Experimental simulation of solid-state phenomena using photonic lattices

Sebabrata Mukherjee

Submitted for the degree of Doctor of Philosophy

Heriot-Watt University

School of Engineering and Physical Sciences (EPS)

Institute of Photonics and Quantum Sciences (IPaQS)

September-2016

Abstract

The propagation of light waves across a periodic array of evanescently coupled optical waveguides can be described by a Schrödinger-like equation for a particle in a periodic potential. This mapping allows us to investigate the dynamics of electrons in a crystalline solid using an artificial crystal of optical waveguides, known as a photonic lattice. The unique capabilities of ultrafast laser inscription enable us to design, fabricate and precisely control various properties of a photonic lattice. Here, we focus on the experimental construction of the Hamiltonians associated with various complex quantum systems using engineered photonic lattices, and then measure the time evolution of a given input state. In this photonic platform, we experimentally observe various single particle effects known from solid-state physics, such as the localised states associated with flat-band lattice geometries, localised Wannier-Stark states, photon-assisted tunnelling and the anomalous topological edge modes in slowly-driven lattices. Specific phenomena associated with particle interactions, such as the dynamics of two interacting particles in a one-dimensional lattice with static and sinusoidally driven Hubbard Hamiltonian, is also investigated. The experimental results presented here will be of interest to a large community, including physicists working on photonics, quantum optics, cold atomic gases, and condensed-matter physics.

To my parents,

Shantwana and Sambit Mukherjee.

Acknowledgements

Firstly, I sincerely thank my academic supervisor Prof. Robert R. Thomson for his guidance, encouragement and advice. I have been extremely lucky to have a supervisor and friend who cared so much about my research.

I would like to thank all the members of Photonic Instrumentation Group, in particular, Dr. Debaditya Choudhury and Mr. David MacLachlan for their assistance in many aspects of experimental work.

I am grateful to my collaborators, Prof. Erika Andersson, Prof. Nathan Goldman, Prof. Patrik Öhberg, Mr. Alexander Spracklen and Dr. Manuel Valiente for various discussions regarding both experimental and theoretical physics. Without their help, none of the work described in this thesis would have been possible. In particular, I would like to thank Alexander for being a good friend and helping me to learn and understand various theoretical problems.

I would like to thank Prof. Ajoy Kar for his guidance and also for allowing me to use various facilities in his laboratory. I am grateful to Prof. Kar and his family for their care and support.

I would like to thank Dr. Andrew Waddie and Mr. Neil Ross for designing and fabricating the diffractive optical element (DOE) respectively. This DOE was a crucial part of many experiments described in this thesis.

I would like to thank my office mates and my close friend, Mr. Dipendu Mandal. Their friendship has made this journey enjoyable.

I am pleased to thank my teachers, Dr. Dwijesh Majumdar, Dr. Asok Kumar Pal and Prof. M. R. Shenoy for guiding and inspiring me.

Finally, I would like to thank my parents for everything they have done for me.

ACADEMIC REGISTRY

Research Thesis Submission

Name*:*	SEBABRATA MUKHERJEE		
School:	EPS		
Version: *(i.e. First, Resubmission, Final)*	FINAL	Degree Sought:	PhD (Physics)

Declaration

In accordance with the appropriate regulations I hereby submit my thesis and I declare that:

1) the thesis embodies the results of my own work and has been composed by myself
2) where appropriate, I have made acknowledgement of the work of others and have made reference to work carried out in collaboration with other persons
3) the thesis is the correct version of the thesis for submission and is the same version as any electronic versions submitted*.
4) my thesis for the award referred to, deposited in the Heriot-Watt University Library, should be made available for loan or photocopying and be available via the Institutional Repository, subject to such conditions as the Librarian may require
5) I understand that as a student of the University I am required to abide by the Regulations of the University and to conform to its discipline.
6) I confirm that the thesis has been verified against plagiarism via an approved plagiarism detection application e.g. Turnitin.

* *Please note that it is the responsibility of the candidate to ensure that the correct version of the thesis is submitted.*

Signature of Candidate*:*		Date:	

Submission

Submitted By *(name in capitals):*	
Signature of Individual Submitting:	
Date Submitted:	

For Completion in the Student Service Centre (SSC)

Received in the SSC by *(name in capitals):*			
Method of Submission *(Handed in to SSC; posted through internal/external mail):*			
*E-thesis Submitted (**mandatory for final theses)***			
Signature:		Date:	

Please note this form should be bound into the submitted thesis.

Table of contents

List of figures

List of publications

Journal papers

1. Sebabrata Mukherjee, Alexander Spracklen, Manuel Valiente, Erika Andersson, Patrik Öhberg, Nathan Goldman, and Robert R. Thomson, "Experimental observation of anomalous topological edge modes in a slowly-driven photonic lattice," *arXiv preprint arXiv:1604.05612* (2016).
[S. M.'s contributions: Designed and fabricated the devices, conceived the characterisation technique, and carried out all measurements. Contributed to numerical simulations and manuscript preparation.]

2. Sebabrata Mukherjee, Manuel Valiente, Nathan Goldman, Alexander Spracklen, Erika Andersson, Patrik Öhberg, and Robert R. Thomson, "Observation of pair tunneling and coherent destruction of tunneling in arrays of optical waveguides," *arXiv preprint arXiv:1604.00689* (2016).
[S. M.'s contributions: Conceived this work, carried out all experiments, performed all numerical simulations, and contributed to manuscript preparation.]

3. Sebabrata Mukherjee, Alexander Spracklen, Debaditya Choudhury, Nathan Goldman, Patrik Öhberg, Erika Andersson, and Robert R. Thomson, "Modulation-assisted tunneling in laser-fabricated photonic Wannier-Stark ladders," *New Journal of Physics* **17**, 115002 (2015).
[S. M.'s contributions: Carried out all experiments, performed all numerical simulations, and contributed to manuscript preparation. He initiated this project after the experimental observation of photonic Wannier-Stark localisation.]

4. Sebabrata Mukherjee, and Robert R. Thomson, "Observation of localized flat-band modes in a one-dimensional photonic rhombic lattice," *Optics Letters* **40**, 5443-5446 (2015).
[S. M.'s contributions: Conceived this work, fabricated and characterised the photonic lattices, performed all numerical simulations, and prepared the manuscript.]

5. Sebabrata Mukherjee, Alexander Spracklen, Debaditya Choudhury, Nathan Goldman, Patrik Öhberg, Erika Andersson, and Robert R. Thomson, "Observation of a localized flat-band state in a photonic Lieb lattice," *Physical Review Letters* **114**, 245504 (2015). **Viewpoint** in Phys. Rev. Lett. [doi: 10.1103/Physics.8.55]. **Featured** in Nature Materials [doi: 10.1038/nmat4378].
[S. M.'s contributions: Designed and fabricated the devices. Built the characterisation setup with R. R. T., carried out all measurements, and contributed to manuscript preparation.]

6. Alexander Arriola, Sebabrata Mukherjee, Debaditya Choudhury, Lucas Labadie, and Robert R. Thomson, "Ultrafast laser inscription of mid-IR directional couplers for stellar interferometry," *Optics Letters* **39**, 4820-4822 (2014).
[S. M.'s contributions: Designed and developed the programmes for the translation stages to fabricate the directional couplers.]

7. Yves Bellouard, Audrey Champion, Benjamin McMillen, Sebabrata Mukherjee, Robert R. Thomson, Charles Pépin, Philippe Gillet, and Ya Cheng, "Stress-state manipulation in fused silica via femtosecond laser irradiation," *Optica*, accepted for publication.
[S. M.'s contributions: Characterised the laser written structures and measured propagation loss.]

Conference submissions

1. Sebabrata Mukherjee, Alexander Spracklen, Debaditya Choudhury, Nathan Goldman, Patrik Öhberg, Erika Andersson, and Robert R. Thomson, "Observation of a localized flat-band state in a photonic Lieb lattice," Topolight 2015, 8-th Optoelectronics and Photonics Winter School: Topological Effects in Photonics, Trento, Italy, March, 2015.

2. Sebabrata Mukherjee, David G. MacLachlan, Arriola Arriola, Debaditya Choudhury, and Robert R. Thomson, "Development of mode-multiplexing/ de-multiplexing device based on integrated photonic-lanterns," International Conference on Fibre Optics and Photonics (Photonics), (paper: T2B.7) IIT Kharagpur, India, December, 2014.

3. Sebabrata Mukherjee, Alexander Spracklen, Debaditya Choudhury, Nathan Goldman, Patrik Öhberg, Erika Andersson, and Robert R. Thomson, "Light localization phenomena in photonic lattices," Photon 16, (P: 91) University of Leeds, Leeds, UK, September, 2016 [Poster].

4. Sebabrata Mukherjee, David G. MacLachlan, Arriola Arriola, Debaditya Choudhury, and Robert R. Thomson, "Development of mode-multiplexing/ de-multiplexing device based on integrated photonic-lanterns," Frontiers in Modern Optics Summer School, International School of Physics "Enrico Fermi", Varenna, Italy, June 2014 [Poster].

5. A. Arriola, S. Mukherjee, D. Choudhury, L. Labadie, and R. R. Thomson, "Ultrafast laser inscribed integrated waveguide components for L-band interferometry," SPIE Astronomical Telescopes + Instrumentation, Montreal, Canada, June, 2014.

6. Hatef Dinparasti, Niclas Westerberg, Michael Marshall, Sebabrata Mukherjee, Robert Thomson, Chunyong Li, Fabio Biancalana, Thomas Roger, and Daniele Faccio, "The dynamical casimir effect in spatially modulated waveguides," Photon 14, Imperial College London, London, UK, September, 2014 [Poster].

Chapter 1

Introduction

1.1 Aim of the thesis

Ultrafast laser inscription is a laser-based manufacturing technique that allows a powerful platform to modify refractive index inside a transparent dielectric material, and one application of which is the direct laser writing of three-dimensional optical waveguide structures. The aim of this thesis is to utilise the unique capabilities of this fabrication technique to experimentally investigate the photonic analogues of various solid-state phenomena. Predicting the behaviour of quasiparticles, such as electrons, inside a crystalline solid is at the heart of solid-state physics. Elucidating the dynamics of quasiparticles using periodic arrays of coupled optical waveguides, known as photonic lattices, has recently attracted great attention in both theoretical and experimental physics. A carefully engineered artificial crystal of optical waveguides enables one to experimentally simulate various intriguing quantum phenomena. One of the most attractive features of this classical simulator is that it offers the possibility to directly visualise the time evolution of the analogous wavefunction by measuring the electric field distribution along the propagation direction. Another fascinating degree of freedom in this photonic setup is that one can excite a specific initial state and observe its evolution in a clean environment which may be difficult or inaccessible in other experimental platforms.

Engineering an array of coupled optical waveguides involves controlling the evanescent coupling among the waveguides and the propagation constant of each waveguide in the array. Ultrafast laser inscription offers the possibility to fabricate three-dimensional arrays of optical waveguides with a core size of a few micrometres. By using high precision translation stages, ultrafast laser inscription also enables the relative positions of the waveguides in the array to be controlled on the scale of a few nanometres – enabling precise control of the evanescent coupling strength. The modification the refractive index inside the substrate, which occurs due to a nonlinear optical absorption process, depends

on the deposition of the light energy in the focal region. This can be tuned in a variety of ways, but for the purpose of this thesis we controlled the refractive index, and hence the propagation constant of the waveguides by adjusting the pulse energy and/or translation speed. The primary objective of this work is to control the above-mentioned parameters and fabricate waveguide based devices where the propagation of light is governed by a desired Hamiltonian and hence, experimentally simulate quantum phenomena using classical optical simulators.

1.2 Thesis outline

In Chapter 2, it will be shown that the propagation of light waves across a straight photonic lattice can be described by a Schrödinger-like equation for a quasiparticle moving in a periodic potential. In the tight binding approximation, the evolution of light intensity along the propagation direction will be numerically calculated for one-dimensional and two-dimensional lattice geometries. The photonic analogue of the static and alternating electric field will also be discussed.

In Chapter 3, the ultrafast laser inscription technique will be discussed briefly. We will mainly focus on discussing the parameter space and different techniques relevant to this work. Then the techniques used to evaluate the coupling constant and waveguide refractive index will be presented.

A novel technique of light-trapping will be discussed in Chapter 4. This is achieved by using lattice geometries that support non-dispersive (or flat) bands. In this chapter, we consider two different flat-band lattices; the first is a quasi-one-dimensional rhombic lattice and the second is a two-dimensional Lieb lattice. The diffractionless propagation of light in these flat-band lattices will be experimentally demonstrated by launching carefully prepared input states that excite a superposition of flat-band modes.

The experimental simulation of the dynamics of an electron in the external electric field will be discussed in Chapter 5. In the presence of a static field, we realise a Wannier-Stark ladder and demonstrate Wannier-Stark localisation when the field strength is much stronger than the tunnelling rate. We then present the effect of static and resonant sinusoidal fields and demonstrate the photonic analogue of photon-assisted tunnelling using circularly curved and sinusoidally modulated photonic lattices.

In Chapter 6, it will be shown how an engineered photonic square lattice can be used to

experimentally simulate the one-dimensional two-particle Hubbard model. In the strong interaction regime of the Hubbard Hamiltonian, the formation of a bound state will be presented. The coherent destruction of tunnelling for the paired particles will also be demonstrated in the presence of a high-frequency alternating force.

In Chapter 7, we demonstrate the photonic analogue of the anomalous Floquet topological insulators. The experimental observation of a novel type of edge mode, which has no static analogue, will be presented using slowly-driven photonic square lattices. These robust chiral edge modes exist even if all the bulk bands are associated with zero-Chern number. The topology of the system is captured by the topological invariants known as winding numbers.

In Chapter 8, the conclusions and future scopes will be presented.

This page is intentionally left blank.

Chapter 2

Waveguide arrays as an optical analogue of solid-state systems

2.1 Introduction

The dynamics of electrons in crystals poses many interesting problems depending on the lattice geometry, external fields, presence of disorders and inter-particle interactions. Investigating these intriguing problems is one of the most challenging tasks in modern physics. For example, probing a microscopic quantum system is often difficult because of various complications that arise due to the unwanted many-body environment, various nonlinear and/or time-dependent terms in the Schrödinger equation and difficulties to excite a specific initial state. In recent years, the experimental investigation of various artificial crystals, such as cold atoms in optical lattices [1–3], proves to be a promising platform for the study of analogous large scale quantum phenomena. Another promising platform to perform the classical simulation of quantum phenomena is the periodic arrays of coupled optical waveguides, known as photonic lattices [4, 5]. The propagation of light waves across a periodic array of coupled optical waveguides mimics the time evolution of the electronic wavefunction in a periodic potential. Due to this mapping, the photonic analogue of various solid-state phenomena can be realised using appropriately engineered photonic lattices. As with cold atoms in optical lattices, this artificial system allows us to access a desired Hamiltonian and hence, acts as a powerful platform for the study of various complex quantum mechanical effects in a clean environment. Indeed, photonic lattices are ideal systems to study various effects in the absence of undesired excitations such as phonons in a real solid.

In this chapter, the mapping between the electronic and the photonic system will be discussed. At first, the Schrödinger-like equation governing the evolution of light waves in a photonic lattice will be derived from Maxwell's equations. The effect of bending the propagation axis of the photonic lattice will then be discussed, to clarify how analogous electric fields can be realised in photonic systems.

2.2 Schrödinger-like equation

In this section, we will derive the Schrödinger-like equation that governs the propagation of light in a straight two-dimensional photonic lattice. A two-dimensional array of optical waveguides, inscribed inside a glass (e.g. borosilicate) medium, is an isotropic, linear, non-magnetic and dielectric medium with refractive index distribution, $n(x, y, z)$. Maxwell's equations [6, 7] in this medium can be written as:

$$\nabla \times \boldsymbol{\mathcal{E}} = -\frac{\partial \boldsymbol{\mathcal{B}}}{\partial t} = -\mu_0 \frac{\partial \boldsymbol{\mathcal{H}}}{\partial t}, \tag{2.1}$$

$$\nabla \times \boldsymbol{\mathcal{H}} = \frac{\partial \boldsymbol{\mathcal{D}}}{\partial t} = \epsilon_0 n^2 \frac{\partial \boldsymbol{\mathcal{E}}}{\partial t}, \tag{2.2}$$

$$\nabla \cdot \boldsymbol{\mathcal{D}} = 0, \tag{2.3}$$

$$\nabla \cdot \boldsymbol{\mathcal{B}} = 0, \tag{2.4}$$

where $\boldsymbol{\mathcal{B}} = \mu_0 \boldsymbol{\mathcal{H}}$, $\boldsymbol{\mathcal{D}} = \epsilon \boldsymbol{\mathcal{E}} = \epsilon_0 n^2 \boldsymbol{\mathcal{E}}$. Here, $\boldsymbol{\mathcal{B}}$, $\boldsymbol{\mathcal{H}}$, $\boldsymbol{\mathcal{E}}$ and $\boldsymbol{\mathcal{D}}$ represent the magnetic induction, magnetic intensity, electric field and displacement vector respectively, μ_0 and ϵ_0 are the permeability and permittivity of free space respectively. Now using the above equations one obtains the following vector wave equation [8] for the electric field vector associated with an electromagnetic wave propagating in this medium:

$$\nabla^2 \boldsymbol{\mathcal{E}} + \nabla \left(\frac{1}{n^2} \nabla n^2 . \boldsymbol{\mathcal{E}} \right) - \mu_0 \epsilon_0 n^2 \frac{\partial^2 \boldsymbol{\mathcal{E}}}{\partial t^2} = 0. \tag{2.5}$$

It should be noted that Eq. (2.5) is obtained without any approximation. Although, here we consider isotropic medium, the x and y components of the electric field vector are coupled in Eq. (2.5) due to the second term.

Approximation 1: Here we consider ultrafast laser inscribed optical waveguides with weak refractive index contrast. In other words, $(n_{\text{eff}} - n_0) \ll n_0$ where n_0 and n_{eff} are the refractive index of the substrate and the effective refractive index of the guided mode respectively. In this situation, the second term in Eq. (2.5) can be ignored, which is known as the *weakly guiding approximation*. Under this approximation there is no coupling between the x and the y components of the electric filed if the medium is isotropic. Hence, the propagation of light waves is governed by the following scalar wave equation:

$$\nabla^2 \Psi - \mu_0 \epsilon_0 n^2 \frac{\partial^2 \Psi}{\partial t^2} = 0. \tag{2.6}$$

Here, $\Psi(x, y, z, t) \leftrightarrow E_{x,y}$ is the x or y component of electric field. Now the time dependence of the electric field can be written as $\Psi(t) = \Psi \exp(-i\omega t)$ where ω is the

angular frequency of the electromagnetic wave. Substituting this expression in Eq. (2.6) we obtain

$$\nabla^2\Psi(x,y,z) + k_0^2 n^2(x,y,z)\Psi(x,y,z) = 0, \tag{2.7}$$

where $k_0 = \omega/c = 1/\lambda$, $c = 1/\sqrt{\mu_0\epsilon_0}$ and $\lambda = 2\pi\lambda$ is the free space wavelength.

Approximation 2: In case of a straight array of optical waveguides, the refractive index profile remains unchanged along the propagation direction (z), and the solutions of Eq. (2.7) can be written as $\Psi(x,y,z) = \psi(x,y,z)\exp(i\beta z)$, where $\beta \approx n_0/\lambda$ is known as the propagation constant. Note that the electric field amplitude is represented as the product of a slowly varying complex field amplitude and a fast oscillating wave, and this is known as the *slowly varying approximation* or the *paraxial approximation*. This approximation is also valid when the waveguide path bends slowly so that the wavefront tilt is negligible. Under this approximation $\frac{\partial^2}{\partial z^2}\psi \to 0$ and Eq. (2.7) becomes

$$\begin{aligned} &\frac{\partial^2\psi}{\partial x^2} + \frac{\partial^2\psi}{\partial y^2} + i2\beta\frac{\partial\psi}{\partial z} - \beta^2\psi + k_0^2 n^2\psi = 0, \\ \text{or,}\quad &i\lambda\frac{\partial\psi}{\partial z} = -\frac{\lambda^2}{2n_0}\Big(\frac{\partial^2}{\partial x^2} + \frac{\partial^2}{\partial y^2}\Big)\psi + \frac{1}{2n_0}(n_0^2 - n^2)\psi. \end{aligned} \tag{2.8}$$

We write the refractive index profile as $n(x,y) = n_0 + \Delta n(x,y)$, and $(n_0^2 - n^2)/2n_0 \approx -\Delta n(x,y)$. Hence,

$$i\lambda\frac{\partial}{\partial z}\psi(x,y,z) = \Big[-\frac{\lambda^2}{2n_0}\nabla_\perp^2 - \Delta n(x,y)\Big]\psi(x,y,z) = \hat{\mathcal{H}}\psi(x,y,z), \tag{2.9}$$

where $\nabla_\perp^2$ ($= \frac{\partial^2}{\partial x^2} + \frac{\partial^2}{\partial y^2}$) is the transverse Laplacian operator. Note that $\triangle n(x,y)$ will be periodic for a periodic array of waveguides. In that case, Eq. (2.9) is analogous to the Schrödinger equation for a quasiparticle (e.g. an electron) moving in a periodic potential in the absence of external electric fields. Here, the propagation direction of light (z) plays the role of time in the Schrödinger equation, the envelope of the electric field, $\psi(x,y,z)$, is analogous to the wavefunction, and the refractive index profile acts as the effective potential for the light field, $V(x,y) \equiv -\triangle n(x,y)$. Eq. (2.9) is an eigenvalue equation and the eigenvalues are the effective refractive indices of the corresponding eigenmodes. Remembering the analogy of this equation with the Schrödinger equation, we shall call the operator $\hat{\mathcal{H}}$, a Hamiltonian.

In this thesis, we consider periodic arrays of single-mode waveguides where the waveguides are well separated such that the modes interact with each other through evanescent coupling. In this situation, coupled mode theory or tight binding approximation can be

used to describe the evolution of electric field along the propagation direction. In Section 2.3 we first introduce evanescent coupling and then in Section 2.4 we discuss the tight binding model.

2.3 Evanescent coupling

This section presents the theory of evanescently coupled two optical waveguides [9, 10]. The electromagnetic (EM) field of a guided mode extends beyond the core region into the surrounding host medium, decaying exponentially as one moves away from the waveguide boundary. The exponentially decaying tail of the EM field is called the evanescent wave, first demonstrated by J. C. Bose [11] (see also [12]) using short Hertz waves (e.g. $\lambda = 20$ cm). When two straight waveguides are close together, such that the evanescent fields of the guided modes overlap, one waveguide mode interacts with the other one, which may result in the transfer of optical energy from one waveguide to another. Such a device is called a directional coupler.

For an isolated waveguide (i.e. when there is no evanescent coupling) the modal field varies with the propagation direction, z, in the form $\exp(i\beta' z)$; where β' is the propagation constant of the mode. This suggests that the differential equation describing the evolution of the amplitude of the modal field, $\psi(z)$, with the propagation direction can be written as

$$i\frac{d\psi}{dz} = -\beta'\psi. \tag{2.10}$$

When two waveguides are evanescently coupled, the presence of the one waveguide can be considered as a dielectric perturbation on the second one and vice versa; see [9]. In this situation, the differential equations become [13]

$$i\frac{d\psi_1}{dz} = -\beta_1\psi_1 - \kappa_{12}\psi_2, \tag{2.11}$$

$$i\frac{d\psi_2}{dz} = -\beta_2\psi_2 - \kappa_{21}\psi_1, \tag{2.12}$$

where κ_{12} and κ_{21} describe the strength of evanescent coupling, β_1 and β_2 are the propagation constants of the two waveguides and ψ_1, ψ_2 are the electric field amplitudes of the guided modes in WG 1 and WG 2 respectively. To solve these coupled differential equations, it is postulated that a system of two evanescently coupled waveguides support modes which propagate with propagation constant β and are a superposition of the

modes supported by WG 1 and WG 2 with amplitudes A and B, i.e.

$$\psi_1 = A\exp(i\beta z), \tag{2.13}$$

$$\psi_2 = B\exp(i\beta z). \tag{2.14}$$

Substituting Eq. (2.13) and (2.14) in Eq. (2.11) and (2.12)

$$A(\beta_1 - \beta) + B\kappa_{12} = 0, \tag{2.15}$$

$$B(\beta_2 - \beta) + A\kappa_{21} = 0. \tag{2.16}$$

From Eq. (2.15)-(2.16), we can write

$$\beta^2 - \beta(\beta_1 + \beta_2) + \beta_1\beta_2 - \kappa_{12}\kappa_{21} = 0,$$

$$\text{or,} \quad \beta = \frac{1}{2}(\beta_1 + \beta_2) \pm \left\{\frac{1}{4}(\beta_1 - \beta_2)^2 + \kappa^2\right\}^{1/2} = \beta_{s,a}, \tag{2.17}$$

where $\kappa = \sqrt{\kappa_{12}\kappa_{21}}$. Therefore, the coupled waveguides support two independent modes. The symmetric mode propagates with propagation constant β_s, and the asymmetric mode propagates with propagation constant β_a. Hence, the general solution of Eq. (2.11) and (2.12) can be written as

$$\psi_1(z) = A_s\exp(i\beta_s z) + A_a\exp(i\beta_a z), \tag{2.18}$$

$$\psi_2(z) = \frac{\beta_s - \beta_1}{\kappa_{12}}A_s\exp(i\beta_s z) + \frac{\beta_a - \beta_1}{\kappa_{12}}A_a\exp(i\beta_a z). \tag{2.19}$$

Now if light is launched at one of the waveguides (say WG 1) at the input, it can be assumed that $\psi_1(z=0) = 1$ and $\psi_2(z=0) = 0$. Hence,

$$A_s + A_a = 1, \quad \text{and} \quad \frac{\beta_s - \beta_1}{\kappa_{12}}A_s + \frac{\beta_a - \beta_1}{\kappa_{12}}A_a = 0. \tag{2.20}$$

$$\text{or,} \quad A_s = \frac{\beta_1 - \beta_a}{\beta_s - \beta_a}, \quad \text{and} \quad A_a = \frac{\beta_s - \beta_1}{\beta_s - \beta_a}. \tag{2.21}$$

The power carried by WG 1 and WG 2 are proportional to $|\psi_1(z)|^2$ and $|\psi_2(z)|^2$ respectively. Substituting Eq. (2.21) in Eq. (2.18) and (2.19):

$$|\psi_1(z)|^2 = 1 - \frac{\kappa^2}{\frac{1}{4}(\beta_1 - \beta_2)^2 + \kappa^2}\sin^2\left[\left\{\frac{1}{4}(\beta_1 - \beta_2)^2 + \kappa^2\right\}^{\frac{1}{2}}z\right], \tag{2.22}$$

$$|\psi_2(z)|^2 = 1 - |\psi_1(z)|^2 = \frac{\kappa^2}{\frac{1}{4}(\beta_1 - \beta_2)^2 + \kappa^2}\sin^2\left[\left\{\frac{1}{4}(\beta_1 - \beta_2)^2 + \kappa^2\right\}^{\frac{1}{2}}z\right]. \tag{2.23}$$

Hence, there is a periodic exchange of energy between the two coupled waveguides with a period $2L_c$ where L_c is given by

$$L_c = \frac{\pi}{2\left[\frac{1}{4}(\beta_1 - \beta_2)^2 + \kappa^2\right]^{\frac{1}{2}}}. \tag{2.24}$$

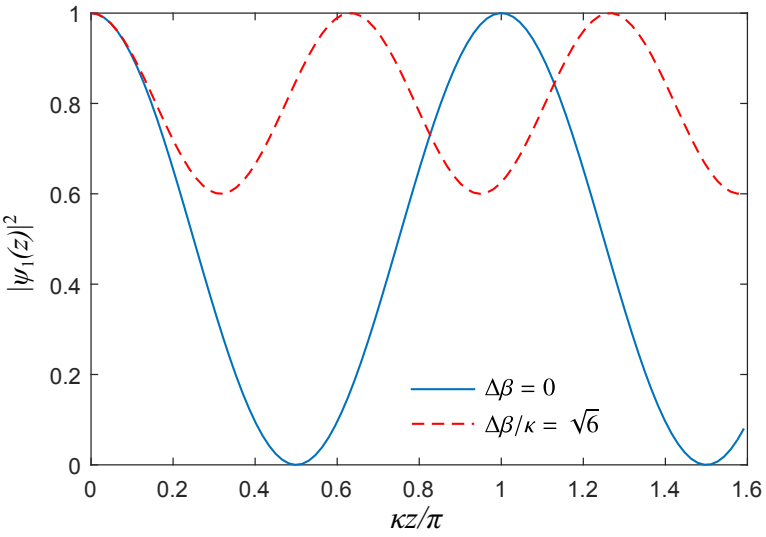

Fig. 2.1: Variation of normalised optical power in WG 1 of a directional coupler as a function of $\kappa z/\pi$ [z is the interaction length, κ is the coupling constant] for $\Delta\beta = 0$ and $\Delta\beta = \sqrt{6}\kappa$. WG 1 was excited at the input ($z = 0$). For $\Delta\beta = 0$, complete transfer of optical power occurs after a minimal interaction length, $\pi/(2\kappa) \equiv L_c$. Note that complete transfer of optical power is not possible if $\Delta\beta \neq 0$.

L_c is known as the coupling length of the direction coupler which corresponds to the minimal interaction length for maximal power transfer. Now for two identical waveguides, assuming $\beta_1 - \beta_2 = 0$ and $\kappa_{12} = \kappa_{21} = \sqrt{\kappa}$, Eq. (2.22), (2.23) and (2.24) become

$$|\psi_1(z)|^2 = \cos^2(\kappa z), \quad |\psi_2(z)|^2 = \sin^2(\kappa z), \\ \text{and} \quad L_c = \frac{\pi}{2\kappa}. \tag{2.25}$$

Fig. 2.1 presents the variation of power in WG 1 as a function of interaction length for $\Delta\beta = \beta_1 - \beta_2 = 0$ (solid curve). When the interaction length is equal to the coupling length, L_c, the power in the WG 1 is zero; that means the optical energy has fully transferred to WG 2. Now as can be seen from Fig. 2.1, for $\Delta\beta \neq 0$ (dotted curve), i.e. if the two waveguides are not identical, complete transfer of optical energy is not possible, and the coupling length is less than $\pi/(2\kappa)$.

A directional coupler discussed in this section is, perhaps, the simplest optical device which is analogous to a static two-level quantum system described by the Hamiltonian $\hat{H}_0$. In this case, there are only two eigenstates ϕ_1 and ϕ_2 and the eigenvalue equations

can be written as

$$\hat{H}_0 \left|\phi_1\right\rangle = E_1 \left|\phi_1\right\rangle ,$$
$$\hat{H}_0 \left|\phi_2\right\rangle = E_2 \left|\phi_2\right\rangle ,$$
$$\text{with} \quad \langle\phi_1|\phi_2\rangle = 0.$$

Here $E_{1,2} \leftrightarrow \beta_{s,a}$ and $|\phi_{1,2}\rangle \leftrightarrow \psi_1 \pm \psi_2$. Now one can intuitively generalise Eq. (2.11) (see also [13, 14]) for an infinite array of identical waveguides as

$$i\frac{d\psi_n}{dz} = -\beta\psi_n - \kappa(\psi_{n+1} + \psi_{n-1}), \tag{2.26}$$

where κ is the coupling constant between the adjacent waveguides [considering only nearest neighbour coupling]. It is assumed that the presence of a third waveguide does not alter the coupling between two adjacent waveguides significantly. In the next section, we will show that this coupled mode equation can also be derived using the tight binding model, and obtain an analytic expression for $\psi_n(z)$.

2.4 Tight binding Model

2.4.1 One-dimensional lattice

In this section, we present the Hamiltonian associated with a straight one-dimensional photonic lattice and then obtain the eigenstate and eigenvalues. Let us consider a one-dimensional periodic array with one waveguide per basis, $\Delta n(x + a) = \Delta n(x)$, where a is the lattice constant; see Fig. 2.2 (a). The waveguides are labelled by $n = ..., -2, -1, 0, 1, 2, ...$ The evolution of light waves (or the dynamics of a quasiparticle) in this system can be described by the following Hamiltonian:

$$\hat{\mathcal{H}} = \Big[-\frac{\lambda^2}{2n_0}\frac{\partial^2}{\partial x^2} - \Delta n(x)\Big]. \tag{2.27}$$

We assume that light energy can transfer from one site to its nearest neighbour sites only, and that κ is the nearest neighbour hopping amplitude. In the second quantisation formalism [15], the nearest neighbour tight binding Hamiltonian can be written as:

$$\hat{\mathcal{H}}_{\text{TB}} = -\beta \sum_n \hat{a}_n^\dagger \hat{a}_n - \kappa \sum_n \hat{a}_n^\dagger (\hat{a}_{n+1} + \hat{a}_{n-1}), \tag{2.28}$$

where $\hat{a}_n^\dagger$ ($\hat{a}_n$) is the creation (annihilation) operator at the n-th lattice site and β is the on-site energy (propagation constant). Assuming that the lattice is composed of N unit

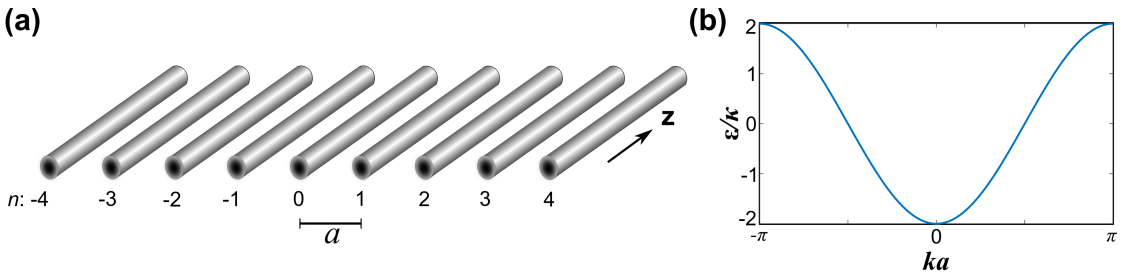

Fig. 2.2: (a) A finite array of coupled optical waveguides. Here a is the lattice constant, z is the propagation direction of light. (b) Band structure of a one-dimensional photonic lattice. Note that β was chosen to be zero.

cells, the Fourier transformation $\hat{a}_k = (1/\sqrt{N}) \sum_m \hat{a}_m \exp(ikam)$ yields the following tight binding Hamiltonian in k-space:

$$\hat{\mathcal{H}}_k = \sum_k \hat{a}_k^\dagger [-\beta - 2\kappa \cos(ka)] \hat{a}_k, \tag{2.29}$$

where $k = 2\pi n/(Na)$. (Note that β represents nothing but the choice of the zero of analogous energy). Here we have discussed the simplest case, a one-dimensional lattice with one waveguide per basis, and the Fourier transformed Hamiltonian is a 1×1 matrix in this case. Fig. 2.2 (b) shows the resultant band structure.

To solve the eigenvalue equation $i\partial_z \psi = \hat{\mathcal{H}}_{TB}\psi$, the wavefunction (envelope of electric field), ψ, is expanded in terms of localised Wannier functions [16]

$$\psi = \sum_{n=1}^{N} c_n a_n^\dagger \left|0\right\rangle, \tag{2.30}$$

where $|0\rangle$ is the vacuum state and c_n is the the expansion coefficient which physically means the electric field amplitude at the n-th waveguide. Substituting Eq. (2.30) in the eigenvalue equation and using Eq (2.28), the following secular equation is obtained for the expansion coefficient, c_n

$$i\frac{\partial}{\partial z} c_n = -\beta c_n - \kappa(c_{n+1} + c_{n-1}). \tag{2.31}$$

Eq. (2.31) is known as the coupled mode equation and can be solved numerically to obtain the evolution of the wavefunction, ψ, along the propagation direction, z. Note that Eq. (2.31) and Eq. (2.26) are identical.

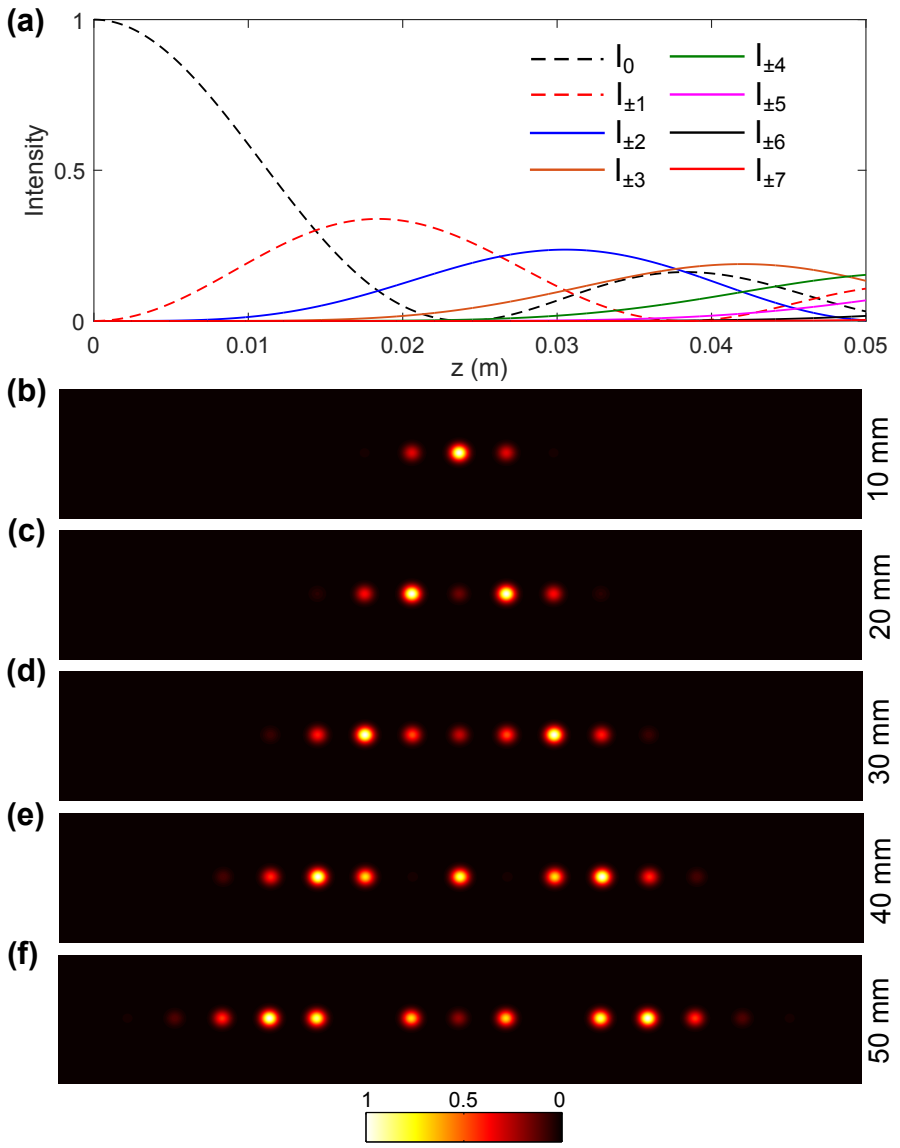

Fig. 2.3: (a) Numerically calculated evolution of light intensity along the propagation direction of a one-dimensional (finite) photonic lattice with 15 waveguides. Input condition: $E_0(z=0)=1$, only the central waveguide was excited, $\kappa = 0.05$ mm^{-1}. The intensity at the n-th waveguide varies as $\mathcal{J}_n^2(2\kappa z)$ which is expected from the analytical expression, Eq. (2.34). (b-f) The output intensity distribution calculated for five different values of propagation distance, z (indicated on the right hand side of each image). Each image is normalised such that the maximum output intensity is 1. See Ref. [17] for an experimental realisation.

To obtain an analytical expression of c_n, Eq. (2.31) can be rearranged as

$$\frac{1}{2\kappa}\Big[\frac{\partial}{\partial z}c_n - i\beta c_n\Big]e^{-i\beta z} = i\frac{1}{2}\Big[c_{n+1}+c_{n-1}\Big]e^{-i\beta z},$$

$$\text{or,}\quad \frac{\partial}{\partial(2\kappa z)}\Big[c_n e^{-i\beta z}\Big] = i\frac{1}{2}\Big[c_{n+1}+c_{n-1}\Big]e^{-i\beta z},$$

$$\text{or,}\quad \frac{\partial}{\partial(2\kappa z)}\Big[i^{-n}c_n e^{-i\beta z}\Big] = \frac{1}{2}\Big[i^{-(n-1)}c_{n-1} - i^{-(n+1)}c_{n+1}\Big]e^{-i\beta z}. \tag{2.32}$$

Now comparing Eq. 2.32 with the following recurrence relation for the Bessel function of first kind:

$$\frac{\partial}{\partial x}\mathcal{J}_m(x) = \frac{1}{2}\big[\mathcal{J}_{m-1}(x) - \mathcal{J}_{m+1}(x)\big], \tag{2.33}$$

and considering the fact that the central (i.e. 0-th) waveguide is excited at the input of the photonic lattice, we obtain the following expression

$$c_n(z) = i^n \mathcal{J}_n(2\kappa z)e^{i\beta z}, \tag{2.34}$$

where $\mathcal{J}_n$ is the Bessel function of the first kind. The intensity at the $\pm n$-th waveguide at the output ($z = z_0$) of the photonic lattice is given by $|c_n|^2 = \mathcal{J}_n^2(2\kappa z_0)$.

Let us now consider a one-dimensional (finite) photonic lattice with N identical waveguides. In this case, the tight binding Hamiltonian will be a $N \times N$ matrix in real space. The Schrödinger-like equation can be numerically solved using Runge-Kutta method to obtain the evolution of intensity along the propagation direction, see Fig. 2.3. As can be seen from Fig. 2.3, the intensity at the n-th waveguide varies as $\mathcal{J}_n^2(2\kappa z)$, which is expected from the analytical expression, Eq. (2.34). In this calculation $\kappa = 0.05$ mm^{-1}, $N = 15$ and the central waveguide is excited at the input, $E_0(z = 0) = 1$. It should be mentioned that similar results were reported in Ref. [17].

2.4.2 Two-dimensional lattice

Let us consider a $N \times N$ square array of optical waveguides, known as a photonic square lattice; Fig. 2.4 (a, b). As discussed in the previous section, the evolution of light-waves in this system is analogous to the dynamics of a quasiparticle in a $N \times N$ square lattice, and is described by the following Hamiltonian

$$\hat{\mathcal{H}} = \Big[-\frac{\lambda^2}{2n_0}\Big(\frac{\partial^2}{\partial x^2} + \frac{\partial^2}{\partial y^2}\Big) - \Delta n(x, y)\Big], \tag{2.35}$$

where $\Delta n(x, y)$ is the transverse refractive index profile of the square array. Using the nearest neighbour tight binding approximation for tightly confined identical single-mode waveguides and setting $\beta = 0$, the coupled mode equation becomes

$$i\frac{d\psi_{l,m}(z)}{dz} = -\kappa\big(\psi_{l+1,m} + \psi_{l-1,m} + \psi_{l,m+1} + \psi_{l,m-1}\big), \tag{2.36}$$

where $\psi_{l,m}$ is the envelope of the electric field at the waveguide (l, m), z is the propagation direction, and κ is the nearest neighbour coupling constant along both axes of the lattice.

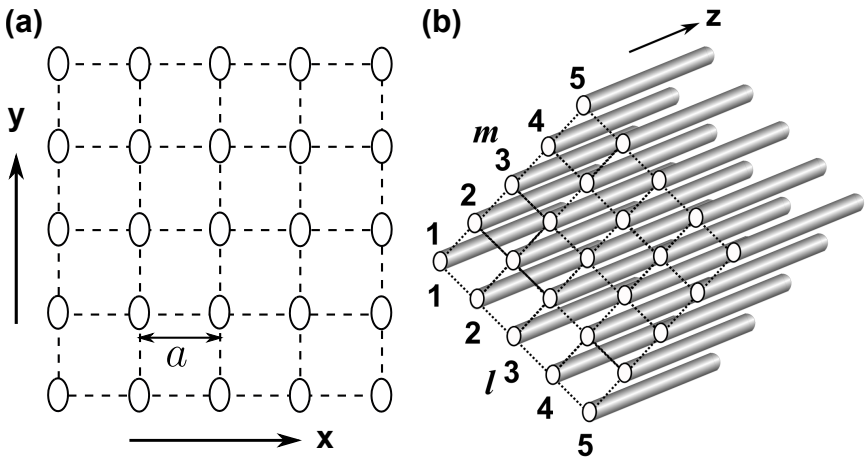

Fig. 2.4: (a) Schematic diagrams of a 5×5 square lattice. Here a is the lattice constant. (b) A 5×5 array of coupled optical waveguides. Note that the lattice axes are rotated by 45^0 with respect to the vertical direction. Here (l, m) are integers labelling the lattice sites in the 2D plane.

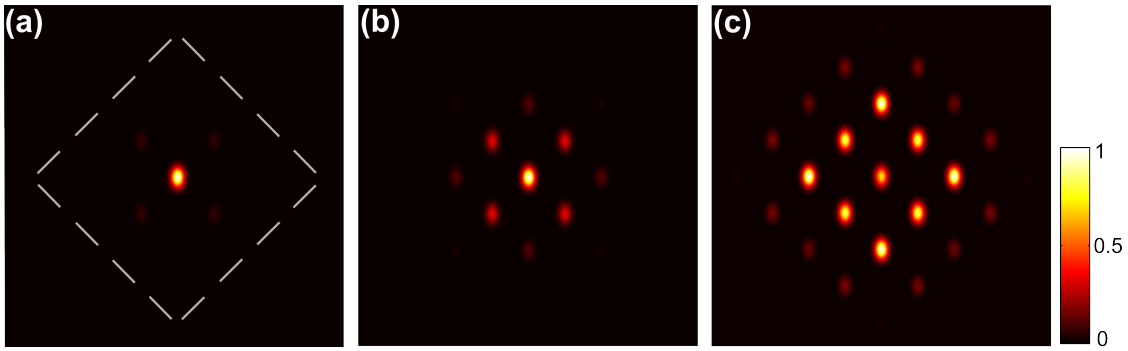

Fig. 2.5: Numerically calculated output intensity distributions for a photonic square lattice. Here $\kappa = 0.025$ mm^{-1}, propagation distance (a) $L = 10$ mm, (b) $L = 20$ mm, (c) $L = 30$ mm. The central waveguide, $(3, 3)$, was excited at the input. The dashed square in (a) indicates the edges of the lattice.

Fig. 2.5 shows numerically calculated output intensity distributions for a photonic square lattice at three different propagation distances. Here $\kappa = 0.025$ mm^{-1} and the central waveguide, $(3, 3)$, was excited at the input.

2.5 Curved photonic lattices

In this section, we will discuss the effect of curving or bending the propagation axis of a photonic lattice. It will be shown that a circular bending is analogous to driving the lattice by a static filed, where the radius of curvature is a measure of the strength of the field. Originally, this idea was proposed by Lenz et al. [18] to predict the possibility to

observe optical Bloch oscillations in circularly curved photonic lattices. We also show that a sinusoidal modulation of the paths of the waveguides in the array mimics the dynamics of a quasiparticle in a sinusoidally driven lattice. Two different approaches to mathematically handle this problem will be discussed.

2.5.1 Conformal transformation

To analyse light propagation in curved waveguides, we use the approach which was reported in Heiblum et al. [19]. Let us first consider a circularly curved single-mode optical waveguide in the laboratory coordinate system (x, y, z); see Fig. 2.6 (a). The inner and outer radii are R_1 and R_2. The scalar wave equation for the electric field envelop, $\Psi(x, y, z)$, is given by

$$\Big[\frac{\partial^2}{\partial x^2}+\frac{\partial^2}{\partial y^2}+\frac{\partial^2}{\partial z^2}+k_0^2 n^2(x, y, z)\Big]\Psi(x, y, z) = 0, \tag{2.37}$$

where k_0 is the free space wave vector and $n(x, y, z)$ is the refractive index profile of the waveguide. It should be highlighted that the refractive index profile appears as a constant at each value of z. Let us assume that the waveguide is bending only in x-z plane; we ignore y coordinate for the time being. We wish to analyse the light propagation in a new coordinate system (u, v), which is defined as: $W = u + iv = f(Z) = f(x + iz)$, see Ref. [18, 19]. In this new coordinate system, using Cauchy Riemann relations (i.e. $\partial u/\partial x = \partial v/\partial z$ and $\partial u/\partial z = -\partial v/\partial x$), the scalar wave equation becomes

$$\Big[\frac{\partial^2}{\partial u^2}+\frac{\partial^2}{\partial v^2}+\Big|\frac{dZ}{dW}\Big|^2 k_0^2 n^2\Big]\Psi(u, v) = 0, \tag{2.38}$$

where $|\partial W/\partial Z|^2 = (\partial u/\partial x)^2+(\partial u/\partial z)^2$. Consider a logarithmic conformal transformation,

$$W = R\ln\Big(\frac{Z}{R}\Big), \tag{2.39}$$

for which $\big|dZ/dW\big| = \exp(u/R)$. Now Eq. (2.38) can be written as

$$\Big[\frac{\partial^2}{\partial u^2}+\frac{\partial^2}{\partial v^2}+k_0^2 n^2\exp(2u/R)\Big]\Psi(u, v) = 0. \tag{2.40}$$

Eq. (2.40) describes a straight waveguide with a new refractive index profile, $n\exp(u/R)$. The width of the straight waveguide is $R\ln\frac{R_2}{R_1}$. For our laser inscribed optical waveguides, the coordinate u varies on a micrometre scale, whereas the radius of curvature in

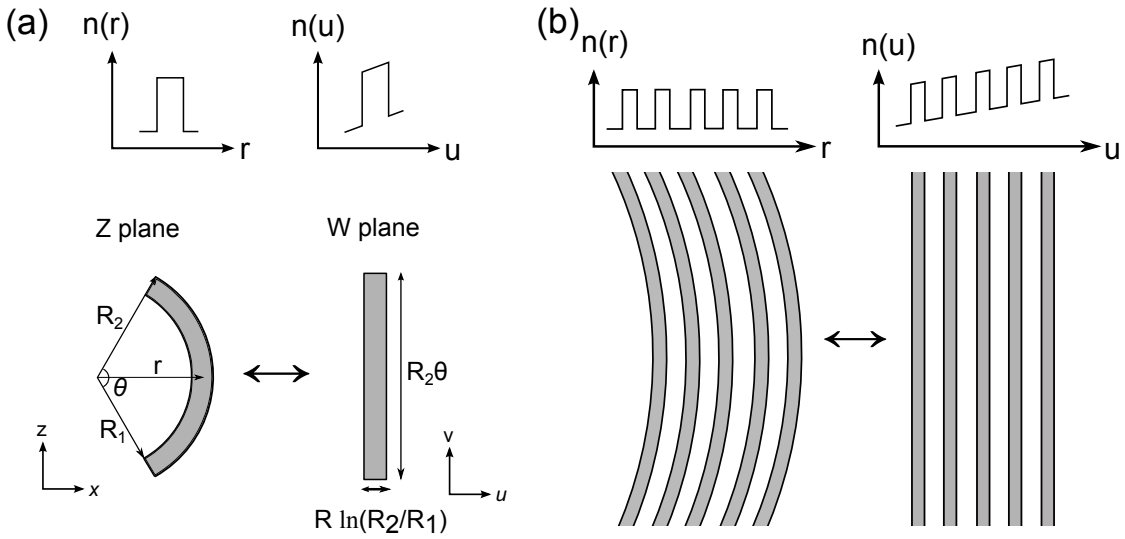

Fig. 2.6: (a) A circularly curved optical waveguide in the laboratory frame, (x, z) and its conformal transformation [see Eq. (2.39)]. In the new coordinate system, (u, v), the waveguide is straight with a new refractive index profile. (b) A circularly curved photonic lattice with step refractive index profile is equivalent to a straight photonic lattice where the refractive index profile is a superposition of the original profile and a linear ramp. See also Ref. [18, 19]

our discussions will be of the order of a few hundred millimetres. Hence, the first two terms in the Taylor series expansion of $\exp(u/R)$ will be sufficient to consider for our discussions; i.e. $\exp(u/R) \approx (1 + u/R)$.

We now consider a one-dimensional periodic array (periodic along x direction) of circularly curved optical waveguides where all the waveguides in the array are simultaneously bending in x-z plane only; see Fig. 2.6 (b). After a similar logarithmic conformal transformation, all the waveguides will be straight in the new (u, v) coordinate system with a new refractive index profile. The scalar equation for this curved array can be written as

$$\Big[\frac{\partial^2}{\partial u^2} + \frac{\partial^2}{\partial v^2} + k_0^2 n^2 (1 + 2u/R)\Big] \Psi(u, v) = 0, \tag{2.41}$$

where n is the refractive index profile of the array. Using paraxial approximation [i.e. $\Psi = \psi \exp(i\beta v)$ and $\frac{\partial^2}{\partial v^2}\psi \to 0$; see Section 2.2] and also remembering the fact that typically, the index contrast for laser-fabricated waveguides is very weak ($\sim 10^{-4}$ to 10^{-3}), we write the Schrödinger-like equation in (u, v) coordinates for the circularly curved photonic lattice

$$i\lambda \frac{\partial \psi}{\partial v} = \Big[- \frac{\lambda^2}{2n_0} \frac{\partial^2}{\partial u^2} - \Delta n(u) - \frac{n_0}{R} u \Big] \psi(u, v). \tag{2.42}$$

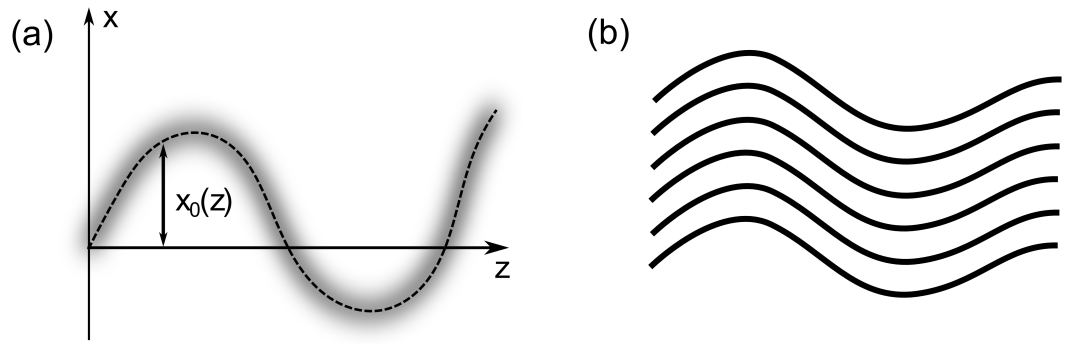

Fig. 2.7: Schematic diagrams of (a) a waveguide which is slowly bending along x direction; $x_0(z)$ describes the bending profile. (b) An example of modulated or curved photonic lattice. Note that all the waveguides are modulating simultaneously.

Eq. (2.42) is analogous to the Schrödinger equation for a quasiparticle (e.g. an electron) moving in a one-dimensional lattice with an externally applied electric field ($\mathcal{E}_{dc}$) along the negative u direction. Here the radius of curvature is a measure of the electric field: $e\mathcal{E}_{dc} = n_0/R$; charge of the quasiparticle is e. Now if the radius of curvature changes along the propagation direction, one can intuitively understand that the amplitude and/or direction of the external field will change with z, the analogous time.

2.5.2 Kramers-Henneberger transformation

Kramers-Henneberger transformation is a time dependent unitary transformation which was introduced to investigate the problem of interaction of atoms with intense light; see for example [20]. This transformation can be used to analyse the propagation of light in a curved one-dimensional photonic lattice under the paraxial approximation. Let us consider that the guide axis of each waveguide in the lattice is slowly and simultaneously bending along x-axis, indicated by $x_0(z)$, see Fig. 2.7 (a, b). The evolution of electric field envelop is governed by the following paraxial equation [21]:

$$i\lambda\frac{\partial\psi(x,z)}{\partial z} = \Big[-\frac{\lambda^2}{2n_0}\frac{\partial^2}{\partial x^2} - \Delta n\big(x - x_0(z)\big)\Big]\psi(x,z). \tag{2.43}$$

Using Kramers-Henneberger transformation $x' = x - x_0(z)$, $z' = z$ and $\Phi(x',z') = \psi(x',z')\exp\Big[-i(n_0/\lambda)\partial_{z'}x_0(z')x' - i(n_0/2\lambda)\int_0^{z'}\partial_{z'}x_0(\xi)^2 d\xi\Big]$, Eq. 2.43 can be written as [22]

$$i\lambda\frac{\partial\Phi(x',z')}{\partial z'} = \Big[-\frac{\lambda^2}{2n_0}\frac{\partial^2}{\partial x'^2} - \Delta n(x') - Fx'\Big]\Phi(x',z'), \tag{2.44}$$

with $F = -n_0 \partial_{z'}^2 x_0(z')$. Eq. (2.44) is analogous to the Schrödinger equation for a quasiparticle (e.g. an electron) of effective mass n_0 moving in a one-dimensional periodic potential, $V(x') = -\Delta n(x')$, and an external force, F, z' plays the role of time. If the charge of the quasiparticle is e, then the analogue external electric field realised by bending the lattice is given by $\mathcal{E} = F/e$.

Now consider a circularly curved photonic lattice where all the waveguides have a radius of curvature, R ($R \gg a$). The bending profile, $x_0(z')$, of each waveguide is given by: $x_0^2(z') = R^2 - z'^2$. This implies that the analogous force is $F = n_0/R$, which is a static force. Similarly, in case of a sinusoidal modulation of the waveguide paths with amplitude A and spatial frequency ω: $x_0(z') = A\sin(\omega z')$, the analogous force is given by $F = n_0 A\omega^2 \sin(\omega z')$.

2.6 Chapter summary

In this chapter, we have discussed the propagation of light in coupled optical waveguides and shown the mapping between a crystalline solid and an artificial crystal of optical waveguides. We have considered one-dimensional and two-dimensional photonic lattices and discussed how the band structure can be calculated in the nearest neighbour tight binding approximation. We have also shown how a curved photonic lattice can mimic the dynamics of an electron in a driven lattice. These mappings will be used in the following chapters to demonstrate various phenomena known from solid-state physics.

This page is intentionally left blank.

Chapter 3

Ultrafast laser inscription of optical waveguides

3.1 Introduction

Under certain conditions, focused sub-bandgap femtosecond (fs) laser pulses can drive nonlinear absorption processes inside transparent dielectric materials. The induced micro-plasma can result in a permanent and localised modification to the material structure near the focus. In fused silica, for example, three different femtosecond laser writing regimes have been identified where the induced modification results in either an isotropic refractive index modification [23], a highly birefringent refractive index change [24] or the formation of a laser induced void [25]. The regime of modification depends on various exposure parameters such as pulse energy, pulse duration, polarisation and wavelength, as well as on the numerical aperture of the focusing lens and the translation speed of fabrication. If correctly controlled, a smooth and isotropic refractive index modification of the order of $10^{-4} - 10^{-3}$ [26] can be induced using ultrafast laser inscription, which then enables the direct fabrication of three-dimensional optical waveguides. The overall aim is to apply laser inscription to design and fabricate tightly confined low-loss (propagation loss: ~ 1 dB/cm near 780 nm wavelength) optical waveguides and waveguide arrays. Another crucial objective is to precisely control the evanescent coupling between waveguides and the propagation constant of each waveguide. In this chapter, the fabrication and characterisation of optical waveguides will be presented.

3.2 Ultrafast laser inscription technique

Ultrafast laser inscription (ULI) is a rapidly maturing and powerful technique for the fabrication of three-dimensional integrated photonic devices. To date, a wide variety of devices has been realised using ULI, including evanescently coupled directional-couplers [27], Mach-Zehnder interferometers [28], micro-lens arrays [29], waveguide

Bragg gratings [30–32] and photonic lanterns [33]. The schematic diagram of the experimental setup used for ULI within the Photonic Instrumentation Group at Heriot-Watt University is shown in Fig. 3.1. As shown in Fig. 3.1 (a), a transparent dielectric substrate is mounted on x-y-z translation stages (Aerotech), and the fs-laser beam is focused inside the substrate using a lens, L_3. We control the power and polarisation of the laser beam using a set of waveplates and a polarisation beam splitter. The femtosecond laser (Menlo Systems, BlueCut) is a Yb-doped fibre laser which can supply femtosecond pulses (between 320 fs and 440 fs) of 1030 nm light at five different pulse repetition frequencies (PRFs$=0.25, 0.5, 1.0, 2.0$ and 10.0 MHz).

Although refractive index modification is highly sensitive to the substrate material, ULI has been used to fabricate waveguides in a variety of materials, including amorphous glasses, such as fused silica [34, 35], N-BK7 [36], AF-45 [37], Eagle^{2000} [38], GLS [39] etc, as well as crystalline materials such as $LiNbO_3$ [40] and Nd: YAG [41]. Through careful optimisation of ULI parameters, it is possible to control the geometry of the structure to fabricate optical waveguides [42]. In case of fused silica, for example, a positive refractive index modification, which acts as the core, can be achieved at the focus of the laser beam resulting in a "Type I" waveguide. In case of $LiNbO_3$, as the refractive index modification is usually negative ("TypeII"), waveguiding is achieved by engineering the cladding; see Ref. [43] for fabrication details of TypeI waveguides in z-cut $LiNbO_3$. In this work, we use borosilicate glass (AF-45 and Eagle^{2000}) as substrate and inscribe TypeI waveguides.

3.2.1 Fabrication configurations

As shown in Fig. 3.1 (b, c), waveguides can be fabricated using two different ULI configurations [44], each one having its own advantages and disadvantages. In the longitudinal writing geometry (LWG), the cross-section of the inscribed waveguide is generally circular due to the circular symmetry of the focused laser beam. However, the length of the structure is limited by the working distance of the focusing lens ($\approx$ few mm). Due to the depth-dependent aberrations [45], the refractive index profile of the inscribed waveguide can also vary along its length, which is not desirable. In the transverse writing geometry (TWG), on the contrary, the length of the waveguide is not limited by the working distance of the lens, and almost arbitrary three-dimensional waveguide structures can be inscribed over a depth range of few millimetres. A disadvantage of the TWG is that the cross-section of the inscribed waveguide (i.e. the refractive index profile), which is

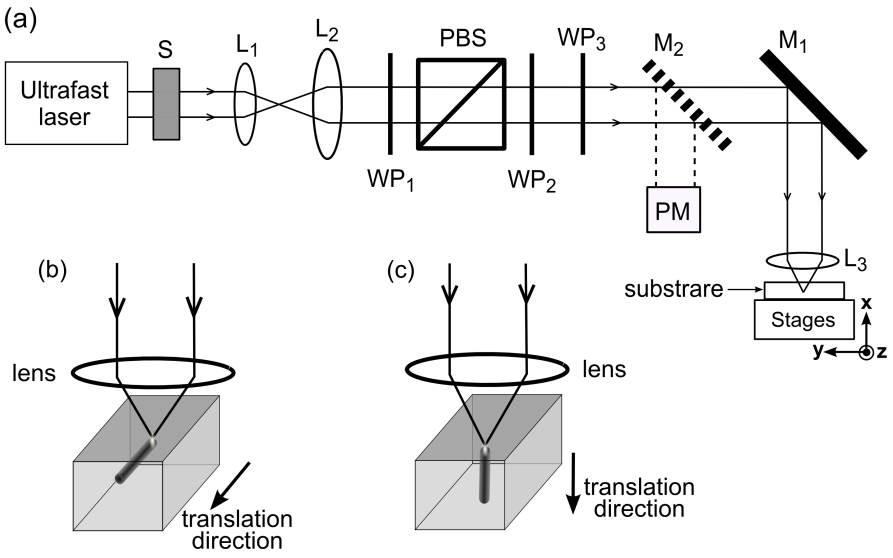

Fig. 3.1: (a) Schematic diagram of ultrafast laser inscription setup. A transparent dielectric substrate is mounted on x-y-z translation stages, and the fs laser beam is focused inside the substrate using a lens, L_3. We control the power and polarisation of the laser beam using a set of waveplates and a polarisation beam splitter (PBS). Here WP_1 and WP_2 are half-waveplates, WP_3 is a quarter-waveplate; M_1, M_2 are mirrors; M_2 is on a flip-mount to measure optical power using a power meter (PM); L_1, L_2 are two convex lenses, which form a Keplerian telescope, used to expand the laser beam and S is a shutter. (b) The transverse writing geometry (TWG). (c) The longitudinal writing geometry (LWG).

determined by the spot size $[2\omega_0 = 2\lambda/(\pi \mathrm{NA})]$, and Rayleigh range $[b = 2\pi n\omega_0^2/\lambda]$ of the laser focus, is usually asymmetric. However, to achieve waveguiding with well-confined guided modes, a precisely symmetric refractive index profile is not necessary, and due to the inherent writing flexibility offered by TWG, we have chosen to utilise the this configuration for all of the experimental works; we will not discuss the LWG further.

3.2.2 High and low repetition rate regimes

The pulse repetition rate of the femtosecond laser plays a critical role in the process of modifying the structure of the substrate medium [38]. When the time between the laser pulses is shorter than the time to diffuse the absorbed heat from the focal volume, the laser induced modification is primarily determined by the manner in which heat diffuses away from the focal region. When the heat diffusion process is isotropic and symmetric, the cross section of the inscribed structure can be significantly more symmetric

compared to the shape and symmetry of the focal volume itself. This regime (PRF above ~ 1 MHz) is known as the high repetition rate (HRR) regime. In this case, as the number of pulses incident on the focal volume increases, heat accumulates within the focal volume and the temperature is driven far above the limit that is achievable using a single pulse of the same energy.

Unfortunately, when operating in the HRR regime using a TWG, optical waveguides often exhibit complicated refractive index profiles, and the refractive index contrast of the inscribed structure is often not well controlled. In particular, this regime is not suitable to fabricate photonic lattices, where it is necessary to inscribe each waveguide without modifying the refractive index of the nearby waveguides. For this reason, it is desirable to operate in the low repetition rate (LRR) regime, using femtosecond lasers operating at PRFs $\lesssim 1$ MHz. In this regime, the time between pulses is sufficiently long compared to the time to diffuse the absorbed heat from the focal region before the arrival of the next pulse. In other words, each pulse acts individually to modify the material at the focal volume. However, the main disadvantage of operating in the LRR regime (using TWG configuration) is that the cross-section of the modified region is primarily determined by the focusing lens, and as a result, may be highly asymmetric. Several methods to correct for this asymmetry have been demonstrated, including the astigmatic focusing [46], deformable mirror beam reshaping [47], slit beam shaping [34] and multiscan technique [35]. For the work outlined in this thesis, we have chosen to write waveguides in the LRR regime using the TWG. To control the refractive index profile the multiscan technique and the slit beam shaping technique were investigated which will be discussed in the following section.

3.2.3 Controlling the waveguide refractive index profile

Controlling the refractive index profile, i.e. the refractive index contrast and the shape of the index modification, is a key part of waveguide fabrication. It determines the effective refractive index (n_{eff}) of the mode, propagation and bend losses and most importantly, for applications described in this thesis, the evanescent coupling between the adjacent waveguides. In this section, two different techniques will be discussed which was used to efficiently control the refractive index profile.

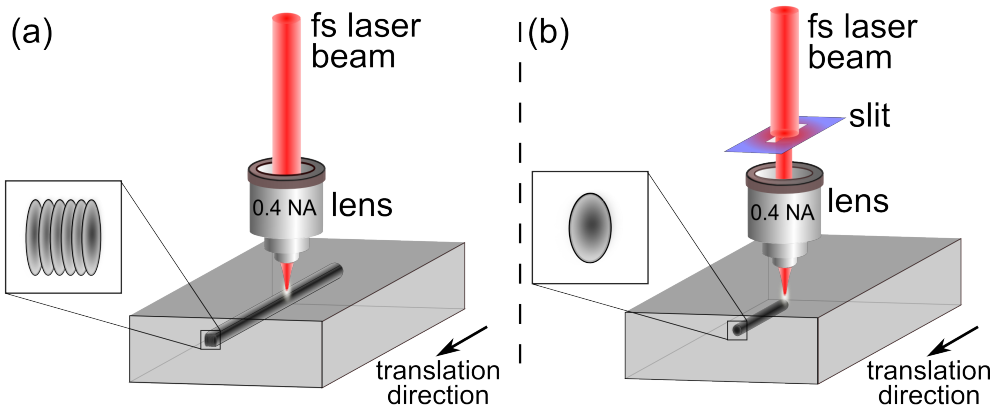

Fig. 3.2: Schematic diagram of two different ULI techniques to control the refractive index profile: (a) multiscan technique and (b) slit beam shaping technique.

Multiscan technique

Multiscan technique relies simply on scanning the substrate through the focus multiple times to "build" a symmetric waveguide cross section from the individual building blocks; see Fig. 3.2 (a). When fabricating waveguide structures in the LRR regime, the refractive index profile of each translation (or scan) is asymmetric and its height and width depend on the numerical aperture of the focusing lens for a given pulse energy and translation speed (v). The total number of scans and the scan-separation are optimised to obtain tightly confined low-loss waveguides. The main advantage of the multiscan technique is that optical waveguides can be fabricated without modifying the optical properties of the surrounding medium significantly. It is for this reason that the multiscan technique can be very powerful for fabricating devices, such as photonic lanterns, where the separation between waveguides could be of the order of a fraction of a micrometre, and this technique enables to inscribe each waveguide without modifying the refractive index its nearby waveguides.

We investigated the optical properties of the straight waveguides fabricated using multiscan technique inside a 10-mm-long borosilicate (AF-45) substrate at ≈ 200 μm depth from the top surface. Each waveguide was fabricated by translating the substrate 21 times through the focus with 0.2 μm separation between two adjacent translations. In Fig. 3.3 (a) the variation of insertion loss (i.e. input coupling loss+propagation loss) at 780 nm wavelength is plotted as a function of pulse energy for different translation speeds and pulse repetition rates. These waveguides were characterised using single-mode-fibre input coupling and free-space output coupling. In this experiment, all six sets of data follow a similar trend: initially, the insertion loss of the single-mode waveg-

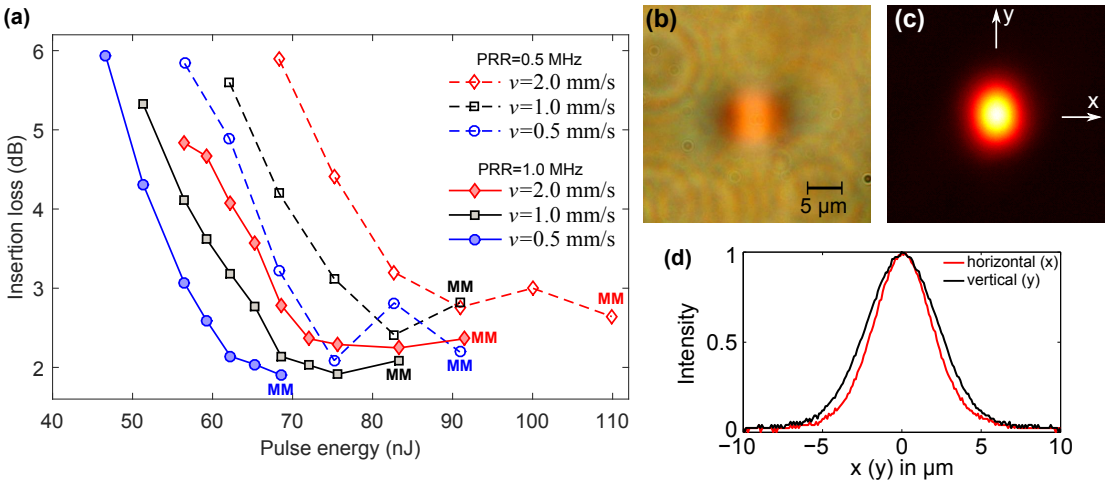

Fig. 3.3: Multiscan technique. (a) The variation of insertion loss at 780 nm wavelength as a function of pulse energy for three different translation speeds and two pulse repetition rates (PRRs). These waveguides were fabricated inside a 10-mm-long borosilicate (AF-45) substrate at ≈ 200 μm depth from the top surface. For each set of data, the waveguide with maximum pulse energy is multimode, and is denoted by "MM". (b) White-light-transmission micrograph of the facet of a tightly confined low-loss optical waveguide fabricated using the multiscan technique. Fabrication parameters are PRF$=$ 500 kHz, $t_p = 350$ fs, $\lambda = 1030$ nm, pulse energy$=$77 nJ, circular polarisation, NA$=$0.4 and $v = 1$ mm/s. This waveguide supports only the fundamental mode at 780 nm wavelength (c, d). The mode is elliptical: MFD$_x \approx 8$ μm MFD$_y \approx 10$ μm.

uides reduces rapidly as the pulse energy is increased. The insertion loss then becomes less sensitive to pulse energy, until we reach a pulse energy at which the the waveguide becomes multimode. It was also observed that the confinement of the fundamental mode becomes tighter as the pulse energy is increased. A white-light-transmission micrograph of the facet of a low-loss waveguide is shown in Fig. 3.3 (b). Fig. 3.3 (c, d) present the intensity profile of the supported (fundamental) mode for this waveguide fabricated with 500 kHz PRF and 1 mm/s translation speed. As shown in this figure, the mode is elliptical with mode field diameters (i.e. the diameter at which the far field power falls to $1/e^2$ of its maximum value) MFD$_x \approx 8$ μm and MFD$_y \approx 10$ μm along the horizontal and vertical directions respectively. Unfortunately, long fabrication times would be required to inscribe waveguide arrays using multiscan technique, which could be a problem due to instabilities in the fabrication process. For creating waveguide arrays, it would therefore be desirable to fabricate each waveguide using the single-scan

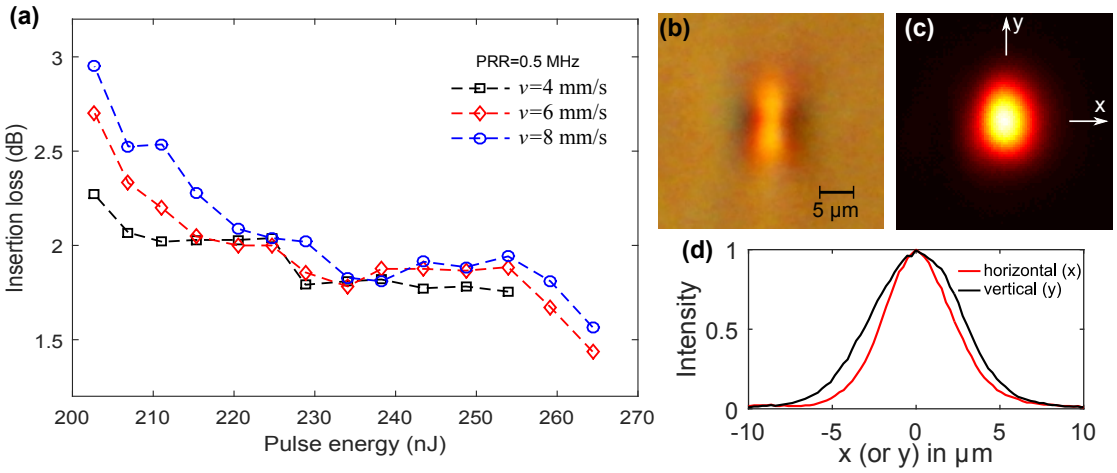

Fig. 3.4: Slit beam shaping technique. (a) The variation of insertion loss at 780 nm wavelength as a function of pulse energy for three different translation speeds. These waveguides were fabricated inside a 10-mm-long borosilicate (Eagle^{2000}) substrate at $\approx$ 200 μm depth from the top surface. (b) White-light-transmission micrograph of the facet of a tightly confined low-loss optical waveguide. Fabrication parameters are PRF = 500 kHz, t_p = 350 fs, λ = 1030 nm, pulse energy = 234 nJ, circular polarisation, NA = 0.4, v = 4 mm/s and slit width: 2 mm. This waveguide supports only the fundamental mode at 780 nm wavelength (c, d) with MFD$_x$ $\approx$9.4 μm MFD$_y$ $\approx$10.6 μm.

technique – we discuss this in the following section.

Slit beam shaping technique

The refractive index profile for the tightly confined, low-loss waveguides fabricated using single-scan technique in the LRR regime (PRF = 500 kHz) with 350 fs pulses is usually complicated, and it was found that the upper portion of the modified region does not guide either due to the creation of voids or negative refractive index modification. Slit beam shaping technique, originally demonstrated in Ref. [34], was used to resolve the above-mentioned problem. A slit with adjustable width is inserted in the beam path before the lens as shown in Fig. 3.2 (b). Note that the slit is along the direction of waveguide axis. The complex valued electric field profile at the focus of the lens is the Fourier transform of the aperture function (e.g. the complex valued field amplitude transmitted through the slit) and hence, by tuning the width of the slit it is possible to control the width of an optical waveguide. The height of the waveguide is controlled primarily via the numerical aperture of the beam in the orthogonal axis.

To investigate the optical properties of the waveguides fabricated using slit beam shaping technique, three sets of straight waveguides (translation speed, $v = 4$, 6 and 8 mm/s) were fabricated inside a 10-mm-long borosilicate (Eagle^{2000}) substrate. Each waveguide was fabricated by translating the substrate once through the focus (NA: 0.4) and the pulse energy was varied from 190 nJ to 264 nJ. In Fig. 3.4 (a) the variation of insertion loss at 780 nm wavelength is plotted as a function of pulse energy for different translation speeds. A white-light-transmission micrograph of the facet of a low-loss waveguide is shown in Fig. 3.4 (b). Fig. 3.4 (c, d) present the intensity profile of the supported (fundamental) mode for this waveguide fabricated with 234 nJ and 4 mm/s translation speed. The mode field diameters are MFD$_x \approx 9.4$ μm and MFD$_y \approx 10.6$ μm along the horizontal and vertical directions respectively.

The fabrication parameters that will be used in the following chapters are shown in Table 3.1.

3.3 Measurement of coupling constant

A brief theory of two evanescently coupled optical waveguides was discussed in Section 2.3. In this section, the measurement of coupling constant will be presented; see also [48]. Consider two identical optical waveguides, each supporting only the fundamental mode when isolated, with a core to core separation, d, and the maximum propagation distance, $z_{\text{max}} = L$. In this situation, if one of the waveguides is excited at the input (say WG 1), the normalised light intensities in the two waveguides are given by $I_1 = I_0 \cos^2(\kappa z)$ and $I_2 = I_0 \sin^2(\kappa z)$, where $\kappa = \pi/(2L_c)$ is the coupling constant, L_c is the coupling length, I_0 is the input intensity at WG 1. It should be mentioned that $I_{1,2} \equiv I_{1,2}(z) f(x, y)$, where $f(x, y)$ can be approximated as a two-dimensional Gaussian function. Now one way to obtain the value of κ is to measure L_c. Fig. 3.5 shows the measured variation of $I_1(z)$ and $I_2(z)$ as a function of propagation distance, z, for $d = 13$ μm, $\lambda = 780$ nm. From Fig. 3.5, it can be seen that $L_c \approx 9.5$ mm and hence, the calculated value of κ is 0.165 mm^{-1}. These couplers were fabricated inside Eagle^{2000} substrate and the refractive index profile was controlled using slit beam shaping technique. After fabrication, the facets of the glass substrate were optically polished. The devices were characterised using single-mode-fibre (SM 600) input coupling and free space output coupling. Light at 780 nm wavelength from a CW diode laser was used for characterisation. The value of κ can also be obtained by measuring I_1 and I_2 for a

Tab. 3.1: Fabrication parameters

Inscription laser	Menlo Systems, BlueCut
Laser wavelength	1030 nm
Pulse repetition frequency	500 kHz
Pulse width	350 fs
Laser polarisation	Circular
Beam width	5 mm
Inscription lens (NA)	0.4
Substrate	Borosilicate glass Eagle^{2000}
Beam shaping	Slit beam shaping technique
Slit width	2.0 mm

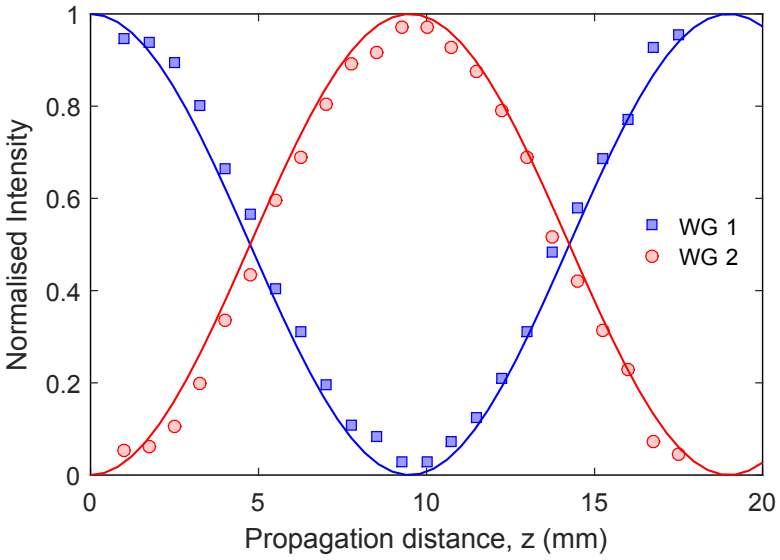

Fig. 3.5: Measured variation of light intensity in a two-waveguide coupler as a function of propagation distance, z, for waveguide-to-waveguide separations, $d = 13$ μm, $\lambda = 780$ nm. Waveguide 1 was excited at the input for all measurements. Solid lines are the guides to the eyes.

known device length, L:

$$\kappa = \frac{1}{L} \tan^{-1}\left(\sqrt{\frac{I_2(L)}{I_1(L)}}\right). \tag{3.1}$$

To investigate the variation of the coupling constant as a function of inter-waveguide separation, d, we fabricated twelve directional couplers (11 μm $\leq d \leq 22$ μm in steps of 1 μm) inside Eagle^{2000} substrate using 350 fs laser pulses of 245 nJ pulse energy and

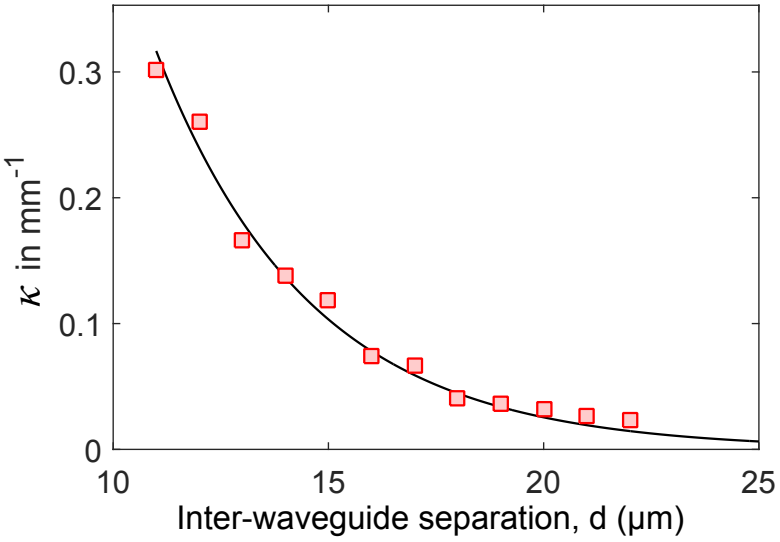

Fig. 3.6: Variation of coupling constant (at 780 nm wavelength) as a function of waveguide-to-waveguide separation, d. The red squares are the measured values of coupling constants and the solid black line is an exponential fit.

500 kHz PRF. Fig. 3.6 shows the variation of κ calculated using Eq. 3.1, as a function of d. The red squares are the measured values of coupling constants and the solid black line is an exponential fit. Note that the value of κ drops exponentially as d was increased for a given wavelength. It should be highlighted that the coupling constant for a given directional coupler with fixed d can be tuned by changing the wavelength of light. In other words, κ is a function of wavelength as the refractive index profile, that determines κ, varies with wavelength. This will be discussed further in Chapter 7.

In this section, we have only considered two evanescently-coupled straight waveguides. In Section 7.4, tapered couplers consisting of two synchronously bending waveguides is discussed.

3.4 Estimation of waveguide refractive index

The refractive index profile determines all the light transport properties exhibited by a waveguide array. However, the precise knowledge of refractive index profile is neither required nor easy to measure. In many situations, we are interested in an array of identical straight optical waveguides. In this situation, the information of coupling constant, which can be measured accurately, is enough to describe the observed phenomena. However, in various situations, the difference in propagation constants for two optical waveguides will be required. This means the knowledge of the difference in the

effective refractive index of the supported modes will be sufficient. In this section, three different ways to estimate the waveguide refractive index will be discussed.

Method 1: At first, a simple and "crude" way of estimating the waveguide refractive index will be discussed. Let us consider the waveguide shown in Fig. 3.4 (b). The mode field diameters of the supported mode at 780 nm wavelength are $\text{MFD}_x \approx 9.4$ μm, $\text{MFD}_y \approx 10.6$ μm along the horizontal and vertical axes respectively. The transverse dimension of the waveguide is measured using an optical microscope and is found to be ≈ 5.5 $\mu\text{m} \times 3.5$ μm (height and width). The propagation of light in an optical waveguide with this dimension is then simulated by BeamPROP software. We assume that the waveguide has step refractive index profile where $n_{\text{cl}} = 1.5$ (the refractive index of the cladding, Eagle^{2000}) and the refractive index contrast, Δn, is varied to investigate how the mode field diameters changes as a function of n_{core}. It was found that the simulated mode field diameters match with the experimentally measured values when $n_{\text{core}} \approx 1.5015$. It should be highlighted that the refractive index profile can also be calculated by solving the Helmholtz equation and using the measured the mode field profile; see [49, 50]

Method 2: Another way to estimate the waveguide refractive index is to study a one-dimensional diffraction grating which is formed by a one-dimensional array of identical optical waveguides. The physical depth of a grating, which is the height of a waveguide (h) in the array, can be measured using an optical microscope. Such an array of optical waveguide (with grating period ~ 15 μm) acts almost like a sinusoidal phase grating. Now the absolute diffraction efficiency of a sinusoidal phase grating at the first order (η_1) is given by [51]:

$$\eta_1 = \mathcal{J}_1^2\Big(\frac{2\pi(n_{wg} - n_0)}{\lambda}h\Big), \tag{3.2}$$

where n_0 is the refractive index of the substrate, n_{wg} is the refractive index of the waveguide, λ the is wavelength of light, and $\mathcal{J}$ is the Bessel function of the first kind. By measuring the absolute diffraction efficiency of this grating at the first order (η_1), one can estimate n_{wg}. This method of estimating n_{wg} will be further discussed in Chapter 6.

Method 3: The third method relies on the fundamental principle of Bragg gratings. Let us consider a single-mode straight waveguide with periodically modulated refractive index along the propagation direction (z). When light propagates through such a waveguide, the forward propagating mode is strongly coupled to the mode propagating

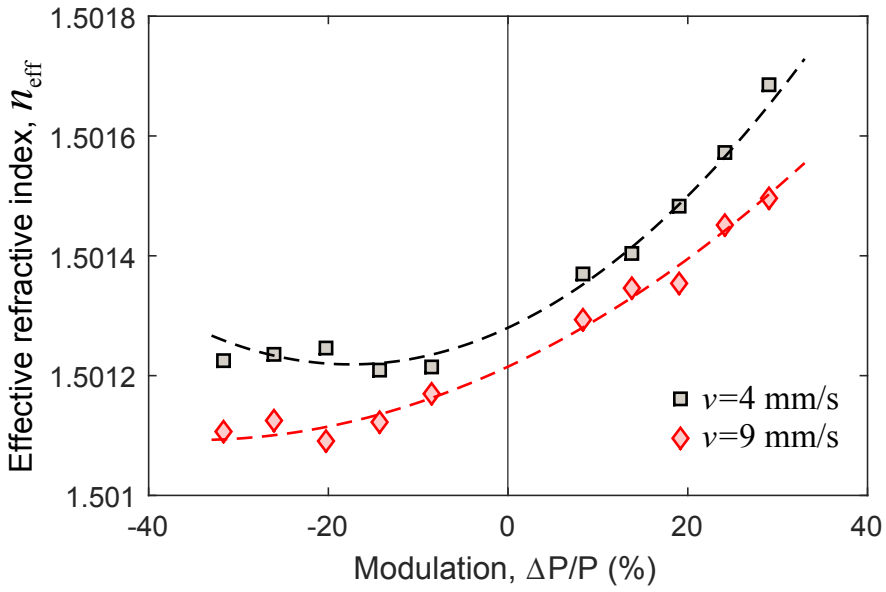

Fig. 3.7: Characterisation of waveguide Bragg gratings. n_{eff} is calculated from the intersection of the polynomial fits (dotted lines) and the vertical solid line. It was found that $n_{\text{eff}} = 1.50128$ and 1.501215 for waveguides fabricated with 4 and 9 mm/s translation speeds respectively.

in the backward direction under the following condition (the Bragg condition):

$$\lambda_B = 2\Lambda n_{\text{eff}}, \tag{3.3}$$

where λ_B is the wavelength of light, Λ is the spatial period of the grating and n_{eff} is the effective refractive index of the guided mode. In the experiment, we periodically vary the laser power, which modulates the magnitude of the refractive index modification, to fabricate the waveguide Bragg grating. Realisation of waveguide Bragg grating, and the measurement of Bragg wavelength as a function of the modulated laser power enable us to evaluate n_{eff} of the optical waveguide with zero modulation in refractive index.

Originally, fibre Bragg gratings were demonstrated by K. O. Hill [52] in 1978 (see also [53]), which have now become a key device for applications in telecommunications [54], astronomy [55] and sensing technology [56]. Our primary objective is to fabricate and characterise waveguide Bragg gratings to estimate n_{eff} of an optical waveguide. In this context, G. D. Marshall et al. [30] (see also Ref. [31]) and G. Brown et al. [32] reported ultrafast laser inscribed waveguide Bragg gratings using single scan and multiscan techniques respectively. We translate the glass substrate (Eagle^{2000}) through the focus of a 0.4 NA lens, and the laser power is externally modulated periodically with time using an acousto-optic modulator (AOM, Gooch & Housego). For fabrication, we

use the first order diffracted beam from the AOM which was driven with a square wave from a programmable signal generator (Tektronix). We denote the extreme values of the laser power by P and $P + \Delta P$. Two sets of 30-mm-long (translation speeds $v = 4$ and 9 mm/s) waveguide Bragg gratings were fabricated with $P = 220$ nJ pulse energy and 260 nm grating period. For each set ΔP was varied from $+0.3P$ to $-0.3P$. These gratings were characterised by launching broadband supercontinuum light and the wavelength of the first order Bragg reflection is measured. Fig. 3.7 shows the variation of n_{eff} as a function of modulation in laser power; the dotted lines are the 2-nd order polynomial fit. Now the effective refractive index of the optical waveguides without any Bragg grating (modulation, $\Delta P = 0$) is calculated from the intersection of the polynomial fits and the vertical solid line. We found that $n_{\text{eff}} = 1.50128$ and 1.501215 for waveguides fabricated with 4 and 9 mm/s translation speeds respectively. As a final note, it should be highlighted that the methods of estimating the effective refractive index of the guide mode will be useful to demonstrate analogous magnetic field (see Section 4.2.6) and to experimentally simulate one-dimensional two-particle Hubbard model in photonic platform (see Chapter 6).

3.5 Chapter summary

In this chapter, we presented a brief introduction to the ULI technique, and the characterisation of optical waveguides and directional couplers. In the following chapters we will use the slit beam shaping technique to fabricate optical waveguides in the low repetition rate (LRR) regime using the transverse writing geometry (TWG); see Table 3.1 for the other fabrication parameters. We aim to find the mapping between various solid-state systems and engineered waveguide arrays, and thus demonstrate the photonic analogue of solid-state phenomena using the basic fabrication and characterisation techniques presented in this chapter. Other details of fabrication parameters and characterisation, as required, will be presented in the respective chapters.

This page is intentionally left blank.

Chapter 4

Flat-band lattices

4.1 Introduction

Processes leading to the localisation of the electronic wavefunction in crystalline solids have long been studied in theoretical physics. One of the most celebrated localisation effects is Anderson localisation [57], which occurs due to the presence of disorder. The presence of external fields and particle interactions can also cause localisation. In recent years, these intriguing effects are being experimentally observed in the photonic domain, using arrays of carefully engineered coupled optical waveguides. Localisation caused by disorder [58], analogous external field [22, 59] and Kerr nonlinearity [60] have already been realised in photonics. Another type of localisation can result due to the presence of a non-dispersive (or flat) band in the energy spectrum. Originally, flat-band Hubbard models were analysed in the context of magnetism, where electrons populating the flat band were found to contribute to unusual ferromagnetic ground states [61]. Recently, the interplay between flat-band localisation and correlated disorder was studied in Ref. [62] and the transport of light in various flat-band lattices, such as Lieb [63–66], Kagome [67, 68], rhombic [69] and sawtooth [70], have been experimentally investigated.

In this chapter, two different photonic lattices, a quasi-one-dimensional rhombic lattice and a two-dimensional Lieb lattice will be considered – both of which support two dispersive and a perfectly non-dispersive (flat) band in the nearest neighbour tight binding approximation. In the experiment, we excite a superposition of flat-band eigenmodes at the input of the lattice and show the diffractionless propagation of the input states due to their infinite effective mass. As also proposed by S. Longhi in Ref. [71], we suggest that a photonic rhombic lattice, when implemented with a synthetic gauge field, will allow the observation of Aharonov-Bohm photonic caging.

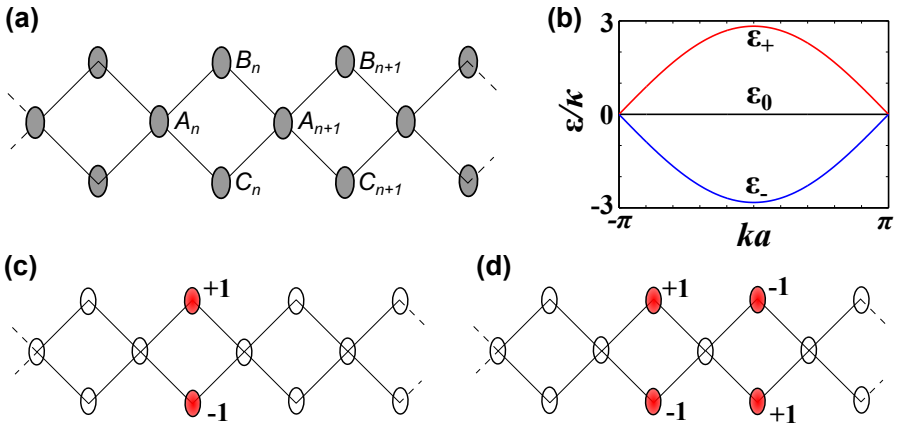

Fig. 4.1: (a) A quasi-one-dimensional rhombic lattice where the unit cell contains three lattice sites (A, B and C). (b) In the nearest neighbour tight binding model, the lattice supports three energy bands. The upper and the lower bands are dispersive. The middle one is perfectly flat. The span of the Brillouin zone: ($-\pi \leq ka \leq \pi$). At $k = \pm\pi/a$ the three bands intersect each other. (c) Flat-band modes 1: a superposition of flat-band eigenmodes can be excited at the input of the lattice if the B and C sites of a unit cell are excited with equal intensities ($I_B = I_C$) and opposite phases ($\phi_B = \phi_C \pm \pi$). (d) Flat-band modes 2: the flat-band modes can also be excited if the B and C sites of two neighbouring unit cells are excited with equal intensities ($I_B = I_C$) and alternating phases ($\phi_B = \phi_C \pm \pi$).

4.2 Photonic rhombic lattice

In this section, we consider a quasi-one-dimensional lattice, the rhombic lattice [71, 72], which supports three energy bands, including a perfectly flat-band in the middle.

4.2.1 Band structure of a rhombic lattice

In our previous discussions, we have seen that the evolution of light-waves in a photonic lattice, a periodic array of coupled optical waveguides, is governed by a Schrödinger-like equation which was derived from Maxwell's equations, using the scalar-paraxial approximation (Section 2.2). In a one-dimensional photonic lattice, the Schrödinger-like equation takes the following form

$$i\lambda\frac{\partial}{\partial z}\psi(x,z) = \Big[-\frac{\lambda^2}{2n_0}\frac{\partial^2}{\partial x^2} - \Delta n(x)\Big]\psi(x,z). \tag{4.1}$$

Here we consider a quasi-one-dimensional photonic rhombic lattice as shown in Fig. 4.1 (a). The unit cell contains three lattice sites (A, B and C) with site energies (or propagation constants) β_a, β_b and β_c respectively. In the nearest neighbour approximation, the

spinless tight-binding Hamiltonian of the rhombic lattice in real space reads

$$\begin{aligned}\hat{\mathcal{H}}_{TB} = \; & -\sum_n \big[\beta_a a_n^\dagger a_n + \beta_b b_n^\dagger b_n + \beta_c c_n^\dagger c_n + \kappa a_n^\dagger b_n + \kappa a_n^\dagger c_n + \kappa a_n^\dagger b_{n-1} \\ & + \kappa a_n^\dagger c_{n-1} + \kappa b_n^\dagger a_n + \kappa b_n^\dagger a_{n+1} + \kappa c_n^\dagger a_n + \kappa c_n^\dagger a_{n+1}\big], \end{aligned} \tag{4.2}$$

where $\{a_n^\dagger, b_n^\dagger, c_n^\dagger\}$ and $\{a_n, b_n, c_n\}$ are the creation and annihilation operators of the localised Wannier states $\{|A_n\rangle, |B_n\rangle, |C_n\rangle\}$ respectively and κ is the nearest neighbour hopping amplitude (or coupling constant). Using the Fourier transformation, $O_k = \frac{1}{\sqrt{N}} \sum_n O_n e^{ikan}$, where N is the number of unit cell, the Fourier transformed Hamiltonian in k-space is described by the following 3×3 matrix:

$$\hat{\mathcal{H}} = \sum_k \begin{pmatrix} a_k^\dagger & b_k^\dagger & c_k^\dagger \end{pmatrix} \begin{bmatrix} -\beta_a & -\kappa(1+e^{ika}) & -\kappa(1+e^{ika}) \\ -\kappa(1+e^{-ika}) & -\beta_b & 0 \\ -\kappa(1+e^{-ika}) & 0 & -\beta_c \end{bmatrix} \begin{pmatrix} a_k \\ b_k \\ c_k \end{pmatrix} \tag{4.3}$$

Now considering that the three sites in the unit cell contain identical optical waveguides i.e. $\beta_a = \beta_b = \beta_c \equiv 0$, and diagonalizing the Fourier transformed Hamiltonian, the following dispersion relations are obtained [71, 73]:

$$\begin{aligned} \varepsilon_\pm(k) &= \pm 2\kappa\sqrt{1+\cos(ka)}, \\ \varepsilon_0(k) &= 0, \end{aligned} \tag{4.4}$$

where a is the lattice constant, ε_0 is the energy of the non-dispersive (flat) band, $\varepsilon_\pm$ represent the upper and the lower dispersive bands respectively. The span of the Brillouin zone is given by $(-\pi \leq ka \leq \pi)$. At $k = \pm\pi/a$ the three bands intersect each other; see Fig. 4.1 (b).

To solve the eigenvalue equation, $i\partial\Psi/\partial z = \hat{\mathcal{H}}_{TB}\Psi$, the wavefunction Ψ is expanded in terms of localised Wannier function [see Eq. (2.30)] to obtain the following coupled-mode equations in the nearest neighbour approximation:

$$\begin{aligned} i\frac{\partial}{\partial z}A_n &= -\kappa\big(B_n + B_{n-1} + C_n + C_{n-1}\big), \\ i\frac{\partial}{\partial z}B_n &= -\kappa\big(A_n + A_{n+1}\big), \\ i\frac{\partial}{\partial z}C_n &= -\kappa\big(A_n + A_{n+1}\big), \end{aligned} \tag{4.5}$$

where A_n, B_n and C_n are the electric field amplitudes (of the light waves) at the A, B and C sites of the n-th unit cell respectively. The intensity distribution at the output of the photonic lattice, for a given input excitation, is obtained by numerically solving

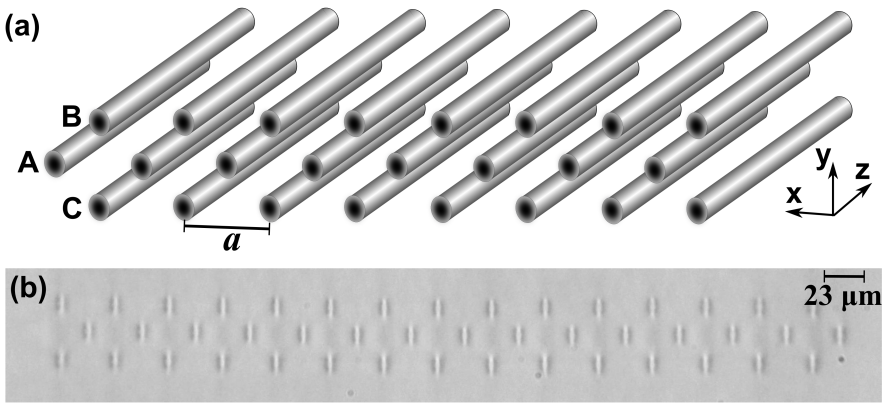

Fig. 4.2: (a) A photonic rhombic lattice. The lattice constant is a. (b) White-light-transmission micrograph of the facet of a finite photonic rhombic lattice with fifteen unit cells. Each waveguide was observed to support a well confined fundamental mode at 780 nm wavelength with mode field diameters 8.3 μm and 7.0 μm along the y-axis (vertical) and x-axis (horizontal), respectively.

Eq. (4.5). In the nearest neighbour approximation, a superposition of flat-band eigenmodes can be excited at the input of the lattice if (a) the B and C sites of a unit cell are excited with equal intensities ($I_B = I_C$) and opposite phases ($\phi_B = \phi_C \pm \pi$) or (b) the B and C sites of two neighbouring unit cells are excited with equal intensities ($I_B = I_C$) and alternating phases ($\phi_B = \phi_C \pm \pi$); see Fig. 4.1 (c, d). [These are just two different ways of exciting the flat-band states. Of course, there are other input states to do that.]

4.2.2 Fabrication of photonic rhombic lattices

Twelve sets of photonic rhombic lattices (waveguide-to-waveguide separation, $a/\sqrt{2} = 15$ μm to 26 μm in steps of 1 μm) were fabricated inside a 70-mm-long glass (Corning Eagle^{20000}) substrate. Each waveguide was fabricated by translating the glass substrate once through the focus of a femtosecond laser beam at 8 mm/s. Fabrication parameters were optimised to inscribe well-confined single-mode waveguides at 780 nm wavelength. Each lattice contains fifteen unit cells. All the experiments were performed using the lattice with $a/\sqrt{2} = 23$ μm for which $\kappa = 0.01$ mm^{-1} and the next-nearest neighbour coupling constant was insignificant (for the maximum propagation distance). In Fig. 4.2 (b), a white-light-transmission micrograph of the facet of the lattice is shown.

4.2.3 Experimental setup

The experimental setup to excite the desired lattice sites at the input of the photonic rhombic lattice is shown in Fig. 4.3. First order diffraction "spots" generated by a

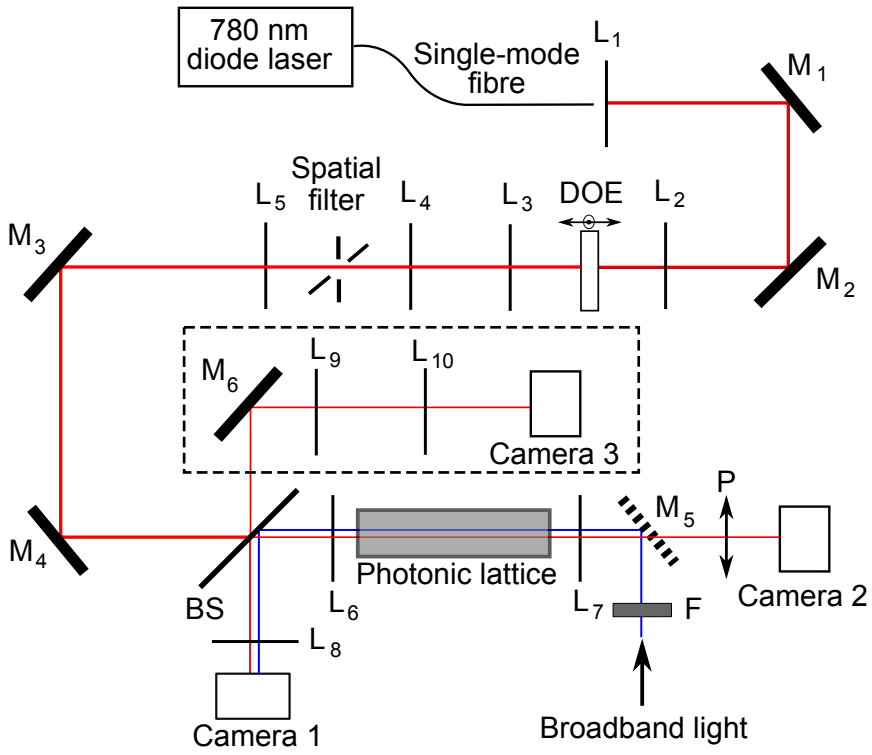

Fig. 4.3: Experimental setup for exciting the desired lattice sites at the input of the photonic rhombic lattice. L_1-L_{10} are convex lenses, M_1, M_2 are silver-coated mirrors and BS is a beam splitter $(50 : 50)$. A zero-order nulled diffractive optical element (DOE) generates a square array of diffraction-order "spots". A rectangular spatial filter (with adjustable height and width) blocks all the higher order diffraction "spots" except for the first order "spots". The spatial filter also helps to launch the desired number of first order spots. The separation among the four Gaussian spots was varied by translating the DOE along the propagation direction (z) of the laser beam. The relative phases of the four "spots" can be controlled by translating the DOE in the x-y plane. The output intensity distribution is measured in Camera 2. A polariser (P) passes only vertically polarised light. The set-up inside the dotted rectangle is used to observe the interference pattern of the input modes in the Fraunhofer regime.

zero-order nulled, binary-phase, square-checker-board diffractive optical element (DOE) were used to launch four Gaussian spots with almost equal intensities (the measured relative standard deviation, (RSD)$\approx$ 4 %). A rectangular spatial filter, with adjustable height and width, placed at the image plane of lens L_4, passes the four spots including a very weak central one while filtering all other higher spatial frequencies. The size of these spots on the lattice facet is determined by the diameter of the beam entering lens L_6 and its focal length. On the other hand, the spacing between the spots can be controlled via the distance of the DOE from lens L_2 (by translating it along the propagation

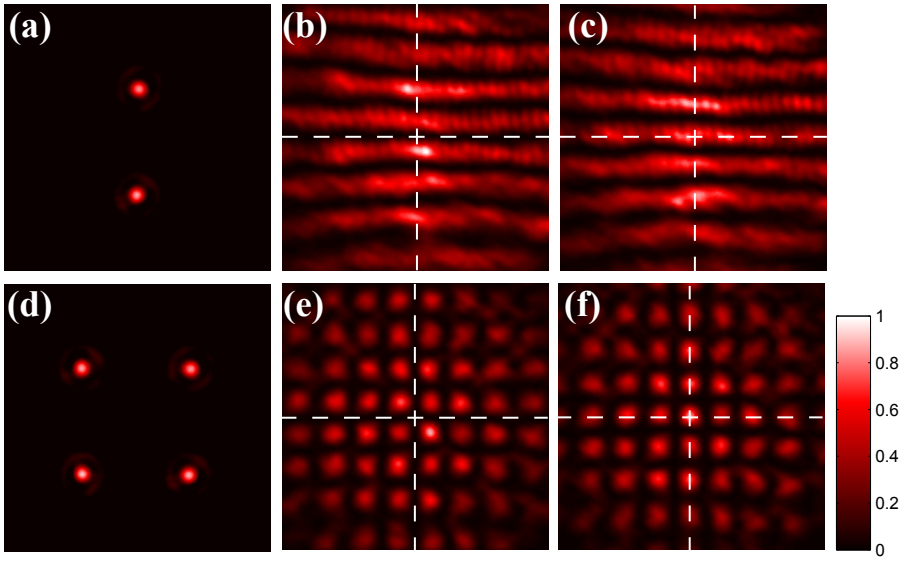

Fig. 4.4: (a, d) Two different input intensity distributions used in the experiment to excite flat-band eigenmodes. The measured values of relative standard deviation (RSD) of the intensities are 3.9% and 4.1% respectively. (b, e) The interference pattern of the flat-band modes in the Fraunhofer regime. (c, f) The interference pattern of the equal phase modes in the Fraunhofer regime.

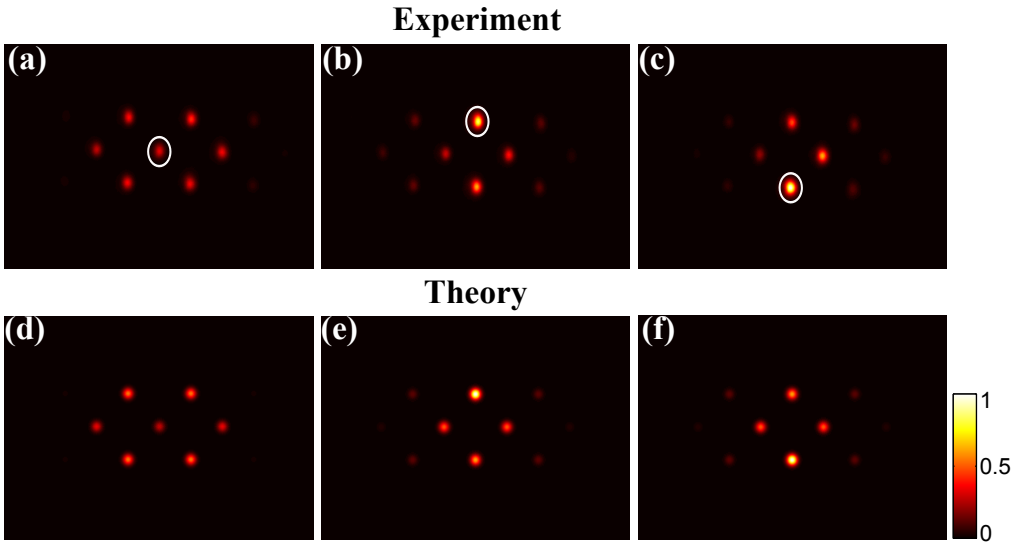

Fig. 4.5: (a-c) Experimentally observed intensity distributions at the output of a 70-mm-long photonic rhombic lattice when A, B and C sites (indicated by the white circles) were excited at the input respectively. The simulated output intensity distributions for A, B and C site excitation are shown in (d-f) respectively. The images are normalised such that the total power for each image is 1.

direction (z) of the laser beam). The independent control over the spacing and size of the four spots enables the excitation of the four desired waveguides (B and C sites) in the lattice. The relative phases of the four "spots" can be controlled by translating the

DOE in the x-y plane. Camera 1 (L_8 is a tube lens) is used to observe the input facet of the lattice. 780 ± 10 nm light is filtered from a broadband source and illuminates the output end of the lattice, in order to observe the guided modes for each waveguide using Camera 1. Viewing the modes in this manner allowed us to launch light specifically to the modes of the lattice. Camera 2 is used to observe and measure the output intensity distribution. The polariser (P) in front of Camera 1 passes only the vertically polarised (which is one of the eigen polarisation of the waveguides) light. Hence, our measurements are not affected by polarisation dependent coupling.

The relative phases among the Gaussian "spots" were measured by observing the interference pattern in the Fraunhofer regime; see the set-up inside the dashed rectangle in Fig. 4.3. The measured interference patterns for the two different types of flat-band modes [see Fig. 4.1 (c, d)] for the photonic rhombic lattice are shown in Fig. 4.4 (b, e). Fig. 4.4 (c, f) are the interference patterns for the equal-phase modes, the input states where relative phases among all the Gaussian spots are zero.

4.2.4 Single site excitations

Fig. 4.5 (a-c) present the output intensity distributions when single A, B and C sites were excited individually at the input respectively. Fig. 4.5 (d-f) present the corresponding simulated intensity distributions obtained by solving Eq. (4.5). It should be noted that the light contained at the initially excited A site (indicated by the white circle) is less than that measured at B and/or C sites. In other words, light injected into A sites diffracts more than light injected into B and/or C sites. Indeed, the calculation of the overlap between the input state and the eigenstates of the three bands show that the A site excitation excites more eigenstates from the dispersive bands compared to B (and/or C) site excitation.

4.2.5 Excitation of flat-band modes

To excite the flat-band modes we couple light into the B and C sites of a unit cell with equal intensity and opposite phases (the flat-band modes 1; see Fig. 4.4). We observe that the light remains localised to the excited sites without tunnelling to other waveguides; see Fig. 4.6 (a). This localisation effect is due to the interference effect. When the flat-band modes are excited by launching light into the B and C sites with equal intensities and opposite phases, the light cannot tunnel to the nearest A sites due to destructive interference. It should be noted that this can only occur if the next-nearest

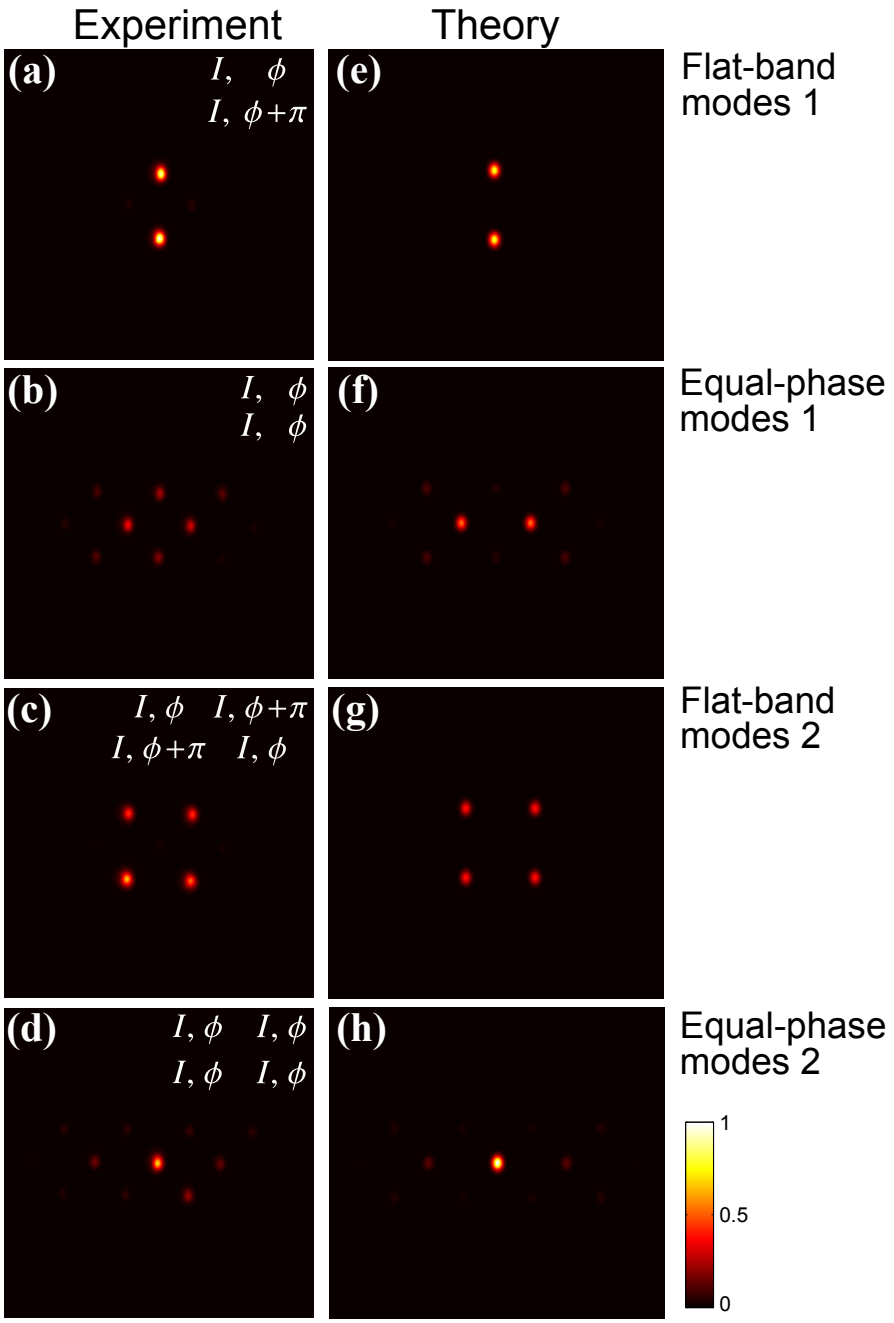

Fig. 4.6: Experimentally observed flat-band modes (a, c) and the equal-phase modes (b, d). The intensities and relative phases of the input modes are shown on the top-right of each image. The output intensity distribution when the B and C sites of a primitive cell were excited with equal intensities, opposite (a) and equal (b) phases. When the flat-band mode is coupled to the B and C sites, light cannot tunnel to the nearest A sites due to destructive interference. Localised flat-band modes can also be observed by coupling the B and C sites of the neighbouring primitive cells with equal intensities and alternating phases (c). When these four B and C sites were excited with equal intensities and equal phase, the mode in not localised (d). The images are normalised such that the total power for each image is 1.

neighbour coupling is insignificant. To confirm that we are observing the correct sensitivity of phase profile, we couple light into the B and C sites with equal intensities and equal phases (the equal-phase modes 1). As shown in Fig. 4.6 (b), this input mode is not localised.

The above-mentioned input state is not unique to excite the flat-band modes. In the nearest neighbour approximation, the flat-band modes can also be excited if the B and C sites of two neighbouring unit cells are excited with equal intensities ($I_B = I_C$) and alternating phases ($\phi_B = \phi_C \pm \pi$), and the localised output intensity distribution for this second flat-band mode is shown in Fig. 4.6 (c). In the next step we excited these four waveguides with equal intensities and equal phase (the second equal-phase mode). These modes are not localised [Fig. 4.6 (d)] as would be expected.

4.2.6 Future scope: Aharonov-Bohm photonic caging

In comparison to two-dimensional photonic lattices, the rhombic lattice we have investigated here is a greatly simplified system which can be used to study complex phenomena. In particular, synthetic gauge fields are one of the exciting routes to engineer the band structure of photonic lattices. In the presence of magnetic fields, various interesting phenomena, such as the Hofstadter spectrum and the fractional quantum Hall effect [74] and topologically protected chiral edge modes [75–77], can be observed in suitable lattice geometries. As we show, a photonic rhombic lattice can be used in conjunction with synthetic gauge fields, to observe Aharonov-Bohm photonic caging, a magnetic field induced localisation effect which occurs due to the destructive interference at some specific values of magnetic flux; see [71, 73, 78]. The experimental implementation of a synthetic gauge field in a photonic lattice is an experimental challenge, and it requires an engineered lattice where a photon tunnelling along a closed loop on the lattice will acquire a non-vanishing phase which is analogous to an Aharonov-Bohm phase. In principle, it can be realised by generating complex-valued hopping amplitudes. As proposed in Ref. [71], a circular bending and periodic modulation of the propagation constant (which can be realised by changing the translation speed) of the waveguides along the z direction, would generate a magnetic flux in a photonic rhombic lattice. Considering a rhombic lattice [see Fig. 4.7] in a gauge field with Φ flux per

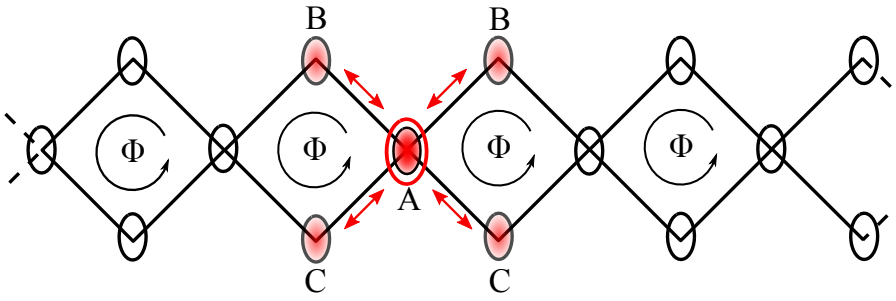

Fig. 4.7: Aharonov-Bohm caging in a photonic rhombic lattice in the presence of a synthetic magnetic flux, $\Phi = \pi$ per plaquette. When a single A site is excited at the input, the light intensity at the excited lattice site will periodically oscillate between 1 and 0 along the propagation (z) direction. Due to photonic Aharonov-Bohm caging, the light intensity is locked into the initially excited A site and its nearest neighbour sites (four B and C sites).

plaquette, the dispersion relation becomes [71, 73]:

$$\begin{aligned} \varepsilon_{\pm}(k) &= \pm 2\kappa\sqrt{1+\cos(\Phi/2)\cos(ka-\Phi/2)}, \\ \varepsilon_{0}(k) &= 0. \end{aligned} \tag{4.6}$$

For $\Phi = \pi$, the energy spectrum consists of three non-dispersive (flat) bands. In this situation, if a single A site is excited at the input, the light intensity at the excited lattice site will periodically oscillate between 1 and 0 along the z direction. Due to photonic Aharonov-Bohm caging, the light intensity is locked into the initially excited A site and its nearest neighbour sites (four B and C sites).

The possibility to realise Aharonov-Bohm photonic caging is investigated by considering a photonic rhombic lattice where the propagation constants of the lattice sites are modulated in the following way:

$$\begin{aligned} \beta_A &= 2n\Delta\beta + K\sin(\omega z), \\ \beta_B &= (2n+1)\Delta\beta + K\sin(\omega z + \phi), \\ \beta_C &= (2n+1)\Delta\beta + K\sin(\omega z - \phi), \end{aligned} \tag{4.7}$$

where $\Delta\beta = n_0 a/(2R\lambda)$ is the linear gradient of the propagation constant (along the lattice axis), which can be realised by circularly curving the photonic lattice with a radius of curvature, R. Here, K and ω are the amplitude and frequency of the sinusoidal modulation of the propagation constant respectively, which can be realised by sinusoidally changing the translation speed of fabrication; see Section 6.4. Note that the propagation

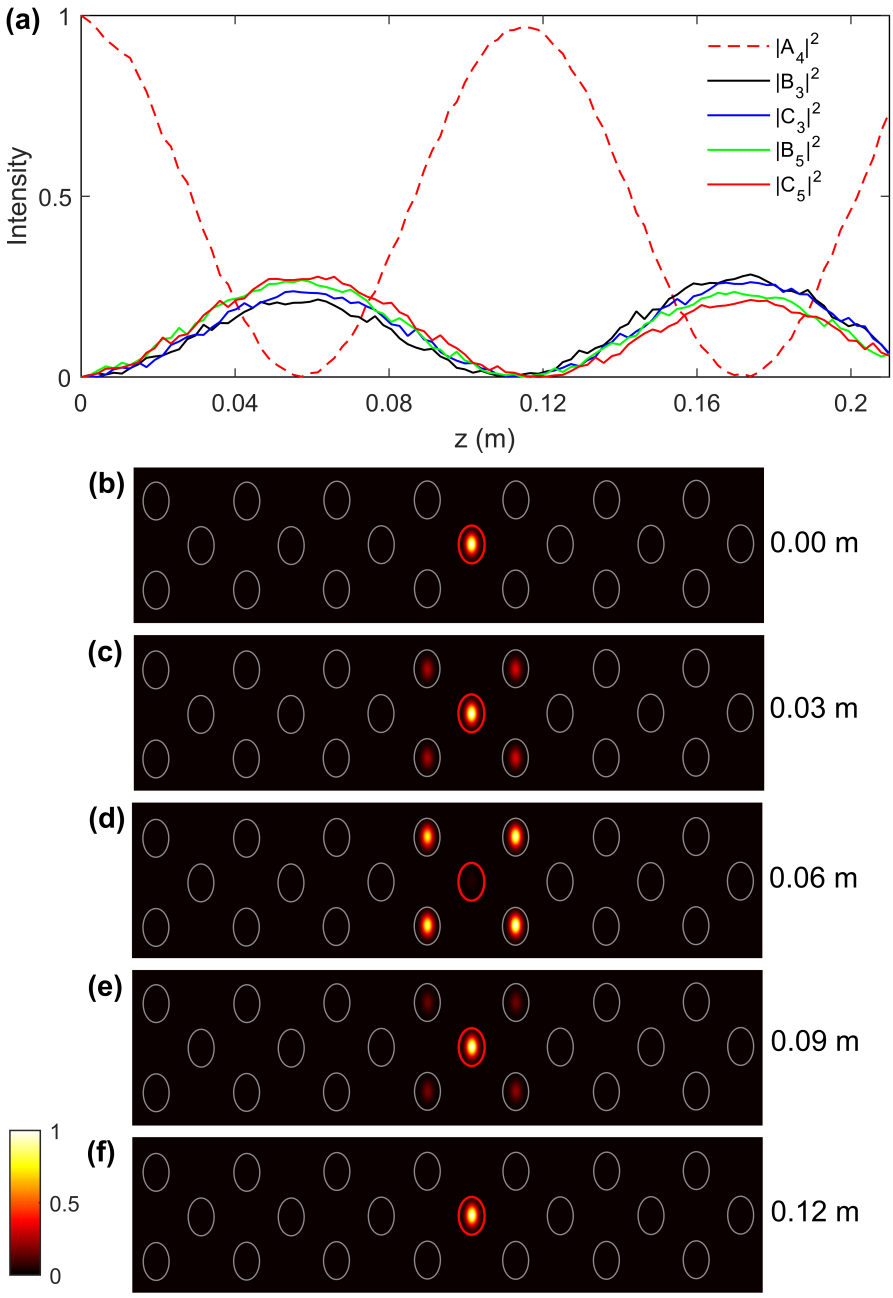

Fig. 4.8: (a) Numerically calculated evolution of light intensity which is governed by Eq. (4.7) and (4.8) for an engineered photonuc rhombic lattice. Here, $|A_4(z=0)|^2 = 1$, $\kappa = 0.035$ mm^{-1}, $\omega/\kappa = 12.82$, $\Delta\beta = \omega$, $K/\omega = 2$ and $\phi = \pi/2$. The observed inequality of light intensity at $B_{3,5}$ and $C_{3,5}$ is due to the fact that $\omega/\kappa \to \infty$ (high frequency driving) is not truly satisfied. (b-f) Output intensity distributions at different values of z, indicated on the right side of each image. The red circle, in each image, indicates the A site that was excite at the input.

constants of the B sites and the C sites modulate with a 2ϕ phase difference. It should be highlighted that a similar driving scheme was originally proposed in Ref. [71]. In the nearest neighbour tight binding approximation, the coupled mode equations for a

photonic rhombic lattice with the above-mentioned driving is given by

$$\begin{aligned}
\Big[i\frac{\partial}{\partial z}+\beta_A\Big]A_n &= -\kappa\big(B_n+B_{n-1}+C_n+C_{n-1}\big),\\
\Big[i\frac{\partial}{\partial z}+\beta_B\Big]B_n &= -\kappa\big(A_n+A_{n+1}\big),\\
\Big[i\frac{\partial}{\partial z}+\beta_C\Big]C_n &= -\kappa\big(A_n+A_{n+1}\big),
\end{aligned} \tag{4.8}$$

In the absence of modulation ($K=0$), the effective tunnelling among the nearest neighbour lattice sites is suppressed due to the propagation constant mismatch. However, the tunnelling can be restored for $K \neq 0$, under the resonance condition, $\Delta\beta = \nu\omega$ ($\nu = 1, 2, 3, ...$). Here, we consider the limit of high frequency driving ($\omega \gg \kappa$), and $\Delta\beta = \omega$ (i.e. $\nu = 1$). Regardless the value of K/ω, the numerical calculation shows that the associated Floquet quasienergy spectrum (see Section 7.2) consists of three flat bands when $\phi=\pi/2$.

Considering a driven photonic rhombic lattice, described by Eq. (4.7) and (4.8), we calculated the evolution of light intensity at the A site that was excited initially; see Fig. 4.8. The driving parameters are: $\kappa=0.035$ mm^{-1}, $\omega/\kappa=12.82$, $\Delta\beta=\omega$, $K/\omega=2$ and $\phi=\pi/2$. The photonic caging is clearly observed in Fig. 4.8.

4.3 Photonic Lieb lattice

In this section, we consider an edge centred square lattice (or the Lieb lattice) and experimentally demonstrate the excitation of localised flat-band modes. Although the concept is very similar to what we have already discussed in the previous section, the fabrication is more challenging in this case as the Lieb lattice has a two-dimensional geometry. First, we discuss the band structure in the nearest neighbour tight-binding model. We then present fabrication, characterisation and excitation of different bands.

4.3.1 Band structure of a Lieb lattice

In the scalar-paraxial approximation, the propagation of light-waves in a two dimensional array of optical waveguides is described by (see Section 2.2)

$$i\frac{\partial}{\partial z}E(x,y,z)=\left(-\frac{1}{2k_0n_0}\nabla_\perp^2-k_0\triangle n(x,y)\right)E(x,y,z)=\hat{H}E(x,y,z) \tag{4.9}$$

where $\nabla_\perp^2$ is the transverse Laplacian operator and $\hat{H}$ is the Hamiltonian that governs the wave propagation in the array of waveguides. Considering an edge-centred square

(Lieb) lattice, as shown in Fig. 4.9 (a), in the absence of external electric fields and in the limit of nearest neighbour tight binding approximation, the energy eigenvalues are given below [79, 80]

$$\begin{aligned} \varepsilon_{\pm}(\mathbf{k}) &= \pm 2\sqrt{\kappa_x^2 \cos^2(k_x a) + \kappa_y^2 \cos^2(k_y a)} \\ \varepsilon_0(\mathbf{k}) &= 0 \end{aligned} \tag{4.10}$$

where κ_x and κ_y are the hopping amplitudes (or coupling constants) for nearest neighbour sites along x and y directions. $\varepsilon_{\pm}$ are the energies of the upper and the lower bands, respectively, ε_0 represents the non-dispersive (flat) band; see Fig. 4.9 (c). The span of the Brillouin zone is given by $\{\pi/2 < k_x a, k_y a < \pi/2\}$. The three bands intersect at $k_x a = k_y a = \pi/2$, known as the M point. The dotted square in Fig. 4.9 (a) shows a unit cell of the lattice. There are four A sites at the corners of each cell; two B sites and two C sites lie on the edges. If the Lieb lattice is isotropic (i.e. $\kappa_x = \kappa_y$ everywhere), with insignificant next-nearest neighbour coupling, and the two B sites and two C sites of a unit cell are excited with equal intensities ($I_B = I_C$) and alternating phases ($\phi_B = \phi_C \pm \pi$), a superposition of eigenstates in the flat band can be excited. Here we demonstrate experimentally that the flat-band modes excited at the input of a photonic Lieb lattice do not diffract.

4.3.2 Fabrication of photonic Lieb lattices

Photonic Lieb lattices were fabricated using the ultrafast laser inscription technique inside a borosilicate glass (Corning Eagle^{2000}) substrate. Each of the waveguides in the lattice was written by translating the substrate material once through the focus of a 500 kHz train of sub-picosecond (350 fs) laser pulses of circularly polarised 1030 nm light. These laser pulses were generated by a Menlo BlueCut fibre laser system. To control the substrate translation, the substrate was mounted on high-precision air-bearing Aerotech x-y-z translation stages. The various laser writing parameters were optimised to produce low propagation loss single-mode waveguides for operation at a wavelength of 780 nm. The refractive index profile of the waveguides was controlled using the slit beam shaping method (see Section 3.2.3), by placing a slit directly in front of the 0.4 numerical aperture (NA) lens that was used to focus the laser inside the material. The effective NA's of the laser focus were calculated to be ≈ 0.2, and 0.3 in the axis perpendicular and parallel to the waveguide axis respectively. The final Lieb lattices were inscribed in a 7 cm long glass chip, and the individual waveguides exhibited a propagation loss of ≈ 1 dB/cm.

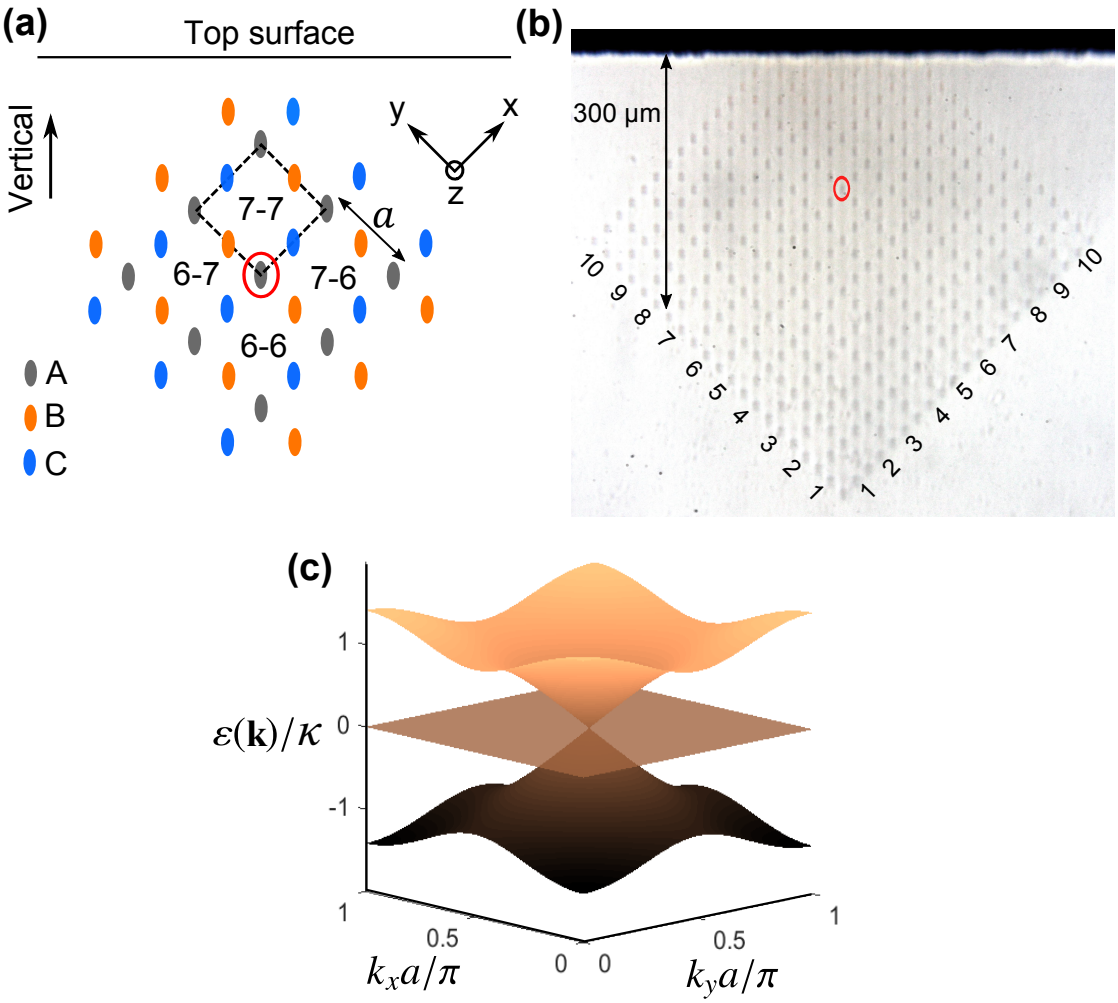

Fig. 4.9: (a) Edge centred square (or Lieb) lattice. The basis consists of three sites (A, B and C). All the measurements were performed near the circled A site (A_{7-7}) to avoid edge effects and effects due to lattice inhomogeneity with depth. The lattice constant is $a = 44$ μm, see also (b). (b) White-light-transmission micrograph of the facet of a finite Lieb lattice with 323 waveguides fabricated by femtosecond laser writing. Each waveguide supports only a single fundamental mode at 780 nm. The next-nearest neighbour coupling for a 7 cm long glass chip was observed to be negligible. To minimise the difference in the next nearest neighbour coupling constants along the x and y-axis, the lattice axes were rotated by 45° with respect to the vertical direction. (c) Representation of the three energy bands, including the flat band in the middle, for $\{k_x a, k_y a\} = \{0, \pi\}$, $\kappa_x = \kappa_y = \kappa$. The three bands (one flat and two dispersive) intersects at $k_x a = k_y a = \pi/2$.

Thirteen sets of complete Lieb lattices (lattice constant $a = 24$ μm to 48 μm in steps of 2 μm), with each containing 323 single-mode waveguides were fabricated. A white-light-transmission micrograph of the facet of the lattice with $a = 44$ μm is shown in

Fig. 4.9 (b). As shown in Fig. 4.9 (b), the lattice axes were rotated by $45°$, relative to the vertical axis. This rotation was performed in order to accommodate any asymmetry in the guided modes and minimise any potential differences in the nearest neighbour coupling coefficients for the x and y directions.

4.3.3 Investigation of disorder

It is well known that when writing waveguides using a femtosecond laser, depth dependent aberrations imparted on the laser beam by the air-glass interface can have a significant impact on the optical properties of the fabricated waveguides. This phenomenon will clearly change the properties of the lattice as a function of depth inside the material. To assess the impact of this on the homogeneity of the fabricated Lieb lattice we measure the fluctuation of coupling constant (off-diagonal disorder) and investigate the possibility of the variation of the propagation constant (diagonal defect) as a function of depth.

Off-diagonal disorder

Evanescently coupled two-waveguide couplers were fabricated at six different depths (100 μm to 600 μm in steps of 100 μm) with identical fabrication parameters used to inscribe the Lieb lattices. Each coupler was written using the same waveguide-to-waveguide separation and angle as the waveguides in the Lieb lattice. At each depth, five sets of seventeen couplers were fabricated, with each set consisting of couplers with interaction lengths ranging from 1 mm to 65 mm in steps of 4 mm. To characterise each coupler, light was injected into one of the waveguides, and the coupling constant was evaluated by measuring the observed ratio of the output intensities (see Section 3.3). For each depth, the mean and standard deviation of the evaluated coupling constant was obtained using the data for 85 couplers. This information is presented in Fig. 4.10, where it can be seen that the coupling constant, and the variance in the coupling constant, is constant with depth up to a maximum depth of 300 μm. After this depth, both the coupling constant and variance become a function of depth, with deeper structures exhibiting a progressively higher variance. We note that in future work the homogeneity of the lattice could be greatly improved by either using active optics techniques [45] to compensate for the depth dependent aberration, or by using large working distance immersion optics.

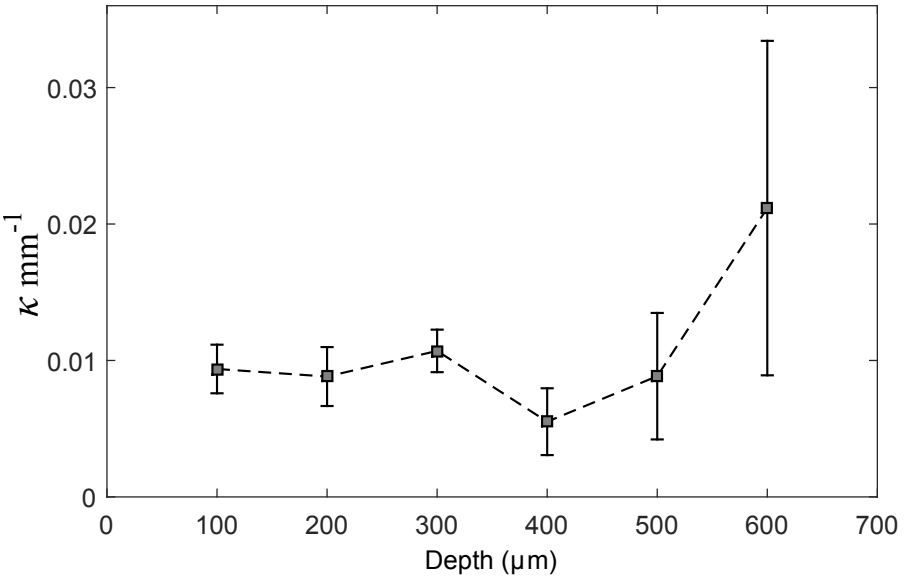

Fig. 4.10: Variation of coupling constant with depth. For each depth 85 couplers with different propagation lengths were measured to estimate the fluctuation in coupling constant. The error bars indicate the standard deviation from the mean coupling constant.

Diagonal disorder

In the previous section, we have investigated the presence of off-diagonal disorder assuming the fact that there is no diagonal disorder (random variations in waveguide propagation constants). To prove that the random variations in waveguide propagation constants is insignificant (locally), we performed a second set of experiments, where three sets of couplers (waveguide-to-waveguide separation, $d = 13$, 14 and 15 μm) with different interaction lengths were fabricated at a single depth inside the substrate. The waveguide-to-waveguide angle was set to 45°. The reduced waveguide-to-waveguide separation was used to reduce the coupling length. Coupling characteristics for these couplers were observed to be close to ideal, with near-complete transfer of power from the input waveguide to the other waveguide achieved after one coupling length; see Fig. 4.11. Since the complete transfer of energy from one waveguide to the another, in an evanescent field coupler, is only possible if the waveguides support modes with identical propagation constants, we conclude that local variations in waveguide propagation constants are negligible in our Lieb lattices. Hence, diagonal disorder is not significant.

4.3.4 Single site excitations

In order to avoid edge and lattice inhomogeneity effects, all optical measurements were performed by injecting light into the sites surrounding the A_{7-7} [circled in Fig. 4.9 (a,

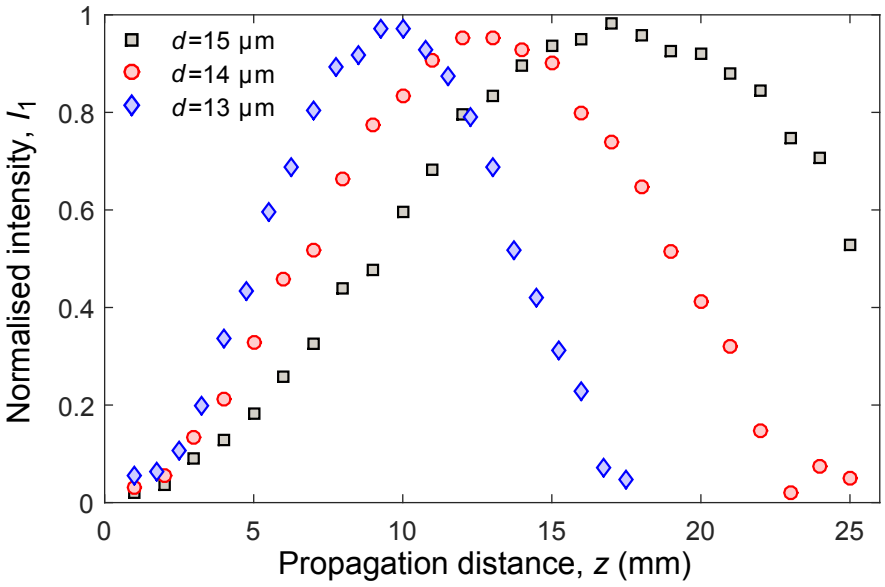

Fig. 4.11: Variation of coupling ratio with interaction length for three different waveguide-to-waveguide separations, d. This graph shows the full transfer of optical power from one waveguide to other. Interaction lengths for full transfer of power are 17.2 mm, 12.7 mm and 9.4 mm respectively.

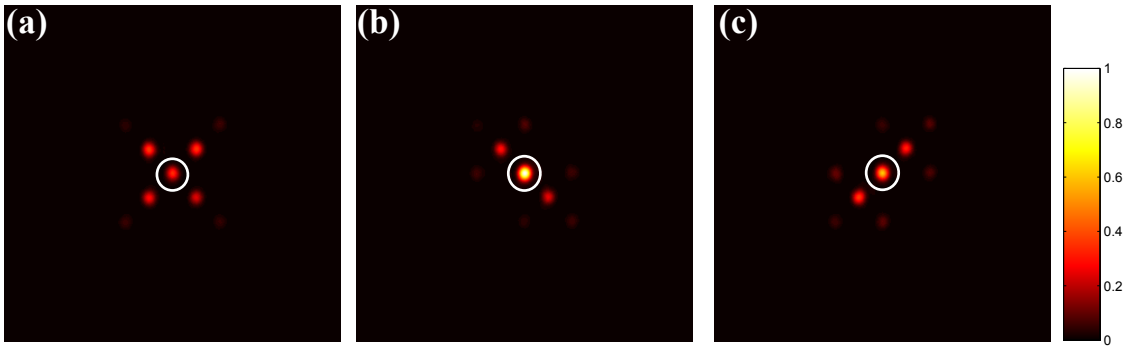

Fig. 4.12: Average diffraction patterns when A (a), B (b) and C (c) sites surrounding A_{7-7} were excited separately. The images are normalised such that the total output power is 1 for all the images. Estimated coupling constant for these diffraction patterns is 0.01 ± 0.001 mm^{-1}.

b)]. First, light was individually injected into the nine A, six B and six C sites surrounding the A_{7-7} site, and the output diffraction patterns were measured. For each type of injection site, the obtained diffraction patterns were normalised and averaged. The results of these measurements are shown in Fig. 4.12. The white circle in each of the images in Fig. 4.12 show the site excited at the input. The circled A site [in Fig. 4.12 (a)] contains less light than the circled B [in Fig. 4.12 (b)] or circled C site [in Fig. 4.12 (c)]. This obviously means that light injected into A sites diffracts more than

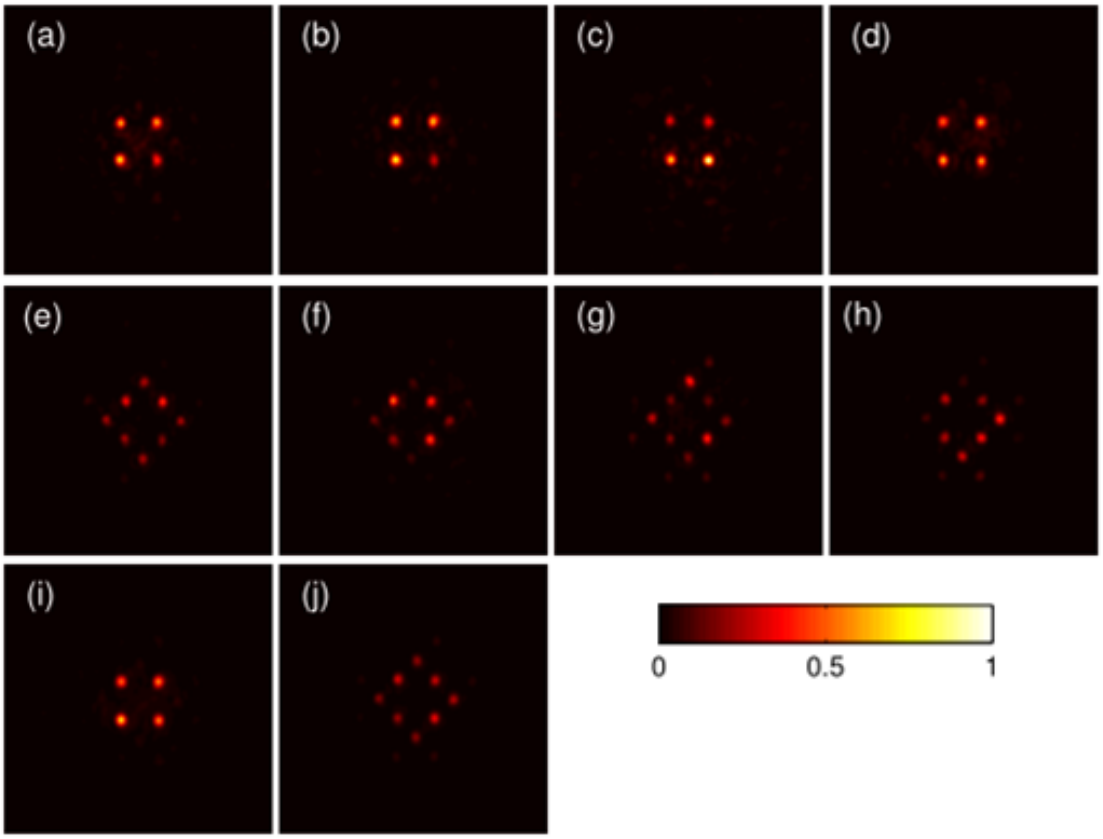

Fig. 4.13: (a-d) are the non-diffracting states observed at the output of the lattice when the flat-band state was launched into the B and C sites of the (7-7), (6-7), (7-6) and (6-6) cells respectively. When the equal-phase state was launched into the same cells, the output state is not localised, as shown by (e-h). (i) shows the average diffraction pattern of (a-d) and (j) is the average diffraction pattern of (e-h). Each image is normalised so that total intensity is 1. The field of view is approximately 210 μm by 210 μm. See also [64].

B or C sites, a phenomenon that has been recently shown by Guzman-Silva et al. [63]. From Fig. 4.12 (b) and Fig. 4.12 (c) we can say that the difference in κ_x and κ_y is comparable to the random fluctuation in coupling strength.

4.3.5 Excitation of flat-band states

As outlined in Section 4.2.3, and shown in Fig. 4.3, a diffractive optical element (DOE) and spatial filter combination were used to generate four Gaussian spots in a square array, with highly equal intensities (relative standard deviation, (RSD): 5.7 %) and alternating 0 and π phases. These four spots were then coupled to the B and C sites for a given unit cell of interest, in order to excite a superposition of eigenstates in the flat

band. The (7-7), (6-7), (7-6) and (6-6) primitive cells were each excited independently, and the output diffraction patterns observed in each case. Fig. 4.13 (i) shows the average of these four intensity distributions. As shown in Fig. 4.13 (a-d), which present the normalised intensity distributions observed at the output of the lattice, when the flat band state was excited, no significant tunnelling of light into the surrounding lattice sites could be observed after 7 cm of propagation. The flat-band state remains localised or non-diffracting. Importantly, this non-diffracting state was not observed in the lattices fabricated using lattice constants of ≤ 42 μm because the next nearest neighbour coupling in these lattices is non-negligible, destroying the flat band.

To confirm that the observed non-diffracting phenomena is unique to the phase and intensity distribution of the injected state, we injected an orthogonal state, where all the B and C sites of a unit cell are excited with nearly equal intensity (RSD: 4.2 $\%$) and equal phase (we call this the equal-phase state). As presented in Fig. 4.13 (e-h), this input state is not localised when injected into the (7-7), (6-7), (7-6) and (6-6) unit cells - a direct result of its near orthogonality to the flat-band-state.

4.4 Chapter summary

In this chapter, we have presented (a) a quasi-one-dimensional photonic rhombic lattice and (b) a two-dimensional photonic Lieb lattice, and experimentally excited a superposition of eigenmodes of the non-dispersive band of the respective lattices. We show that the flat-band modes remain localised to the initially excited waveguides. The reason for this effect is that the eigenmodes in the flat band are degenerate, so any superposition of them behave as an eigenmode. This type of localisation effect is sensitive to the modes excited at the input which makes this effect different from the disorder or nonlinearity induced localisations. Flat bands may be useful for diffractionless image transport [67]. In the presence of nonlinearities, we also expect novel types of nonlinear dynamics due to the absence of any kinetic terms in the effective Hamiltonian.

This page is intentionally left blank.

Chapter 5

Photonic Wannier-Stark ladder and photon-assisted tunnelling

5.1 Introduction

The energy spectrum and dynamics of tightly bound Bloch electrons in the presence of external electric and/or magnetic fields, has been extensively investigated in the literature of solid-state physics [16, 81–83], revealing many intriguing phenomena even in the absence of inter-particle interactions. Recent experimental advancement has enabled us to investigate these phenomena in the laboratory and elucidate the quantum physics of crystalline solids. As discussed in the previous chapters, the transport of light in a system of straight coupled optical waveguides, a straight photonic lattice, is analogous to the behaviour of a quasiparticle in a periodic potential with no external field. Importantly, the effect of an external field can also be realised in photonic systems. In recent years, many interesting phenomena, such as, coherent destruction of tunnelling in a double-well potential [84, 85], Bloch oscillations [18, 86–88], dynamic localisation [22, 89, 90], Bloch-Zener dynamics [91], Landau-Zener dynamics [92] have been investigated using the platform of photonic lattices. In this chapter, the experimental realisation of analogous static and alternating fields will be discussed using curved photonic lattices. This is the photonic analogue of a Bloch electron in a static and alternating electric field.

At first, the theory of Bloch oscillations and Wannier-Stark localisation is summarised briefly. In the limit of strong static field and weak inter-site tunnelling, we then demonstrate Wannier-Stark (W-S) localisation i.e. Wannier-Stark states strongly localised on a single lattice site. Finally, we show that by applying an analogous sinusoidal external field on the strongly localised W-S states, the inter-site tunnelling can be restored; which is historically known as photon-assisted tunnelling.

5.2 Bloch oscillations

A particle in free space moves with constant acceleration when a static force is applied. However, the motion of an electron in a periodic potential is significantly different. When a lattice is driven by a static electric field, an electron can perform oscillatory motion with time, known as Bloch oscillations. In the absence of external electric field, the eigenstates of an electron in a periodic potential are the Bloch states. An external static electric field destroys the degeneracy of these spatially delocalised Bloch states. Let us consider an electron in a one-dimensional periodic potential with an external static electric field, $\mathcal{E}_{dc}$, parallel to $\mathbf{k}$. The equation of motion of the electron is $\hbar dk/dt = -e\mathcal{E}_{dc}$, where e is the electronic charge. We assume that the electron is in the lowest Bloch band, $\epsilon = -2J\cos(ka)$ where J is the hopping amplitude and a is the lattice constant. In this situation the velocity of the electron in the momentum space is given by:

$$v = \frac{1}{\hbar}\frac{d\epsilon}{dk} = \frac{2Ja}{\hbar}\sin ka. \tag{5.1}$$

The variation of the position (x) of the electron, with the initial condition $x(t=0) = 0$, is given by

$$\begin{aligned} x(t) &= \int v(k)(dt/dk)dk = -\frac{2J}{e\mathcal{E}_{dc}}(\cos ka - 1) \\ &= -\frac{2J}{e\mathcal{E}_{dc}}(\cos \omega_B t - 1). \end{aligned} \tag{5.2}$$

$\omega_B = e\mathcal{E}_{dc}a/\hbar$ is the frequency of Bloch oscillations in real space.

5.3 Wannier-Stark localisation

In this section, we will first obtain the eigenstate and eigenvalues for a quasiparticle (e.g. electron) in a periodic potential and static electric field, and then discuss the limiting case when the eigenfunction becomes a Wannier function. Consider an electron in a one-dimensional lattice, driven by a static force $e\mathcal{E}_{dc}$, the Hamiltonian (with $\hbar = 1$) can be written as

$$\hat{\mathcal{H}} = e\mathcal{E}_{dc}a\sum_n n\hat{a}_n^\dagger\hat{a}_n - J\sum_n \hat{a}_n^\dagger(\hat{a}_{n+1} + \hat{a}_{n-1}), \tag{5.3}$$

where J is the nearest neighbour hopping amplitude and $\hat{a}_n^\dagger$ $(\hat{a}_n)$ is the creation (annihilation) operator at the n-th Wannier site. Expanding the wavefunction in terms of localised Wannier functions, the following secular equation is obtained for the expansion coefficient, c_n

$$\big(E/e\mathcal{E}_{dc}a - n\big)c_n = J/e\mathcal{E}_{dc}a(c_{n+1} + c_{n-1}). \tag{5.4}$$

Now as Eq. (5.4) has the same form as the recursion formula of a function satisfying Bessel equation, it is possible to show (see Ref. [16]) that the eigenstates and eigenfunctions of the Hamiltonian in Eq. (5.3) are

$$\phi_m = \sum_n \mathcal{J}_{n-m}(2J/e\mathcal{E}_{dc}a)\,|n\rangle\,, \tag{5.5}$$

$$\text{and} \quad E_m = (e\mathcal{E}_{dc}a)m \tag{5.6}$$

respectively, where $\mathcal{J}_\nu(2J/e\mathcal{E}_{dc}a)$ is the Bessel function of order ν with the argument $2J/e\mathcal{E}_{dc}a$. The span of the Brillouin zone is $\{-\pi/a \leq k \leq \pi/a\}$, $4J$ is the bandwidth, and $|n\rangle$ are the Wannier functions. Now let us consider the limiting case when $2J/e\mathcal{E}_{dc}a \to 0$. In this situation, there is only one term in Eq. (5.5), i.e. $|m\rangle$. In other words, in the limit of strong external electric field and weak inter-site tunnelling i.e. $2J/e\mathcal{E}_{dc}a \ll 1$, the spatial width of W-S state is less than the inter-site separation, a. In this limit, the W-S states will be localised to a single lattice site. The strongly localised electronic states on individual lattice sites can interact with photons and tunnel to the nearest lattice sites. This type of tunnelling with discrete energy exchange is known as photon-assisted tunnelling that has been observed in superconducting diodes [93], semiconductor superlattices [94] and quantum dots [95].

Electronic systems are not the only systems that exhibit W-S localisation and associated phenomena. Indeed, in recent years, such phenomena have been investigated in a variety of artificial systems, including cold atoms in optical lattices and photonic lattices. In fact, tunnelling suppression and photon-assisted tunnelling have been reported [96] in Bose-Einstein condensates in an optical lattice. We use photonic lattices, fabricated using the technique of ultrafast laser inscription (ULI) to investigate the dynamics of W-S states in a strong static electric field and weak inter-site tunnelling. We demonstrate strong localisation of the W-S state using curved photonic lattices, where the curvature is analogous to the static electric field in the electronic case. When the electric field exceeds a threshold value, we observe that the W-S state becomes localised to a single lattice site. We also demonstrate that a strongly localised W-S state becomes delocalised when an appropriate (specific frequencies and amplitudes) sinusoidal modulation is applied to the lattice.

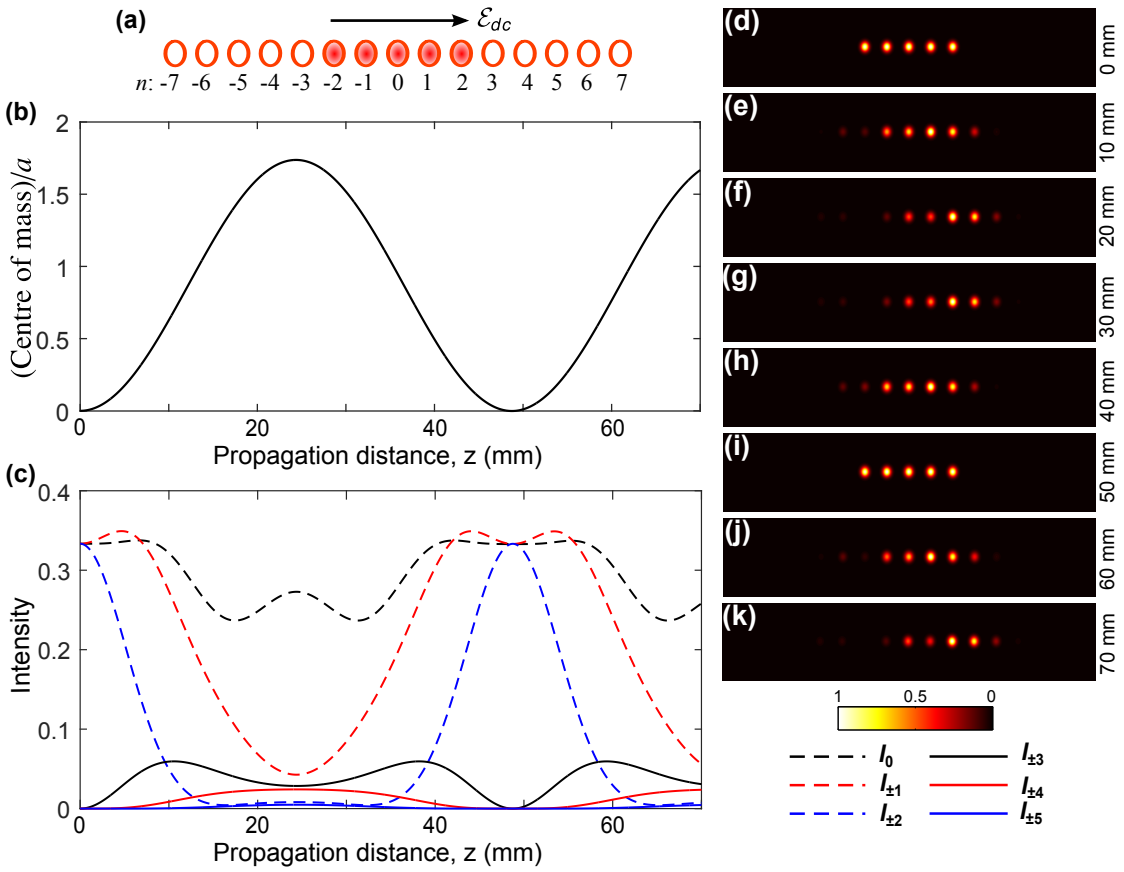

Fig. 5.1: Numerical simulation of photonic Bloch oscillations. (a) A one-dimensional lattice driven by a static field $\mathcal{E}_{dc}$. In photonic system the static field is realised by circularly curving the lattice. (b) The periodic motion of "centre of mass". (c) Evolution of optical intensity along the propagation distance, z, when five central waveguides are excited at the input. Parameters used in the simulation: $\kappa = 0.07$ mm^{-1}, $a = 16$ μm, $n_0 = 1.5$, $\lambda = 780$ nm, $R = 1.5$ m. Period of Bloch oscillations ≈ 48.5 mm. (d-k) Output intensity distributions at different values of z, indicated on the right hand side.

5.4 Photonic analogue of static electric field

As discussed in Section 2.5, the Schrödinger-like equation for a circularly curved one-dimensional photonic lattice is

$$i\lambda\frac{\partial}{\partial z}\Phi(x,z) = \Big[-\frac{\lambda^2}{2n_0}\frac{\partial^2}{\partial x^2} - \Delta n(x) + \frac{n_0}{R}x\Big]\Phi(x,z), \tag{5.7}$$

where (x, y, z) is the coordinate system moving with the lattice and the static external electric field, $\mathcal{E}_{dc}$, is given by $e\mathcal{E}_{dc} = n_0/R$, z plays the role of time. For well-confined single-mode waveguides, Eq. (5.7) can be solved using the tight binding approximation. When only the lowest band is excited, Eq. (5.7) gives the following coupled-mode

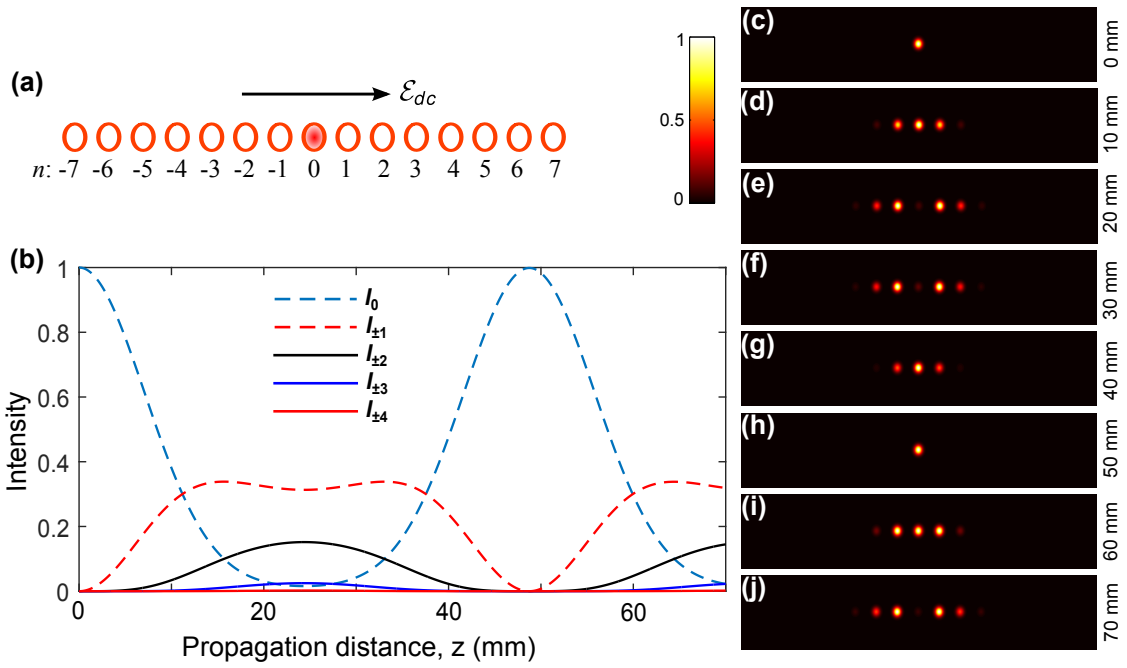

Fig. 5.2: Numerical simulation of photonic Bloch oscillations with single site excitation at the input. (a) A one-dimensional lattice driven by a static field $\mathcal{E}_{dc}$. (b) Evolution of optical intensity along the propagation distance, z, when only the central waveguide is excited at the input. Parameters used in the simulation: same as Fig. 5.1. (c-j) Output intensity distributions at different values of z. Note that the centre of mass of the particle does not move when a single site is excited because all the eigenstates are equally excited at the input.

equations:

$$i\frac{\mathrm{d}}{\mathrm{d}z}E_n = -\kappa(E_{n+1} + E_{n-1}) + n\alpha E_n \tag{5.8}$$

where E_n is the electric field amplitude in the n-th waveguide, κ is the nearest neighbour hopping amplitudes (or coupling constants) and $\alpha = n_0 a/R\lambda$ is the strength of the external linear potential. As discussed in the previous section, any input state will remain localised (i.e. the effective tunnelling will be insignificant) if $2\kappa R\lambda/n_0 a \ll 1$.

Let us consider a circularly curved one-dimensional (finite) photonic lattice with 15 lattice sites and theoretically investigate photonic Bloch oscillations. Consider the following achievable parameters of the tight binding Hamiltonian associated with Eq. (5.8): $\kappa = 0.07$ mm^{-1}, $a = 16$ μm, $n_0 = 1.5$, $\lambda = 780$ nm, $R = 1.5$ m. Note that the waveguides at the edges are not excited for these parameters (i.e. there is no edge effects). Fig. 5.1 (c) presents the evolution of light intensity when five central waveguides are excited at the

input with equal intensity and phase [see Fig. 5.1 (a)]. In this case, a periodic motion of the "centre of mass" [defined as $\sum_n x_n I_n / \sum_n I_n$, where x_n and I_n are the position and light intensity at the n-th lattice site] can be observed; see Fig. 5.1 (b). In the next step, we consider the single site excitation, i.e. only the central lattice site of the same photonic lattice is excited at the input; see Fig. 5.2. In this case, all the Bloch modes are equally excited at the input, and a breathing motion of optical intensity is observed [see Fig. 5.2 (c-j)] indicating no dynamic motion of the centre of mass.

5.5 Observation of W-S localisation

To investigate Wannier-Stark localisation, fifteen one-dimensional lattices (lattice constant $a = 16$ μm) were fabricated. The radius of curvature of the lattice was varied between 1.5 and 0.1 m ($R = 1.5, 1.4, ..., 0.1$ m). An additional straight lattice was also fabricated ($R = \infty$). The white light transmission micrograph of the facet of a lattice is shown in Fig. 5.3 (m). The refractive index profile of each waveguide was controlled using the slit beam shaping method; see Section 3.2.3. Each waveguide was inscribed by translating the 30-mm long glass sample (Corning Eagle^{2000}) at a translation speed of 8 mm/s, once through the focus of a 500 kHz train of 1030 nm femtosecond laser pulses. The ULI parameters were optimised to produce waveguides that were single-mode and well confined at 780 nm. The nearest neighbour coupling, κ, was measured to be 0.072 mm^{-1}, and the next nearest neighbour coupling was insignificant for the maximum propagation distance. Fig 5.3 shows the numerically calculated and experimentally measured output intensity distributions for the lattices with radii of curvature, $R = \infty$ (i.e. the straight lattice), 1.5 m, 1.2 m, 0.5 m, 0.3 m and 0.2 m. It is clear from Fig. 5.3 that the light becomes increasingly localised as the radius of curvature is reduced, as would be expected according to Eq. (5.5).

To investigate this phenomenon further, we fabricated 10-mm-long two-dimensional square lattices (lattice constant $a = 15$ μm in both the x and y directions), where each lattice curves only along x axis. For these lattices, the measured coupling strengths along x and y axis were 0.085 mm^{-1} and 0.095 mm^{-1} respectively. From simulations, the estimated value of next nearest neighbour coupling was 0.019 mm^{-1}. As can be seen from Fig. 5.4, localisation occurs only along the x axis, the direction of the analogous electric field; see Fig. 5.5 for simulated intensity distributions. To quantify localisation along the two axes, the inverse participation ratio (IPR) was calculated. The IPR is a

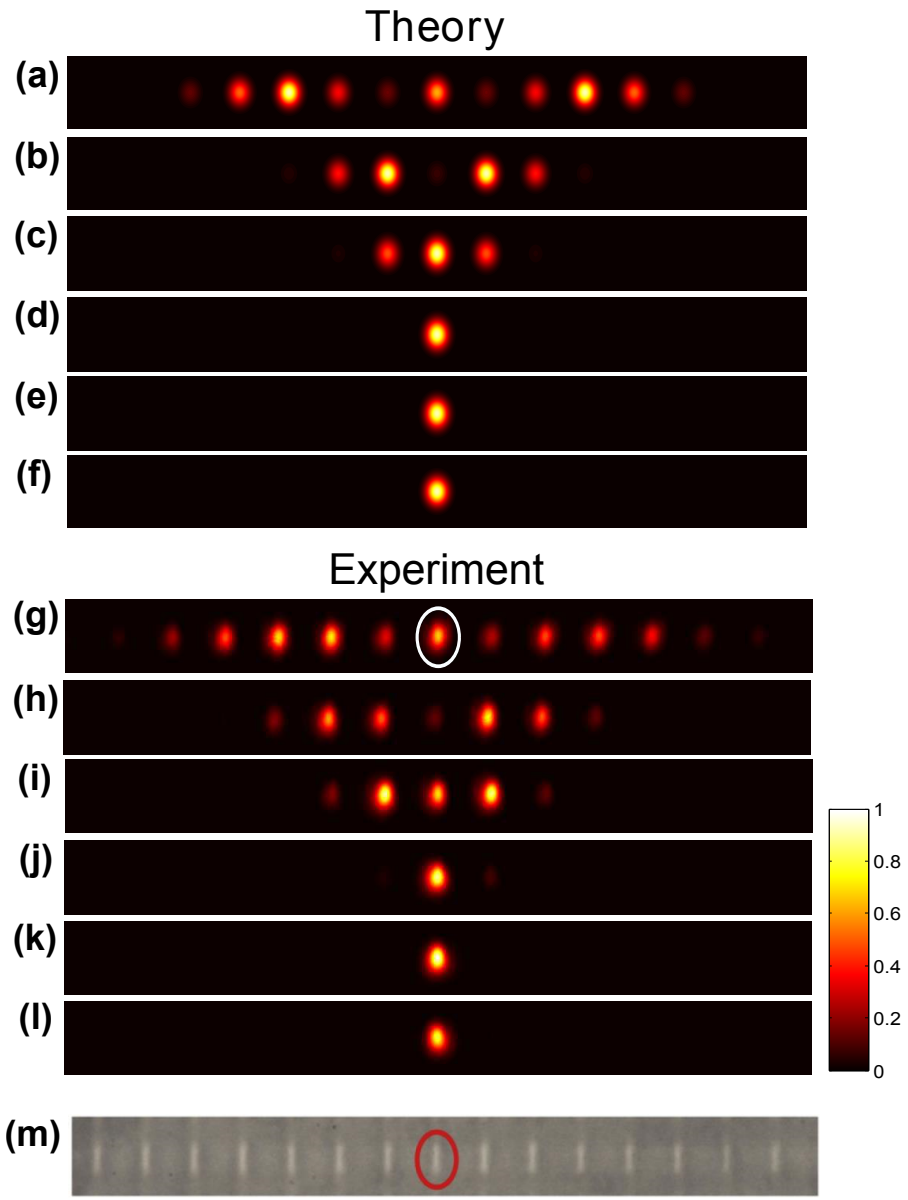

Fig. 5.3: Theoretically predicted (a-f) and experimentally measured (g-l) intensity distributions at the output of a 30-mm-long circularly curved one-dimensional photonic lattices with radii of curvature, (a, g) $R = \infty$ (i.e. straight lattice), (b, h) $R = 1.5$ m, (c, i) $R = 1.2$ m, (d, j) $R = 0.5$ m, (e, k) $R = 0.3$ m and (f, l) $R = 0.2$ m. Here $\kappa = 0.072$ mm^{-1}, $\kappa_N = 0$ and $a = 16$ μm. (m) White-light transmission micrograph of the input facet of a curved one-dimensional photonic lattice with 15 waveguides. Light was launched into the central waveguide at the input of each lattices.

measure of localisation and is defined as the average of the absolute value of the fourth power of the wavefunction. For our purposes, the IPR for the x axis was obtained by summing all the intensity values in each column to obtain a vector of values along the x axis. The IPR was then calculated using this vector. The IPR along the y axis was calculated using the same procedure, but by summing the rows rather than columns. For

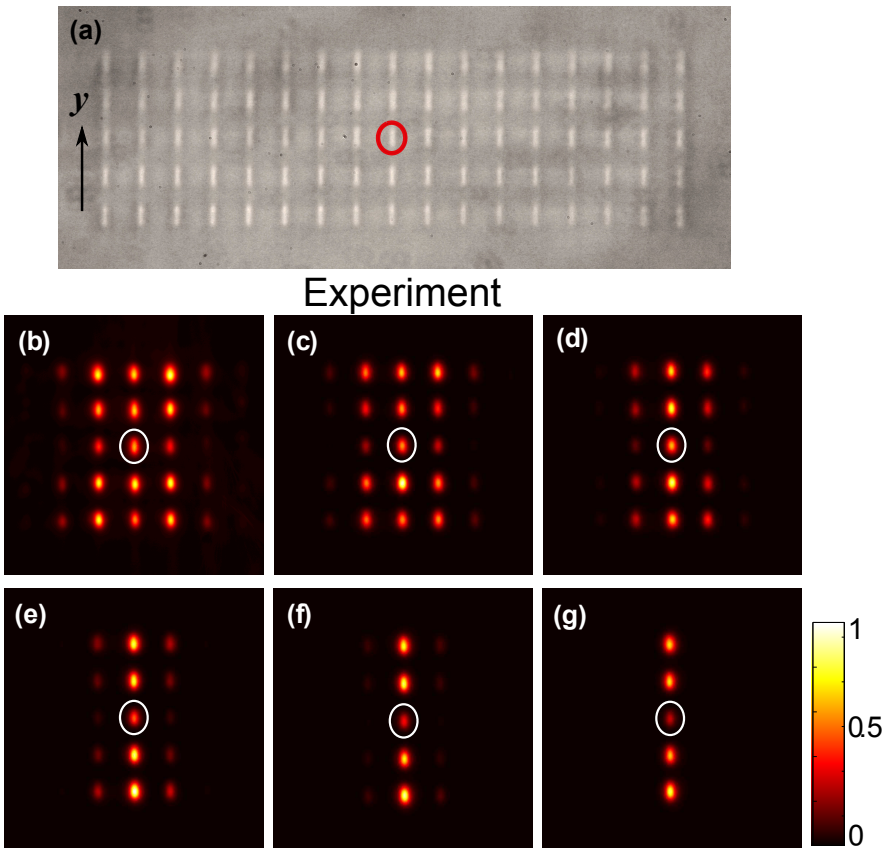

Fig. 5.4: (a) White-light transmission micrograph of the input facet of a curved photonic square lattice with 85 waveguides. (b-g) Experimentally measured intensity distributions at the output of 10-mm-long circularly curved square lattices with radii of curvature (b) $R=\infty$ (i.e. straight lattice), (c) $R=1$ m, (d) $R=0.7$ m, (e) $R=0.5$ m, (f) $R=0.4$ m and (g) $R=0.3$ m. Here $\kappa_x=0.085$ mm^{-1}, $\kappa_y=0.095$ mm^{-1}, $\kappa_N=0.019$ mm^{-1}, $a=15$ μm. For all measurement light was launched into the circled waveguide.

a localised state IPR is unity. As can be seen from Fig. 5.6, there is no effect of the electric field along y axis, as would be expected, but complete localisation (IPR $=1$) is observed along x axis once the electric field analogue exceeds a threshold value.

The localisation phenomenon can also be explained using the theory of waveguide optics. It can be shown [19] using conformal transformation, that a one-dimensional array of curved waveguides with periodic transverse refractive index profile is equivalent to an array of straight waveguides with a new refractive index profile; see also Section 2.5. In the limit $a/R \ll 1$, the new refractive index profile is the superposition of the original periodic index profile and a linear ramp of refractive index, and the radius of curvature controls this ramp. In other words, the mode supported by each waveguide in the curved array has a different propagation constant (β). As R decreases, the difference in β increases, resulting in the partial transfer of light into the nearest waveguides via

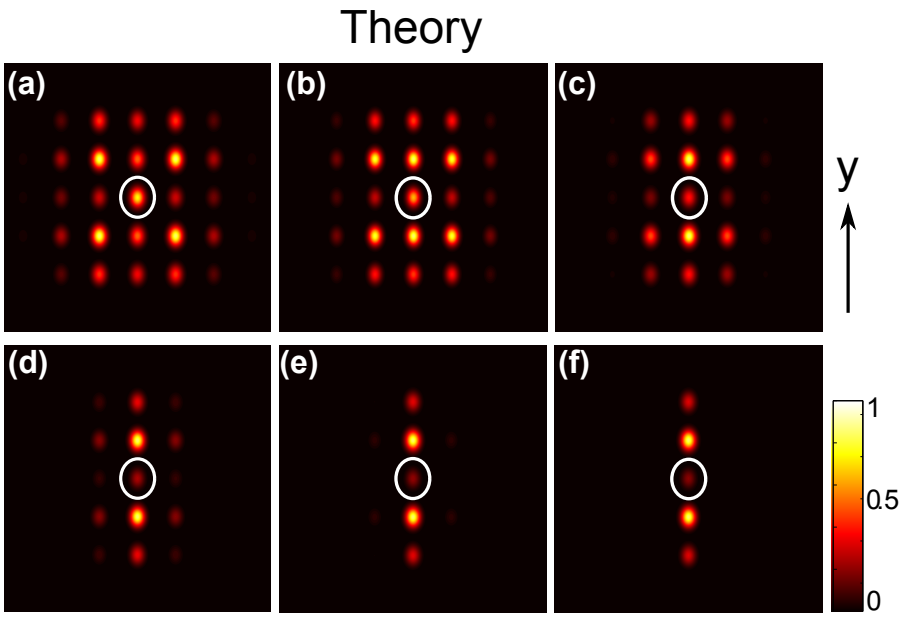

Fig. 5.5: Theoretically predicted intensity distributions at the output of a 10-mm-long circularly curved square lattices with radii of curvature (a) $R = \infty$ (i.e. straight lattice), (b) $R = 1$ m, (c) $R = 0.7$ m, (d) $R = 0.5$ m, (e) $R = 0.4$ m and (f) $R = 0.3$ m. Here $\kappa_x = 0.085$ mm^{-1}, $\kappa_y = 0.095$ mm^{-1}, $\kappa_N = 0.019$ mm^{-1} and $a = 15$ μm.

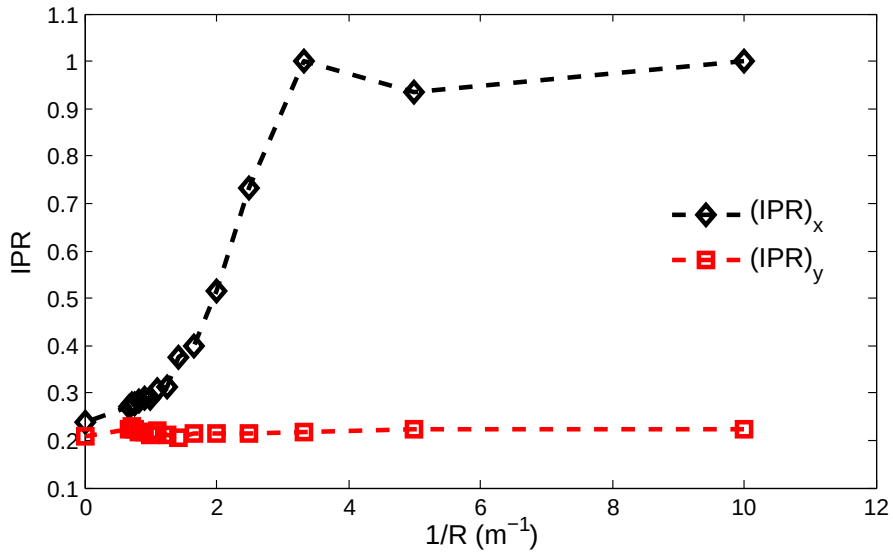

Fig. 5.6: Inverse participation ratio (IPR) is a measure of localisation and is defined as the average of the absolute value of fourth power wave function. The IPRs along the x and y directions, (IPR)$_x$ and (IPR)$_y$ respectively, have been plotted as a function of the inverse of curvature radius R which is a measure of the strength of the static electric field. There is no effect of the electric field along y direction. Complete localisation (IPR $= 1$) is observed along x direction as the electric field exceeds a threshold value.

evanescent coupling. After a threshold value of R, there is no significant coupling between the nearest waveguides resulting a complete spatial localisation.

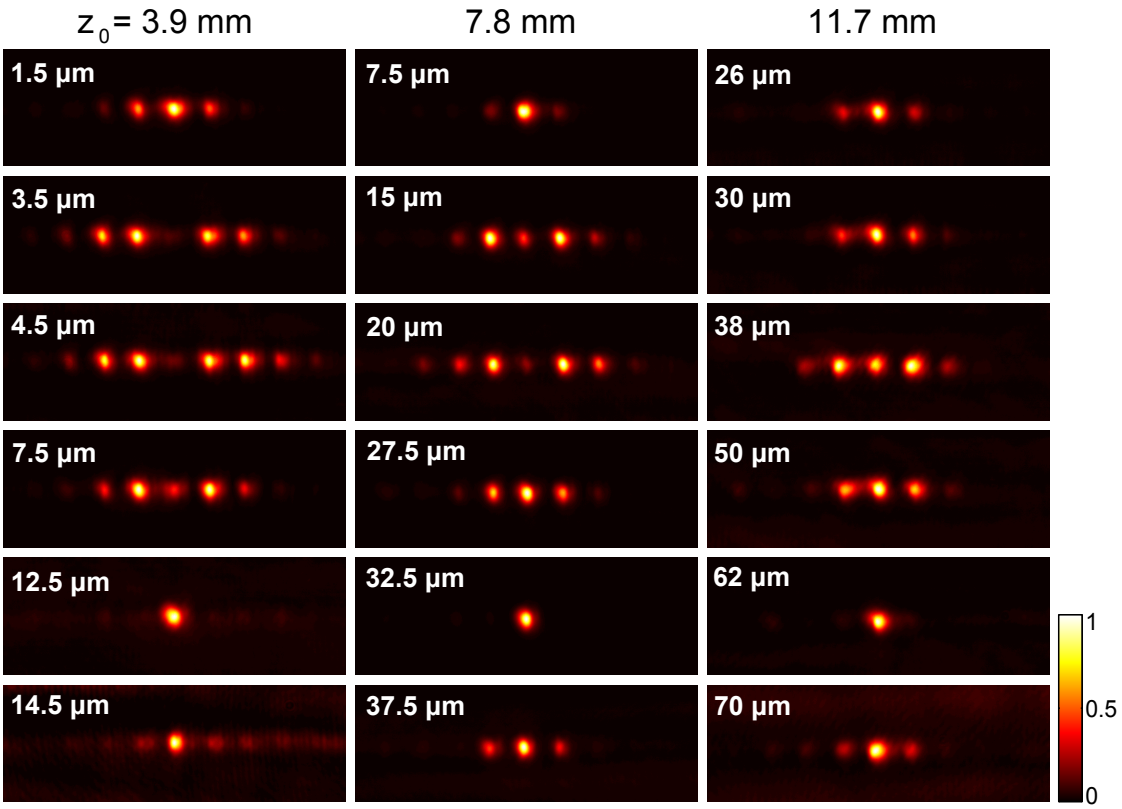

Fig. 5.7: Intensity distribution (normalised) at the output of circularly curved lattices with sinusoidal modulation. Spatial periods of oscillation are 3.9 mm (1-st column), 7.8 mm (2-nd column) and 11.7 mm (3-rd column). For each period the amplitude of oscillation, A, was varied as shown. See also Fig. 5.8. Light was launched into the the central waveguide for all measurements.

5.6 Photon-assisted tunnelling

In the presence of a static, as well as, a sinusoidal field with amplitude A and frequency ω_0, the external force becomes $F = n_0/R + n_0\omega^2 A\sin(\omega_0 z)$. This sinusoidal modulation is analogous to the interaction of the localised W-S state with photons. A strongly localised W-S state can interact with ν photons under the following resonance condition:

$$\omega_0 \nu = n_0 a/R\lambda \tag{5.9}$$

As shown in Ref. [97], the effective tunnelling, in this case, is given by:

$$\left|\frac{\kappa_{\text{eff}}}{\kappa}\right| = \left|\mathcal{J}_\nu\left(\frac{K}{\omega_0}\right)\right|, \tag{5.10}$$

where $\mathcal{J}_\nu$ is the Bessel function of order ν; see also Fig. 5.8.

To observe photon-assisted tunnelling, three sets of lattices (30-mm long) were fabricated with sinusoidal modulation. For sets 1, 2 and 3, the periods ($z_0 = 2\pi/\omega_0$) were

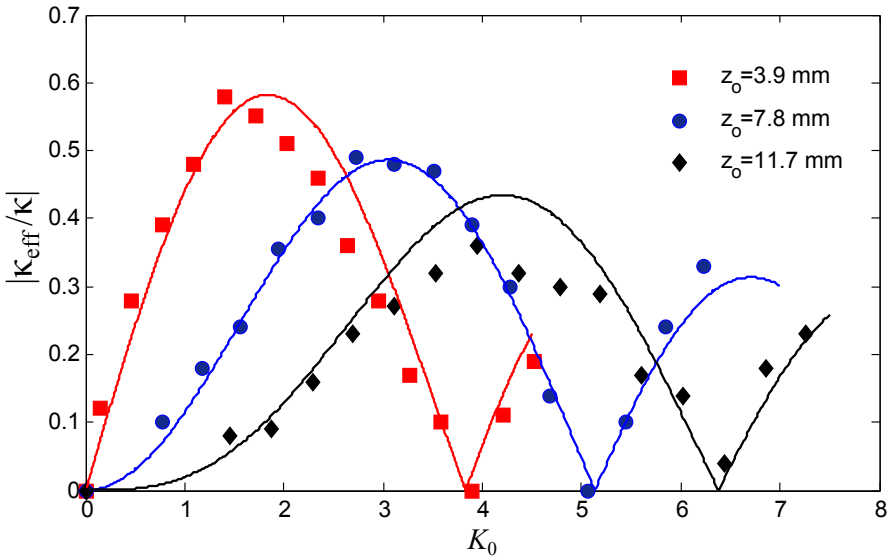

Fig. 5.8: Graphical representation of Fig. 5.7. Variation of the absolute value of the normalised effective coupling with $K_0 (= K/\omega_0)$. The solid lines are the absolute values of Bessel functions ($|J_1|, |J_2|$ and $|J_3|$, respectively) which were predicted theoretically from Eq. (5.10).

set to 3.9 mm, 7.8 mm and 11.7 mm respectively, corresponding to $\nu = 1, 2$ and 3 in Eq. 5.9. For all sets, the radius of curvature and inter-site separation were set to $R = 120$ mm and $a = 16$ μm respectively. For each set, 15 lattices were fabricated, and the amplitude of oscillation, A, was varied; 0.5 μm $\leq A \leq 14.5$ μm (for set 1), 5.0 μm $\leq A \leq 40.0$ μm (for set 2) and 14 μm $\leq A \leq 70$ μm (for set 3). The measured output intensity distributions are shown in Fig. 5.7. The effective coupling of a modulated lattice, for a given value of A, z_0 and R, was evaluated by simulating a 30-mm-long straight photonic lattice, and varying the coupling strength to optimally fit the observed output intensity distributions. The absolute value of the normalised effective coupling strength ($|\kappa_{\text{eff}}/\kappa|$) is plotted graphically as a function of $K_0 = K/\omega_0$ in Fig. 5.8, where it can be seen that ($|\kappa_{\text{eff}}/\kappa|$) has a characteristic (Bessel-function) dependency on K_0, as predicted by Eq. (5.10). This is clear evidence that the tunnelling has been partially restored through an analogue of photon-assisted tunnelling. As a final note, it should be stressed that simulations performed using the experimentally evaluated parameters indicate that significant tunnelling is absent when z_0 was not an integer multiple of 3.9 mm.

5.7 Chapter summary

In this chapter, we have demonstrated that an appropriately designed array of evanescently coupled curved optical waveguides can be used to observe a W-S state that is fully localised on a single lattice site. From the perspective of solid state physics, the localisation is due to an analogue of a strong external static electric field that breaks the degeneracy of the Bloch states and results in a W-S ladder. Remarkably, we also demonstrate that tunnelling in such photonic lattices can be restored by applying an analogue of a sinusoidal electric field and that the strength of this tunnelling obeys a characteristic dependency on the frequency and amplitude of the ac modulation which is directly in agreement with the existing theory of photon-assisted tunnelling.

This page is intentionally left blank.

Chapter 6

One-dimensional two-particle Hubbard model

6.1 Introduction

The physics of tightly bound non-interacting electrons in a crystalline solid at low temperature can be described by the tight binding model. In the tight binding Hamiltonian, only the kinetic energy of an electron is considered. However, in various situations, the particle interaction (e.g the Coulomb repulsion) becomes important giving rise to various intriguing phenomena. In fact, elucidating the physics of interacting electrons in crystalline solids constitutes one of the most challenging problems in modern physics, with direct implications for our understanding of quantum magnetism and superconductivity. In 1963 John Hubbard proposed a model, the Hubbard model [98], by adding an interaction term in the tight binding Hamiltonian, that can be used to examine these problems. However, it should be noted that challenging issues can arise, especially in the intermediate to strong coupling regimes where perturbation theory fails. The artificial crystal of cold atoms loaded into optical lattices [1–3] is an important and powerful experimental platform to simulate Hubbard Hamiltonian and study many-body physics in the laboratory. These experiments include the observation of the superfluid-Mott insulator phase transition [99, 100], the realisation of one-dimensional quantum liquids [101, 102], observation of second-order atom tunnelling [103], the investigation of disordered systems [104] and the demonstration of repulsively bound states using both bosonic [105] and fermionic [106] particles. These experiments triggered an intense activity exploring the physics of interacting particles in optical lattices, including the two-body [107–112] and three-body [113, 114] problems. It is of great interest to identify these exotic few-body properties in the absence of many-body environment which is difficult using solid-state systems and challenging to probe using traditional cold-atom experiments. Recently, few-body physics was explored with cold atoms in the absence of an optical lattice [115–118]; using this approach, a one-dimensional Heisenberg spin

chain was realised using few atoms [119].

In this chapter, we focus on the two-particle photonic Hubbard model in one-dimension, that was investigated in a number of recent works [120–125], and demonstrate a series of phenomena, such as suppression of 1-st order tunnelling, pair tunnelling and coherent destruction of tunnelling (CDT), for the paired particles; see also [126].

6.2 Two-particle Hubbard Model

We consider two identical particles (e.g. bosons) in a one-dimensional tight binding lattice with nearest-neighbour hopping. Also consider, for simplicity, that these particles interact (either attract or repel) with each other only when they are in the same potential well. In other words, there is only on-site interaction. This type of situation is described by the two-particle Hubbard model. In this section, we will show that the physics of two interacting quantum particles moving in a one-dimensional lattice can be simulated using a non-interacting system, such as photonic crystals operating in the linear optical regime [120–125]. This approach is based on a mapping, which we now briefly summarise; see also [127, 128]. Let us consider the standard Hubbard model (with $\hbar=1$) in one dimension,

$$\hat{H}=-J\sum_{s}\left(\hat{a}_{s}^{\dagger}\hat{a}_{s+1}+\hat{a}_{s+1}^{\dagger}\hat{a}_{s}\right)+\frac{U_0}{2}\hat{n}_s(\hat{n}_s-1), \tag{6.1}$$

where $\hat{a}_s^{\dagger}$ ($\hat{a}_s$) is the creation (annihilation) operator for a particle at the s-th lattice site, $\hat{n}_s=\hat{a}_s^{\dagger}\hat{a}_s$ is the number operator, J is the nearest neighbour hopping amplitude and U_0 is the on-site interaction energy (note that $U_0>0$ for repulsive interactions). Considering only two identical particles in the system, one expands the two-body wave function in the Fock basis as

$$|\psi(t)\rangle = \frac{1}{\sqrt{2}}\sum_{l,m} C_{l,m}(t)\,|l,m\rangle\,, \tag{6.2}$$

where $C_{l,m}$ is the probability amplitude for finding one particle at site l and the other one at site m. Using Eq. (6.1) and (6.2), the time evolution of $C_{l,m}(t)$ is obtained from the time dependent Schrödinger equation: $i\partial_t\,|\psi\rangle=\hat{H}\,|\psi\rangle$,

$$i\frac{dC_{l,m}(t)}{dt} = -J\big(C_{l+1,m}+C_{l-1,m}+C_{l,m+1}+C_{l,m-1}\big)+U_0C_{l,m}\delta_{l,m}. \tag{6.3}$$

It should be noted that Eq. (6.3) can be formally mapped into a Schrödinger equation that describes the dynamics of a *single particle* in a two-dimensional lattice, with sites

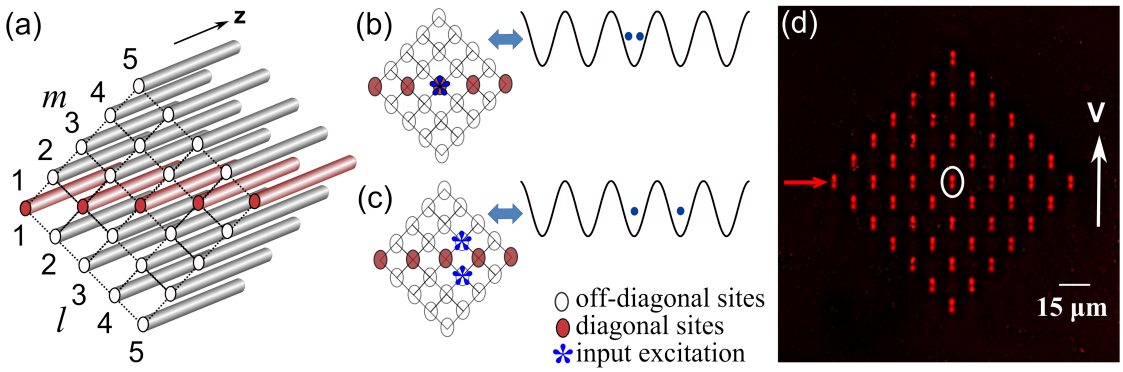

Fig. 6.1: (a) Schematic diagram of a photonic square lattice where the diagonal sites $l = m$ (shown in red) have a shifted propagation constant, $\Delta\beta$ ($\equiv U_0$), compared to the off-diagonal waveguides. The excitation of a diagonal waveguide at the input is the optical analogue of two interacting particles at the same potential well of a one-dimensional lattice at time, $t = 0$ (b). The excitation of the two off-diagonal waveguides corresponds to the particles located at different lattice sites at $t = 0$ (c). (d) White-light transmission micrograph of the facet of a laser-fabricated photonic square lattice. The lattice axes were rotated by 45° with respect to the vertical direction (V) to achieve $\kappa_x \approx \kappa_y = \kappa$. The circled waveguide was excited at the input for all measurements. The red arrow indicates the main diagonal ($l = m$).

located at position $\boldsymbol{r} = a_x l\hat{x} + a_y m\hat{y}$, where $a_{x,y}$ denote the lattice constants, and (l, m) are integers labelling the lattice sites in the 2D plane. In this picture, J denotes the hopping amplitude along both spatial directions, and U_0 corresponds to an on-site potential, which only affects the sites located along the diagonal $l = m$. As a result, any non-interacting two-dimensional system described by Eq. (6.3) can be exploited to capture the physics of the two-body Hubbard problem [Eq. (6.1)].

In this chapter, we explore the above-mentioned mapping by considering a photonic square lattice ($a_x, a_y = a$), a square array of coupled optical waveguides [Fig. 6.1 (a)]. Recently, such photonic systems have been developed to study single-particle effects such as CDT in a double well [84, 85], Bloch oscillations [88], dynamic localisation [22, 129], Landau-Zener tunnelling [92], Anderson localisation [58], chiral edge modes [130], and the localised states associated with flat-band lattices (see Chapter 4). Specific effects related to interacting systems have also been studied based on photonic lattices, see Refs. [120–125], suggesting an interesting alternative to cold-atom experiments [103, 112].

6.3 Photonic implementation

We consider a straight photonic square lattice where the waveguides located along the main diagonal ($l=m$) have a shifted propagation constant ($\Delta\beta=\beta_{\text{off-diagonal}}-\beta_{\text{diagonal}}$) as compared to all other (off-diagonal) waveguides, see Fig. 6.1 (a). (Note that the weakly guiding approximation and paraxial approximation are valid for our engineered photonic lattices; see Section 2.2.) In the nearest-neighbour tight binding approximation, the propagation of light across this photonic lattice is governed by the following coupled mode equation [121, 122]

$$i\frac{dE_{l,m}(z)}{dz}=-\kappa\big(E_{l+1,m}+E_{l-1,m}+E_{l,m+1}+E_{l,m-1}\big)+\Delta\beta E_{l,m}\delta_{l,m}, \tag{6.4}$$

where $E_{l,m}$ is the envelope of the electric field at the waveguide (l,m), z is the propagation direction, and κ is the nearest neighbour coupling constant. The analogy with the Hubbard problem in Eq. (6.3) is obtained by identifying (up to physical units) $t\leftrightarrow z$, $J\leftrightarrow\kappa$ and $U_0\leftrightarrow\Delta\beta$. In the experiment, we only excite a diagonal site and hence, simulate the dynamics of two interacting particles (either bosons or fermions with opposite spins [127]) initially placed in the same potential well. One can, however, simulate the dynamics of two bosons or two spinless fermions placed in two different wells, by exciting two off-diagonal waveguides with symmetric ($E_{l,m}=E_{m,l}$) or anti-symmetric ($E_{l,m}=-E_{m,l}$) states respectively. Note that for two fermions with opposite spin, the particles are distinguishable and hence, the two-body wave function will be of the form: $|\psi(t)\rangle=\sum_{l,m}C_{l,m}(t)\,|l,m\rangle$.

6.4 Fabrication and characterisations

In this section, we briefly discuss the fabrication parameters, measurement of coupling constant (κ) and analogous interaction (or shift in propagation constant, $\Delta\beta$). We then present the measured values of waveguide losses (propagation loss+bend loss). The coupled optical waveguide arrays were fabricated using the ultrafast laser inscription technique and the waveguide refractive index profile was controlled using the slit beam shaping method; see Section 3.2.3. The white-light-transmission micrograph of the facet of a finite square lattice is shown in Fig. 6.1 (d). The lattice contains 49 waveguides, each of which supports only a fundamental mode at 740 nm wavelength. The lattice constant is 16.35 μm. The lattice axes were rotated by 45° with respect to the

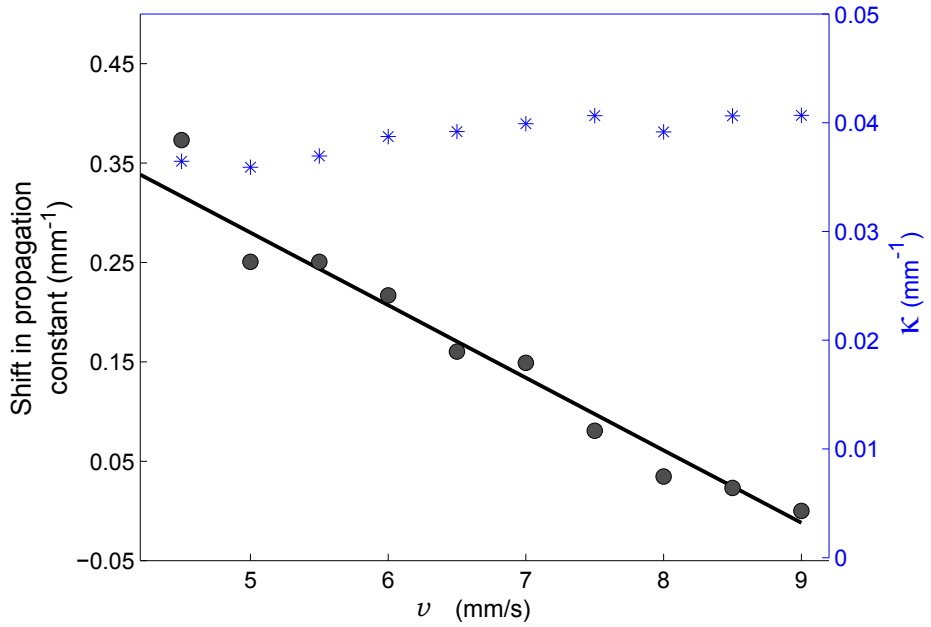

Fig. 6.2: Variation of shift in propagation constant $[\beta(v) - \beta(v = 9 \text{ mm/s})]$ as a function of translation speed (v). The black circles are the measured values and the solid line is the linear fit. (Blue) The variation of hopping amplitude (κ) with translation speed can be ignored as it is comparable to the random variation of κ (i.e. the off-diagonal disorder).

vertical direction (V) to achieve $\kappa_x \approx \kappa_y$, where κ_x and κ_y are the coupling strengths along the two axes of the lattice.

The parameters that describe a photonic lattice are the coupling constants between the lattice sites and the propagation constant of each waveguide. To estimate the variation of the nearest neighbour coupling constant (κ) with translation speed, ten symmetric evanescently coupled two-waveguide couplers (both waveguides with identical fabrication parameters) were fabricated with translation speeds 9 to 4.5 mm/s in steps of 0.5 mm/s. As can be seen from Fig. 6.2, the variation of κ with translation speed can be ignored as it is comparable to the random variation of κ (i.e. the off-diagonal disorder). To measure next-nearest neighbour coupling (κ_n), two-waveguide evanescent couplers were fabricated with waveguide-to-waveguide separation $D = \sqrt{2}a$; a is the lattice constant of the square lattices and it was found that $\kappa_n \approx 0$ for the maximum observable propagation distance. To estimate the variation of the waveguide refractive index (n_{wg}) with translation speed, we fabricated ten one dimensional diffraction gratings with 15 μm grating period, using translation speeds of 9 to 4.5 mm/s. The physical

depth of each grating was measured (using an optical microscope) to be $d = 5 \pm 0.5$ μm, and it is reasonable to assume that for our inscription parameters, the variation of writing speed only changes the magnitude of the refractive index contrast, not its spatial extent. By measuring the absolute diffraction efficiency of these gratings at the first order (η_1), and assuming that the diffraction gratings are sinusoidal phase gratings, n_{wg} is calculated from [51], as:

$$\eta_1 = \mathcal{J}_1^2\Big(\frac{2\pi(n_{wg} - n_0)}{\lambda} d\Big), \tag{6.5}$$

where n_0 is the refractive index of the substrate, and $\mathcal{J}$ is the Bessel function of the first kind. The quantity of our interest is the shift in propagation constant (i.e. $\frac{2\pi}{\lambda}\Delta n_{\text{eff}}$) as function of the translation speed of fabrication. Assuming that the difference in the effective indices of the modes (Δn_{eff}) is very close to the difference in waveguide refractive indices (Δn_{wg}) for two waveguides fabricated with two different translation speeds, we plot the shift in propagation constant [$\beta(v) - \beta(v = 9$ mm/s)] as a function of translation speed; see Fig. 6.2. It was found that within the range of fabrication parameters, the shift in propagation constant varies almost linearly with translation speed. The black circles in Fig. 6.2 are the measured values and the solid line is the linear fit.

To measure the variation of propagation loss with translation speed, ten isolated straight waveguides (translation speeds 9 to 4.5 mm/s in steps of 0.5 mm/s) were fabricated in a 15-mm-long substrate. We estimated propagation loss by subtracting the coupling losses from the measured insertion loss for each waveguide. The propagation loss of the waveguide fabricated with 9 mm/s was found to be 0.92 dB/cm. The variation of propagation loss with translation speed was insignificant, with a maximum fluctuation of ≈ 0.04 dB/cm. To estimate bend loss, two sets of sinusoidally modulated waveguides were fabricated with translation speeds of 9 and 6.5 mm/s. For each set, 15 waveguides were fabricated with 1 μm $\leq A \leq 15$ μm in steps of 1 μm. Now the quantity of interest is the difference in total loss (propagation loss+ bend loss) for two waveguides fabricated with equal amplitude of modulation and two different translation speeds, which was measured to be < 0.15 dB for 15-mm-long waveguides. Therefore the site-dependent loss can be ignored.

6.5 Time evolution of two interacting particles

In order to observe the effect of the on-site "interaction", we fabricated ten straight ($A = 0$) square lattices of 15 mm propagation length (z_{max}) with ten different values for

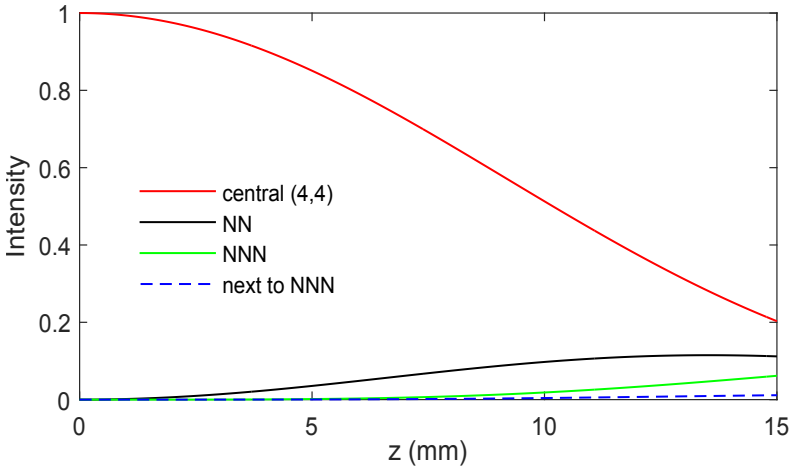

Fig. 6.3: Numerically calculated evolution of light intensity along the propagation direction, z, for a 7×7 photonic square lattice. Here $\Delta\beta=0$, $\kappa=0.04$ mm^{-1}. The red curve is for the central waveguide (4, 4) that was excited at the input $(z=0)$. The black, green and the dotted blue curves indicate intensities at the nearest neighbour (NN), next-nearest neighbour (NNN) and next to next-nearest neighbour waveguides. Fig. 6.4 (a) shows the measured output intensity distribution at $z=15$ mm.

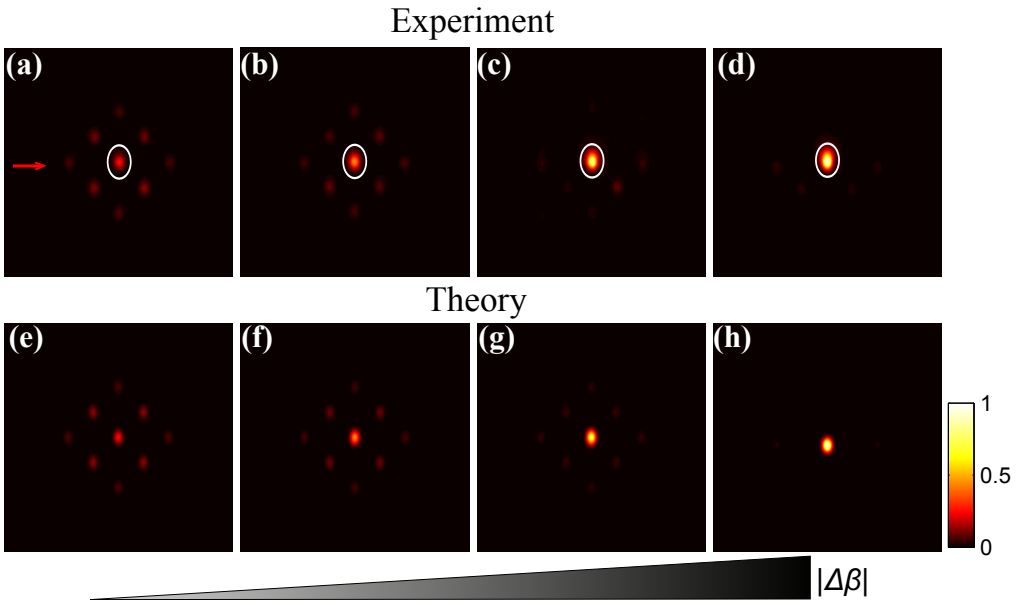

Fig. 6.4: Experimentally observed output intensity distributions when light was launched into the $l, m = 4, 4$ site (circled waveguide) of the 15-mm-long straight photonic square lattices ($A = 0$). Here the coupling constant is $\kappa = 0.04$ mm^{-1}. The analogous interaction $\Delta\beta$ is (a) 0.0, (b) -0.12 mm^{-1}, (c) -0.21 mm^{-1} and (d) -0.32 mm^{-1}. The corresponding simulated intensity distributions are shown in (e)-(h). Each image is normalized such that the total output power is 1. See also Fig. 6.3. The red arrow indicates the main diagonal ($l=m$).

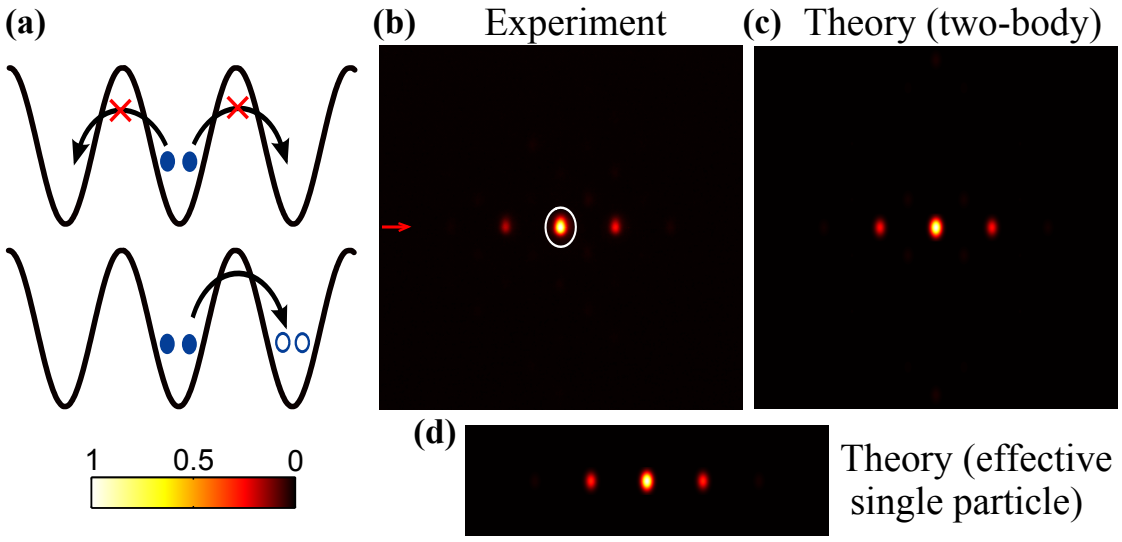

Fig. 6.5: (a) Schematic diagram of pair hopping in the "strong-interaction" regime [$\Delta\beta \gg \kappa$, equivalent to $U_0 \gg J$]. (b) Experimental observation of pair hopping in the 70-mm-long straight photonic square lattices for $\kappa = 0.027$ mm^{-1}, $\Delta\beta = -0.21$ mm^{-1} ($v_d = 6$ mm/s). The corresponding two-body simulation and the effective single-particle simulation with pair coupling $\kappa_2 = -2\kappa^2/\Delta\beta$, are shown in (c) and (d), respectively. Each image is normalised such that the total output power is 1. The white circle indicates the waveguide that was excited at the input.

the shifted propagation constant $\Delta\beta$. As mentioned in the previous section, the precise tuning of $\Delta\beta$ was realised, without affecting κ and site dependent losses, by changing the translation speed, v of fabrication; within the range of our fabrication parameters, the shift in propagation constant varies almost linearly as the translation speed. The nearest neighbour coupling constant is $\kappa = 0.04$ mm^{-1} and the next-nearest neighbour coupling was insignificant for the maximum observable propagation distance (for all lattices). Note that the values of κ and z_{max} were chosen such that the lattice sites at the edges are never excited; see Fig. 6.3. The off-diagonal waveguides have, in all cases, the same propagation constant, since they were fabricated with the same translation speed ($v_{\text{od}} = 9$ mm/s). The diagonal waveguides in each lattice were fabricated with a different translation speed, $v_d = v_{\text{od}} - \Delta v$, with $\Delta v = 0$ to 4.5 mm/s in steps of 0.5 mm/s, resulting in a different propagation constant ($\Delta\beta$) along the diagonal; this gives rise to the analogous on-site "interaction" term [Eq. (6.4)]. Fig. 6.4 (a) shows the observed output intensity distribution for $\Delta v = 0$ (or $\Delta\beta = 0$) and for the input condition: $E_{4,4}(0) = 1$. Applying the same input condition, we observed that the output intensity distribution becomes increasingly localised as Δv was increased [Fig. 6.4 (b)-(d)]; this is in excellent

agreement with the theoretical intensity distributions [see Fig. 6.4 (e)-(h)], which were obtained by solving the coupled-mode equations (Eq. 6.4). Theoretically, these results can be understood in terms of the effective mass of the two-body bound state associated with the Hubbard Hamiltonian Eq. (6.1), i.e. $M^* \approx -\hbar^2 U_0/(4J^2a^2)$, whose absolute value increases as a function of the interaction strength in the strongly-interacting regime [108].

In the strongly-interacting regime of the Hubbard model, standard tunnelling for individual particles is suppressed but the particles can hop as a pair; see Fig. 6.5 (a). Such a pair tunnelling cannot be identified in Fig. 6.4, due to the very weak pair tunnelling parameter $\kappa_2 \ll \kappa$ and the small propagation length (15 mm) of the lattices. Hence, in order to reveal pair tunnelling, a longer photonic lattice (70-mm-long) was fabricated; note that a larger lattice constant (18 μm) was also chosen in order to inhibit next-nearest neighbour hopping in this longer lattice. Here, the other lattice parameters are given by $\kappa = 0.027$ mm^{-1} and $\Delta\beta = -0.21$ mm^{-1}. When the $(4, 4)$ waveguide was excited at the input of this lattice, we observe significant amount of light in the diagonal waveguides [Fig. 6.5 (b)]. This is a direct demonstration of pair tunnelling, and hence, the formation of a bound state in the strongly-interacting regime. We see good agreement between experimental results, the full two-body simulation [i.e. the solution of Eq. (6.4)] and an effective single-particle simulation; the latter corresponds to the dynamics of a paired state hopping in a one-dimensional lattice, with the modified (pair tunnelling) constant $\kappa_2 = -2\kappa^2/\Delta\beta$ [107, 108].

6.6 Theory of coherent destruction of tunnelling

In this section, we will briefly summarise the theory of coherent destruction of tunnelling for two interacting particles; see also [123, 127, 128]. Let us consider the dynamics of two interacting particles in a one-dimensional tight binding lattice driven by a sinusoidal force of high frequency. We add a time dependent term (driving) in Eq.(6.1) and write the Hamiltonian as

$$\hat{H} = -J \sum_s \left(\hat{a}_s^\dagger \hat{a}_{s+1} + \hat{a}_{s+1}^\dagger \hat{a}_s\right) + \frac{U_0}{2} \hat{n}_s(\hat{n}_s - 1) + K \sin(\Omega t) s \hat{n}_s, \tag{6.6}$$

where K and Ω are the amplitude and frequency of the driving. Now expanding the two-body wavefunction in the Fock basis [Eq. (6.2)], the time evolution of $C_{l,m}(t)$ is

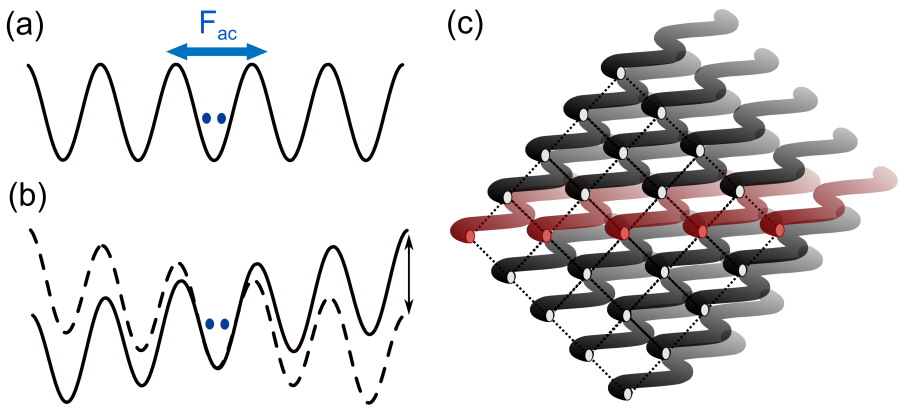

Fig. 6.6: (a) Schematic diagram of two interacting particles in a one-dimensional lattice driven by a sinusoidal force (F_{ac}). (b) The sinusoidal force changes the slope of the potential sinusoidally with time. (c) A modulated photonic square lattices which mimics the dynamics of (a, b).

determined by solving the equation

$$i\frac{d}{dt}C_{l,m}(t) = -J\big(C_{l+1,m} + C_{l-1,m} + C_{l,m+1} + C_{l,m-1}\big) + \big[U_0\delta_{l,m} + K\sin(\Omega t)(l+m)\big]C_{l,m}. \tag{6.7}$$

In our photonic platform, the sinusoidal driving is realised by periodically modulating the waveguides along the main diagonal; see Fig. 6.6 (c). The coupled mode equation for a sinusoidally driven photonic lattice with a shift in propagation constant in the diagonal is given by

$$i\frac{d}{dz}E_{l,m}(z) = -\kappa\big(E_{l+1,m} + E_{l-1,m} + E_{l,m+1} + E_{l,m-1}\big) + \left[\Delta\beta\delta_{l,m} + \frac{An_0\omega^2 a}{\sqrt{2}\lambda}\sin(\omega z)(l+m)\right]E_{l,m}, \tag{6.8}$$

where n_0 is the refractive index of the medium, and A [resp. ω] is the amplitude [resp. spatial frequency] of the sinusoidal modulation. In this photonic setup, the analogy of driving in Eq. (6.7) is obtained by the simple identification $K \leftrightarrow An_0\omega^2 a/(\sqrt{2}\lambda)$.

The dynamics of the two interacting particles in the presence of a sinusoidal driving force is determined by κ, $\Delta\beta$, ω and K [Eq. (6.8)], and the transport along the array can be suppressed (CDT) under the following conditions. In the high frequency regime ($\omega \gg \Delta\beta$), the external driving renormalises the hopping amplitude, $\kappa_{\text{eff}} = \kappa|\mathcal{J}_0(K/\omega)|$, as for the non-interacting case and causes approximate CDT when the zero-th order Bessel function ($\mathcal{J}_0$) is zero. For $\omega \ll \Delta\beta$ (low frequency regime) CDT cannot be

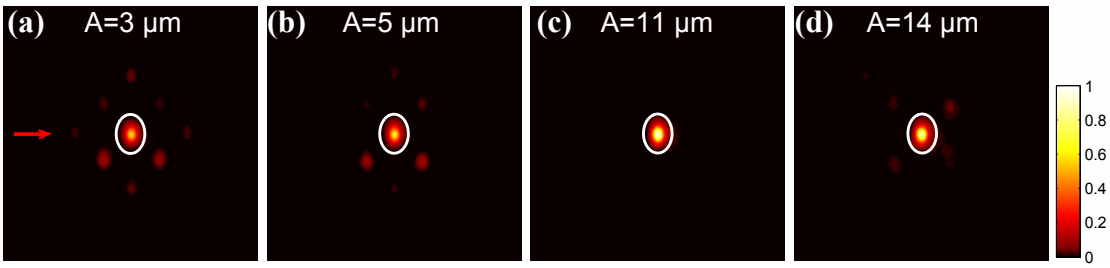

Fig. 6.7: (a)-(d) The intensity distributions at the output of modulated square lattices (15-mm-long) for the input condition: $E_{4,4}(0)=1$. The on-site interaction ($\Delta\beta$) and the driving frequency ($\omega \gg \Delta\beta$) were fixed and The amplitude of modulation (A) was varied from 1 to 15 μm in steps of 1 μm. For each image the value of A is indicated. Each image is normalised such that the total output power is 1. The amplitude of modulation (A) is indicated for each image. A different colour-scale was chosen to highlight the low intensities.

observed simultaneously for paired and unpaired particles as the effective force on the paired particle is twice the force acting on an unpaired particle. In this context the role of $K/\Delta\beta$ was elaborated in Ref. [131]; see also [127]. It was shown that the miniband structure breaks down as K approaches $\Delta\beta$. Recently, it was reported in Ref. [123] that CDT can be simultaneously realised for both paired and unpaired particles under appropriate driving if $\omega \sim \Delta\beta$ and $\omega \gg \kappa$, up to the long time scale ($\sim \omega/\kappa^2$).

6.7 Observation of CDT

Here we focus on CDT in the high frequency regime ($\omega \gg \Delta\beta, \kappa$; $\omega = 2\pi/z_0$; $z_0 = 4$ mm). In the experiment, fifteen square lattices (15-mm-long) were fabricated with sinusoidally modulated waveguides [Fig. 6.6 (c)]. The amplitude of modulation (A) was varied from 1 to 15 μm in steps of 1 μm. The on-site interaction $\Delta\beta = -0.18$ mm^{-1} [$v_{od} = 9$ mm/s and $v_d = 6.5$ mm/s.], driving frequency $\omega = 1.57$ mm^{-1} and the hopping amplitude, $\kappa = 0.04$ mm^{-1} in all cases. Fig. 6.7 (a)-(d) show the output intensity distributions when light is launched at the (4, 4) site of each lattice. As A is increased the output intensity distribution is observed to be increasingly localised and becomes almost fully localised near $A = 11$ μm. As A was further increased, the tunnelling is restored. To quantify the localisation, the inverse participation ratio (IPR) was calculated from the measured output intensity distributions. The IPR is a measure of localisation and is defined as the

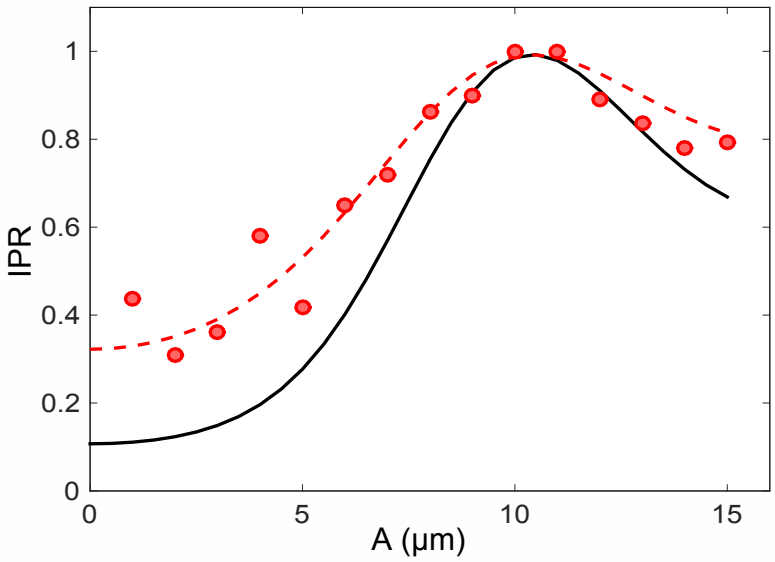

Fig. 6.8: The variation of IPR as a function of A. The red circles show the measured IPR. The dotted red line indicates the theoretically obtained variation of IPR. Here $\Delta\beta = -0.18$ mm^{-1}, $\kappa = 0.04$ mm^{-1}, and $\omega = 1.57$ mm^{-1}. The solid black curve represents the variation of IPR for $\Delta\beta = 0$.

average of the absolute value of the fourth power of the wavefunction:

$$\text{IPR} = \frac{\sum I_{l,m}^2}{\left(\sum I_{l,m}\right)^2}, \tag{6.9}$$

where $I_{l,m}$ is the light intensity at the $(l,\ m)$ waveguide. The measured IPR (at $z = 15$ mm) as a function of A is shown in Fig. 6.8 by the red circles, in good agreement with the theoretical result (dotted red line). To highlight the difference between the observed IPR for two interacting particles and that for two non-interacting particles, the theoretical IPR with no interactions ($\Delta\beta = 0$) is shown by the solid black line for which CDT occurs when $\mathcal{J}_0(K/w) = 0$ (i.e. $A \approx 11$ μm). It should be mentioned that the IPR is not a conserved quantity (when the condition for CDT is not satisfied) along the propagation direction. The variation of IPR as a function of z is shown in Fig. 6.9 for four different values of A.

The observed variation of IPR with the amplitude of modulation can be explained from the Floquet quasienergy spectrum [131, 132]. For the modulated square lattices, the Hamiltonian is a periodic function of z, i.e. $\hat{H}(z) = H(z + z_0)$. In this situation, using Floquet theory, the solution of the Schrödinger equation can be written as $|\Phi(z)\rangle = e^{-i\varepsilon z}|\phi(z)\rangle$ with $|\phi(z)\rangle = |\phi(z + z_0)\rangle$, where $|\phi(z)\rangle$ is a Floquet state and ε is the quasienergy. To obtain the quasienergies we diagonalize the evolution operator defined

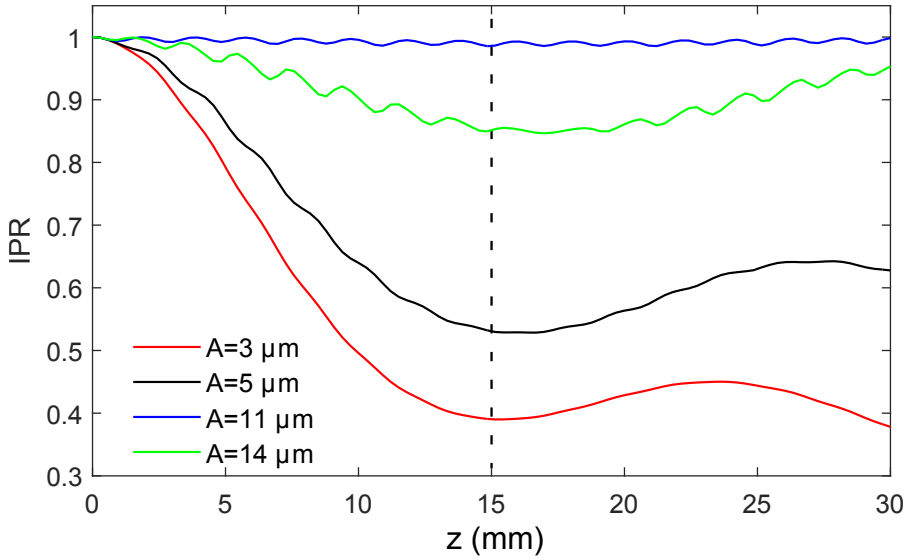

Fig. 6.9: Variation of inverse participation ratio (IPR) as a function of propagation distance, z, for the modulated photonic lattices presented in Fig. 6.7 (a)-(d). The dotted line indicates the z value where the output intensities were experimentally measured; see Fig. 6.7 (a)-(d).

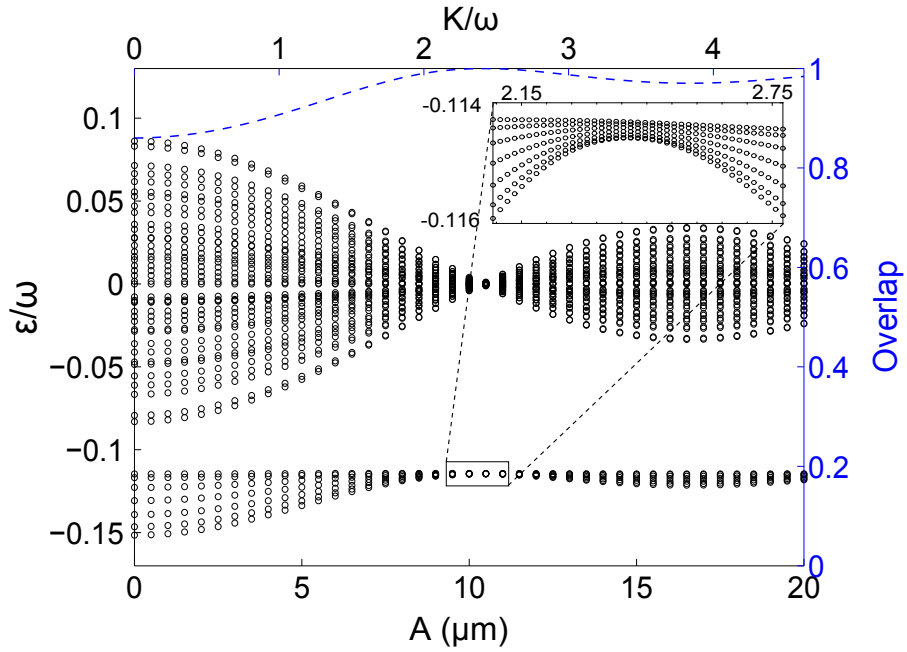

Fig. 6.10: Floquet quasienergies (Black) for a sinusoidally driven one-dimensional lattice with two interacting particles. The wider miniband corresponds to the unpaired state and the narrower miniband is for the paired states. The inset shows the pseudo-collaps of the narrower miniband. The minibands are separated by the Hubbard gap, $\sim \Delta\beta$. The overlap of the input state, $E_{4,4} = 1$ and the eigenstates of the narrower miniband as a function of A is shown by the dotted blue line.

as:

$$U = \mathcal{T} \exp\Big[-i \int_0^{z_0} H(z')dz' \Big], \tag{6.10}$$

where $\mathcal{T}$ indicates the time ordering. The normalised quasienergy (ε/ω) is plotted in Fig. 6.10 as a function of A for fixed values of $\Delta\beta$ and κ. As can be seen in Fig. 6.10, the quasienergies for two interacting particles in a periodically-driven one dimensional lattice form two minibands. The wider miniband corresponds to the states in which the two particles are in separate wells (unpaired state) and the narrower miniband corresponds to the paired states. The minibands are separated by a gap$\sim\Delta\beta$, corresponding to the (anti-) binding energy. Both minibands (pseudo) collapse near $A = 11$ μm which causes (approximate) CDT. The calculation of the overlap of the input state, $E_{4,4} = 1$ and the eigenstates of the narrower miniband as a function of A is shown by the dotted blue line in Fig. 6.10. The overlap is more than 80% irrespective of the value of A. Importantly, since the narrower miniband is less dispersive compared to the Floquet band of two non-interacting particles (not shown in the figure), the localisation (IPR) of the interacting system is stronger than in the case of a non-interacting system (i.e. the dotted red line in Fig. 6.10 lies above the solid black line).

6.8 Chapter summary

We have experimentally implemented the photonic realisation of two interacting particles in a one dimensional tight-binding lattice with only nearest neighbour tunnelling. The suppression of independent tunnelling of individual particles and the evidence of second order pair tunnelling was observed in the strong interaction regime. We then showed the effect of an engineered sinusoidal force on the paired state. Coherent destruction of tunnelling was observed as the amplitude of the force is varied. Our experiment paves the way for simulating few-body physics in low-dimensional lattices with a clean nearest-neighbour-only hopping, for both static and periodically-driven (or Floquet) Hamiltonians. Successful implementation of similar photonic setups will enable us to experimentally simulate other intriguing problems such as *N* particles in a double-well potential [120], the dynamics of the correlated particles in a random potential [133, 134], dissipation-induced correlation [125] and two-body Su-Schrieffer-Heeger model [135].

This page is intentionally left blank.

Chapter 7

Observation of anomalous topological edge modes in a slowly-driven photonic square lattice

7.1 Introduction

The discovery of *quantised Hall effect* [136] and *topological insulators* [137–139] have stimulated the investigation of topologically protected quantum effects in solid-state systems. Topological insulators are a family of materials with insulating bulk and conducting edge or surface states. These edge states are insensitive to defects and they can propagate one-way (chiral) without back-scattering. Although these topologically robust phenomena were originally studied in electronic systems, in recent years various artificial systems, such as cold atoms in optical lattices [140], coupled optical ring resonators [141–143] and photonic lattices [130], have become important experimental tools. In band theory, the Bloch bands are characterised by band index and quasimomentum. However, in topological band theory, a set of topological invariants are necessary for the complete characterisation of the Bloch bands. For a static system, where the Hamiltonian is not a function of time, one such topological invariant is the Chern number, $\mathcal{C}_n$ for the n-th Bloch band. For a finite lattice with edges, $\mathcal{C}_n$ is equal to the difference between the numbers of chiral edge modes entering the band from below and exiting above (static bulk-edge correspondence).

Using Floquet theory, the topological band theory of a static system can be extended to a periodically-driven system. For fast driving, driving frequency $\gg$ hopping amplitude, the topological phase of a system can be predicted by the usual Chern numbers that are used to describe static systems. However, in the limit of slow driving, driving frequency $\sim$ hopping amplitude, topologically protected edge modes can be observed even if the Chern numbers associated with all the bulk bands are zero. In Rudner et. al. [144], these novel type of topological edge modes were referred to "anomalous" edge modes. Here, we focus on the single particle physics in a periodically driven photonic square lattice,

and investigate this novel type of chiral edge mode ("anomalous" or "genuine Floquet" topological edge modes) which can be observed only in a slowly driven system. In the low-frequency regime, we experimentally demonstrate the existence of anomalous topological edge modes which are robust against defects.

7.2 Floquet theory

In this section, we describe the Floquet theory that will be used to investigate the dynamics of a driven two-dimensional lattice. We consider a static system, described by a Hamiltonian $\hat{H}_0$, that is driven in time, and we write the time-dependent Hamiltonian as $\hat{H}(t)$. In general, the time-dependent Hamiltonian, $\hat{H}(t)$, could be complicated and difficult to handle theoretically. However, in case of time-periodic driving, i.e. $\hat{H}(t) = \hat{H}(t+T)$ where the frequency of driving is $\omega = 2\pi/T$, one can use Floquet theory to analyse the system theoretically. In analogy with the static system, the evolution of a periodically driven system is described by the Floquet basis states: $|\Psi(t)\rangle = |\Phi(t)\rangle\, e^{-i\varepsilon t}$ where $|\Phi(t+T)\rangle = |\Phi(t)\rangle$ and ε is called the quasienergy defined on a quasienergy Brillouin zone $\{-\pi/T \leq \varepsilon \leq \pi/T\}$. The behaviour of the system is analysed in terms of the evolution operator, $\hat{U}(T)$, of the system over one full period of the driving:

$$\hat{U}(T) = \mathcal{T} \exp\left[-i \int_0^T \hat{H}(t)\mathrm{d}t\right], \tag{7.1}$$

where $\mathcal{T}$ indicates the time ordering. After each period of driving, each Floquet state is mapped into itself up to a phase: $|\Psi(t)\rangle = \hat{U}(t)\,|\Psi(0)\rangle = e^{-i\varepsilon t}\,|\Psi(0)\rangle$. For a given time-modulation, $\hat{H}(t)$, Eq. (7.1) is numerically integrated and diagonalised to obtain the quasienergies.

7.3 Slowly-driven square lattice

We consider the tight binding model for a square lattice which is inspired by the lattice proposed in Rudner et. al. [144]. The lattice is driven in the following way. The hopping amplitudes (or coupling strengths) between lattice sites are varying in a spatially homogeneous but time-periodic way, see Fig. 7.1 (a). The total driving period (z_0) is equally divided into four. During each $1/4$-th of a complete period, the coupling is allowed only along one of the four nearest neighbours [shown by the solid coloured lines in Fig. 7.1 (a)]. The magnitude of the coupling strengths are κ_i ($i = 1, 2, 3$ and 4). The unit cell is indicated by the grey-coloured square in Fig. 7.1 (b). The Hamiltonian

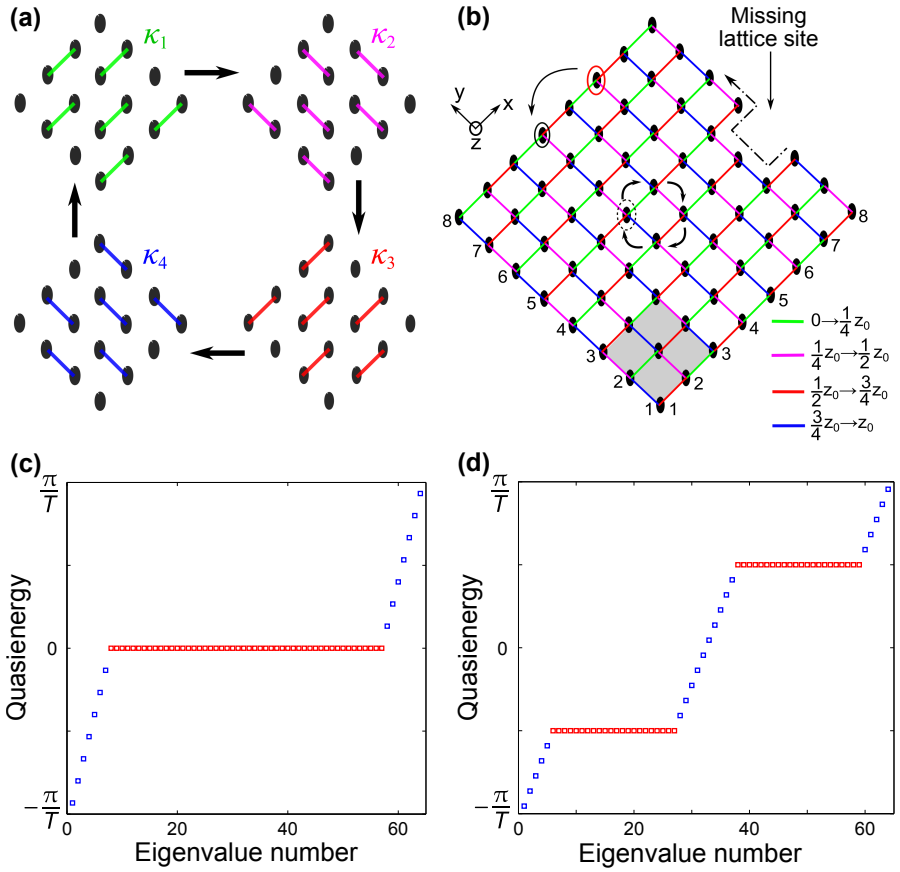

Fig. 7.1: Schematic diagram of a periodically driven square lattice: chiral edge modes and localised bulk modes. (a) The hopping amplitudes are varying in a spatially homogeneous but time-periodic way. The total period (z_0) is equally divided into four. The magnitude of the coupling strengths are κ_i ($i = 1, 2, 3$ and 4) respectively. (b) For $\kappa_i z_0/4 = \pi/2$, if a waveguide in the bulk of the lattice (shown by the dotted circle) is excited in this lattice, it is expected that the light will cycle back to the excitation waveguide after each period. In other words, the bulk state is localised. However, when a waveguide at the edge (as shown by the solid circle) is excited, the light propagates along the edge and does not penetrate into the bulk. The edge modes are insensitive to a broken bond (or a missing waveguide) at the edge. (c) Floquet spectrum for the simplest situation: $\Lambda_i = \pi/2$ for all the bonds, where $\Lambda_i = \kappa_i z_0/4$. The red squares indicate the two degenerate bulk bands. The blue squares correspond to the edge modes. (d) If the lattice is driven with $\Lambda_1 = 0$ and $\Lambda_{2,3,4} = \pi/2$, the bulk bands are flat and well separated.

that describes this system is periodic in z (z is analogous to time) and using Floquet theory [145, 146] one can obtain the band structure.

Consider that the lowest Bloch bands, separated from the higher energy bands by a large band gap, are only excited initially. In this situation, the higher Bloch bands are

not excited when the system is observed stroboscopically (after each full period); see Ref. [147]. The Floquet operator for the above-mentioned driven lattice can be written as:

$$\hat{U}(z_0) = e^{-i\hat{H}_4 z_0/4} e^{-i\hat{H}_3 z_0/4} e^{-i\hat{H}_2 z_0/4} e^{-i\hat{H}_1 z_0/4}, \tag{7.2}$$

where the Hamiltonian, $\hat{H}_n$ ($n = 1, 2, 3$ and 4) is piecewise constant in (analogous) time within the interval $(n-1)z_0/4 \leq z_0 \leq nz_0/4$. Here we consider two different types of driving and numerically calculate the quasienergies.

Case 1: First, we investigate the simplest situation: $\Lambda_i = \pi/2$ for all the bonds, where $\Lambda_i = \kappa_i z_0/4$. This means that a particle will hop to its nearest neighbour site after $1/4$-th of the complete period with $100\ \%$ probability if the coupling between them is allowed. In this situation, a particle in the bulk [shown by the dotted circle in Fig. 7.1 (b)] moves in closed trajectories which means that the bulk state is localised. When this system is observed stroboscopically, the effective static Hamiltonian ($\hat{H}_{\text{eff}}$) vanishes as the evolution operator, $\hat{U}(z_0) = 1$. Here the Floquet spectrum consists of two degenerate bulk bands at quasienergy zero [Fig. 7.1 (c)]; the chiral edge modes are shown in by blue squares. It should be highlighted that Chern number for the bulk bands has to be zero in this case as the bands are gap-less. Hence, the edge modes are "anomalous".

Case 2: Let us imagine that the green bonds in Fig. 7.1 (a, b) are always off which means $\Lambda_1 = 0$. For other three bonds $\Lambda_{2,3,4} = \pi/2$. In this situation, the Floquet spectrum, Fig. 7.1 (d), consists of two non-degenerate flat bends with zero Chern number. Most importantly, as the bulk bands well separated, small disorder (less than the energy gap between the bulk bands) cannot close the energy gap. In the following sections, the experimental realisation of the anomalous edge modes with the above-mentioned driving protocols will be presented.

7.4 Photonic implementation: tapered directional couplers

For the experimental realisation of the model described in Section 7.3, we consider a photonic square lattice with initially uncoupled waveguides. To turn on the coupling between any two desired waveguides, the inter-waveguide separation is reduced by curving the axes of the waveguides in x-y-z, such that the waveguides propagate together for for a straight section of length L_2. After this interaction region, the waveguides are again

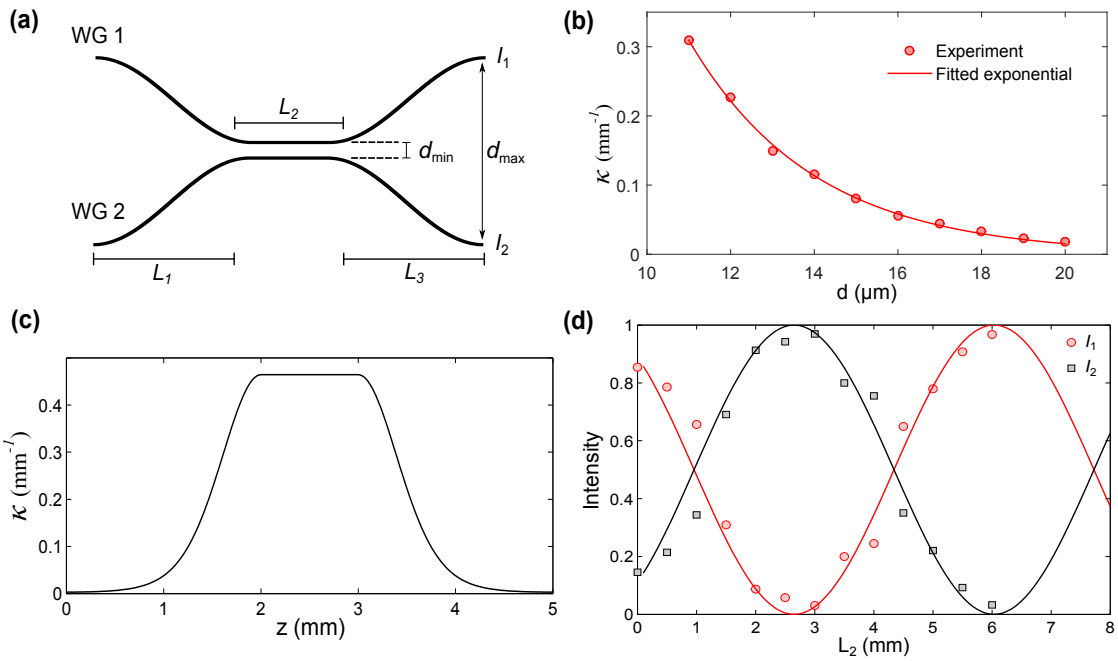

Fig. 7.2: (a) Schematic diagram of a directional coupler consisting of two synchronously bending waveguides, WG 1 and WG 2. The separation between the waveguides is $d(z)$, where z is the propagation direction, $d_{\text{max}} = \max[d(z)]$, and $d_{\text{min}} = \min[d(z)]$. (b) Experimentally measured variation of coupling strength as a function of separation, d, between two coupled straight waveguides. The solid line is the exponential fit. (c) Estimated variation of $\kappa(z)$ along the propagation direction of the coupler, shown in (a), with $L_2 = 1$ mm. (d) Experimentally measured (filled squares and filled circles) and theoretically predicted (solid lines) variation of intensities, (I_1, I_2), as a function of L_2.

separated in a reverse manner. In other words, each bond in the lattice is a tapered directional coupler with two *slowly* and *synchronously* bending optical waveguides, which are evanescently coupled in the middle [see Fig. 7.2 (a)]. For a particular wavelength, the coupling that occurs between two slowly and synchronously bending waveguides is equivalent to an effective tight binding coupling between two straight waveguides (see Ref. [148]). For such a directional coupler, when WG 1 is excited at the input, the normalised output intensities are given by [148]

$$I_1 = \cos^2(\phi) \quad \text{and} \quad I_2 = \sin^2(\phi),$$
$$\text{where} \quad \phi = \int_0^z \kappa(z)\mathrm{d}z. \tag{7.3}$$

To obtain Eq. (7.3), it is assumed that the tilt of the wavefront due to the bending of the waveguide axis is negligible (paraxial approximation). Hence, it is necessary to check

the validity of Eq. (7.3) to show that paraxial approximation is indeed applicable.

To experimentally verify the validity of Eq. (7.3), we fabricated thirteen sets of couplers with $L_1 = L_3 = 2$ mm, $d_{\text{max}} = 40$ μm, $d_{\text{min}} = 9.5$ μm and $0 \leq L_2 \leq 6$ mm; the bending profile of the two waveguides are shown in Fig. 7.2 (a). In the bending region, each waveguide bends as a sine-squared function. In Fig. 7.2 (d), the measured variation of output intensities, (I_1, I_2), are plotted as a function of L_2.

To theoretically explain the measured variation of (I_1, I_2), we estimated $\kappa(z)$ in the following way. First, we experimentally measured how $\kappa(d)$ varies as a function of the separation, d, between two coupled straight waveguides, and an exponentially decaying behaviour was observed as shown in Fig. 7.2 (c); see also Section 3.3. From this, we then estimated the variation of $\kappa(z)$ as a function of z, as the separation, $d(z)$, between the two waveguides of the coupler is known. Fig. 7.2 (c) shows this variation for $L_2 =$ 1 mm. Using Eq. (7.3), we plotted (I_1, I_2) as a function of L_2 [solid lines in Fig. 7.2 (d)] which is in excellent agreement with our experimental result. Fig. 7.2 (d) proves that Eq. (7.3), and hence, the paraxial approximation made to obtain this equation is valid for ultrafast laser inscribed tapered directional coupler with slow bending.

7.5 Fabrication of slowly driven photonic lattices

To implement the scheme described in Section 7.3, we fabricate a photonic square lattice where all the waveguides are initially separated by 40 μm, such that they are effectively uncoupled. To turn on coupling between any two desired lattice sites, the inter-waveguide separation is reduced by synchronously bending the axes of the waveguides in x-y-z, and moving them closer as described in Section 7.4. As discussed in the previous sections, the control of the parameter $\Lambda_i = \kappa_i z_0/4$ is crucial. In the experiment z_0 was chosen to be fixed. The magnitude of coupling constant was controlled by correctly choosing the inter-waveguide separation, and precisely tuned by varying the wavelength of light.

The photonic lattices with two driving periods were fabricated inside a 70 mm-long glass (Corning Eagle^{2000}) substrate using the ultrafast laser inscription technique; the refractive index profile of each waveguide was controlled using the slit beam shaping method; see Section 3.2.3. Each waveguide was inscribed by translating the glass substrate at a translation speed of 6 mm/s, once through the focus of a 500 kHz train of 1030 nm

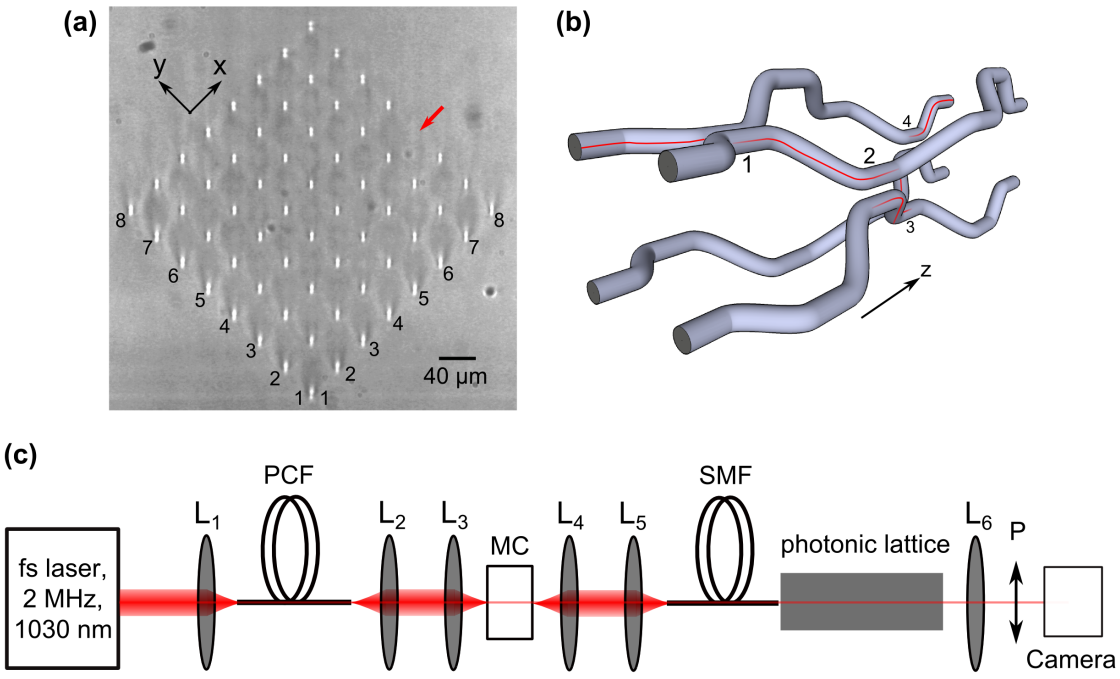

Fig. 7.3: (a) White-light-micrograph of the input facet of the slowly-driven photonic square lattice. The red arrow indicates a missing waveguide [(8, 4) lattice site] which acts like a defect. (b) A cartoon of the three-dimensional waveguide paths for $\Lambda_i = \kappa_i z_0/4 = \pi/2$ ($i = 1, 2, 3$ and 4). (c) Schematic diagram of the experimental set-up to excite different lattice sites. A photonic crystal fibre (PCF) was pumped using sub-picosecond laser pulses of 1064 nm wavelength to generate supercontinuum light. A tunable monochromator (MC) placed after the supercontinuum source transmits a narrow band (~ 3 nm) of light which was coupled to a fibre (SMF-600). The fibre was coupled to the lattice sites. Here L_1-L_6 are convex lenses. The output intensity distribution was observed in a CMOS camera. A polariser (P) passing only vertically polarised light is placed in front of the camera to ensure that the measurements are not affected by polarisation-dependent coupling.

femtosecond (fs) laser pulses. The laser inscription parameters were optimised to produce waveguides that were single-mode and well confined in the wavelength range: 700-830 nm. To study the response of the edge modes in the presence of a defect at the edge, the waveguide at the (8, 4) lattice site was not fabricated. The white-light-transmission micrograph of a lattice is shown in Fig. 7.3 (a). A schematic diagram of the three-dimensional waveguide paths is shown in Fig. 7.3 (b).

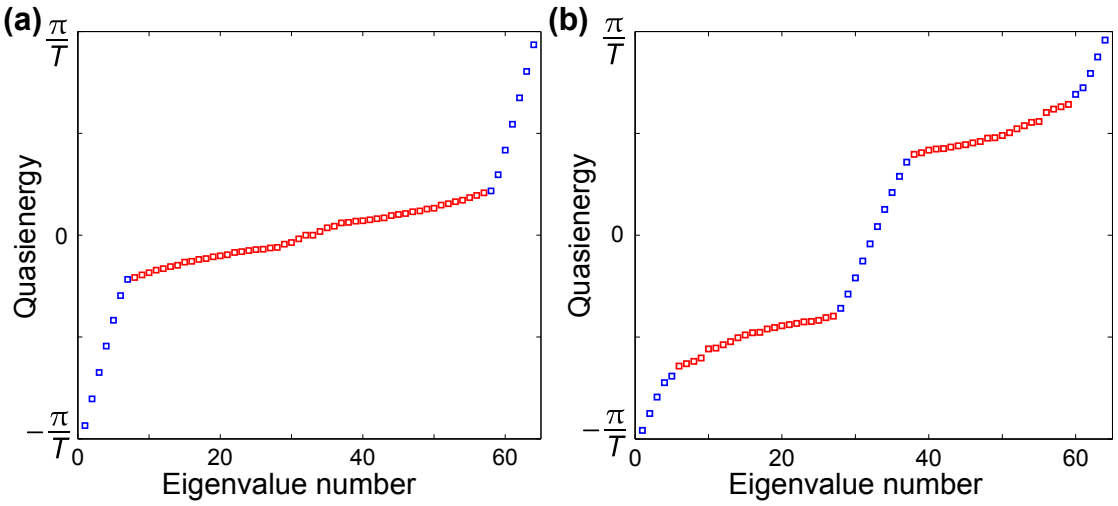

Fig. 7.4: Floquet spectrum when (a) all four bonds (with slightly different strengths) are on with $\lambda_{1,2,3,4} \approx \pi/2$, (b) three bonds (with slightly different strengths) are on with $\Lambda_{2,3,4} \approx \pi/2$ and $\Lambda_1 = 0$; see also Fig. 7.6. The red squares indicate the bulk band(s). The blue squares correspond to the edge modes.

7.6 Characterisation of slowly driven photonic lattices

The lattices were characterised using single-mode-fibre input coupling and free-space output coupling, see Fig. 7.3 (c). As mentioned in the previous section, wavelength tunability of the incident light is required for the precise control of Λ_i. To achieve this a photonic crystal fibre (PCF) was pumped using sub-picosecond laser pulses of 1064 nm wavelength to generate supercontinuum light. A tunable monochromator (MC) placed after the supercontinuum source transmits a narrow band (~ 3 nm) of light which was coupled to a fibre (SMF-600). The fibre was then coupled to the lattice sites. The output intensity distribution was observed in a CMOS camera. A polariser (P) passing only vertically polarised light is placed in front of the camera to ensure that the measurements are not affected by polarisation-dependent coupling.

Case-1 First we consider the driving protocol for which all bonds have equal strength, $\Lambda_i = \kappa_i z_0/4 = \pi/2$ ($i = 1, 2, 3$ and 4). At 785 nm wavelength almost complete transfer of light was observed between two coupled lattice sites; see also Fig. 7.9 (b). As shown in Fig. 7.4 (a), the bulk bands become dispersive when Λ_i are slightly different from the desired value $\pi/2$. In this situation, when edge modes are excited by individually launching light at (8, 8), (4, 8), and (1,7) lattice sites, it was observed that the light propagates along the edge and does not penetrate into the bulk [Fig. 7.5 (a-c)]. As the

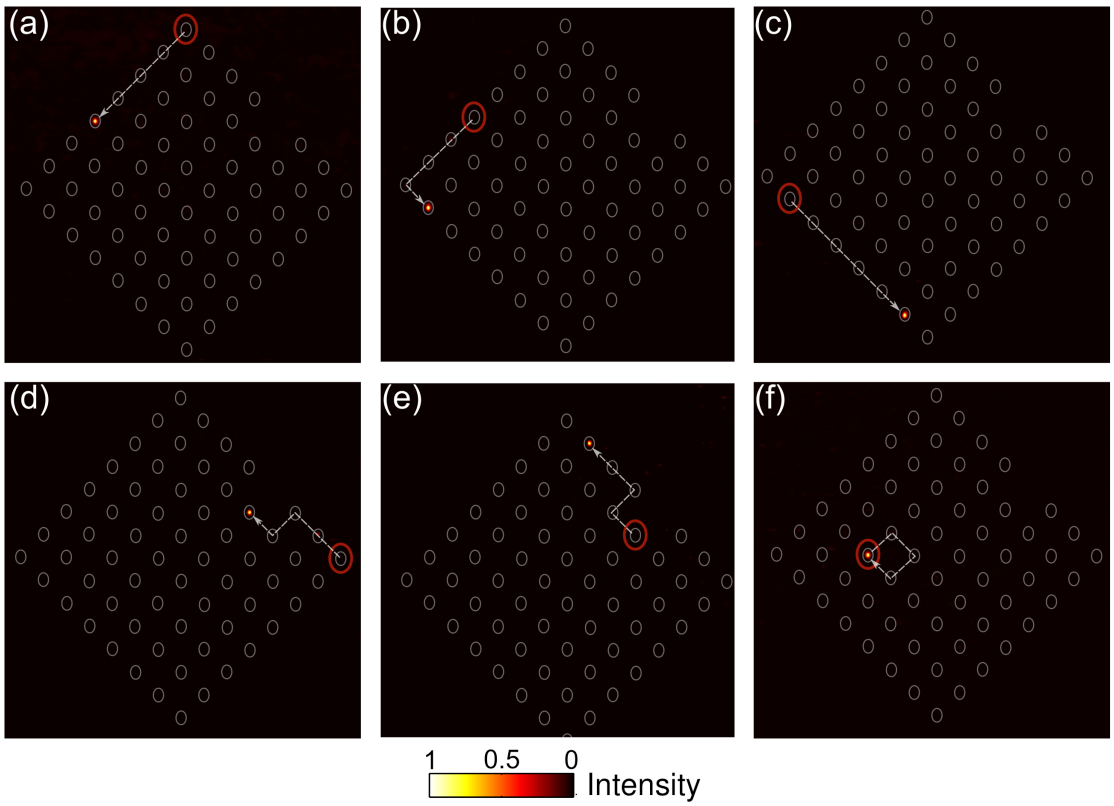

Fig. 7.5: Experimentally observed anomalous topological edge modes and largely localised bulk modes in a periodically driven photonic square lattice. Total length of the lattice is $2z_0$ (z_0 is the period of driving). When $\Lambda_{1,2,3,4} \approx \pi/2$, we observe chiral edge modes (a-c) which are robust against defects [in this case a missing lattice site] (d, e) and the bulk state is largely localised (f). The lattice site that was excited at the input for each measurement is indicated by the red circle. Each image is normalised so that the total power is 1. Band structure for this lattice was shown in Fig. 7.4 (a). See Ref. [149] for a similar experimental work.

total length of the lattice is equal to two driving periods ($2z_0$), the edge modes propagate by two lattice constants along the edge. To demonstrate the robustness of these edge modes against a defect (a missing lattice site), we launch light at (8, 1) and (7, 4) sites and observe that the edge modes propagate around that defect without any back-scattering [Fig. 7.5 (d, e)]. In other words, the edge modes are insensitive to defects. We then excite (3, 6) lattice site at the bulk of the lattice [Fig. 7.5 (f)] and observe a negligible spread of the analogous wavefunction as the bulk band is slightly dispersive and we are measuring the intensity distribution only after two driving periods.

Case-2 In the above-mentioned experiment, we have observed anomalous edge modes when the two bulk bands are degenerate. Now we investigate another type of driving

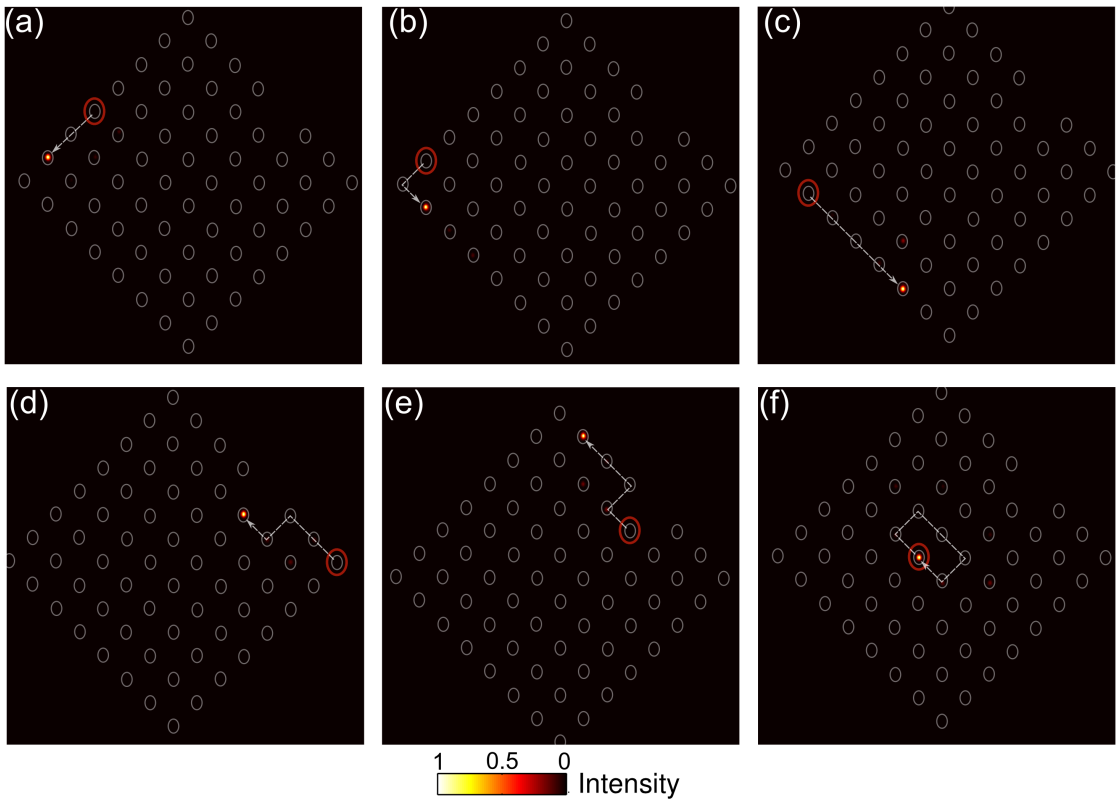

Fig. 7.6: Experimentally observed anomalous topological edge modes and largely localised bulk modes in a periodically driven photonic square lattice with $\Lambda_1 = 0$ and $\Lambda_{2,3,4} \approx \pi/2$. (a-c) Observed chiral edge modes which are robust against defects (d, e) and the bulk state is largely localised (f). The lattice site that was excited at the input for each measurement is indicated by the red circle. Each image is normalised so that the total power is 1. Band structure for this lattice was shown in Fig. 7.4 (b).

protocol where the bulk bands are well separated. We consider a similar engineered photonic lattice where the first bond [the green bond in Fig. 7.1 (a, b)] is never turned on. This means for the first $z_0/4$ length of each period, all the waveguides are straight and uncoupled. The other three bonds are designed to achieve almost complete transfer of light. In other words, $\Lambda_{2,3,4} \approx \pi/2$. To characterise the bonds present in the lattice, and hence validate our theoretical model, we fabricated five sets of each bond in isolation, inside the same substrate, and measured their behaviour as a function of the wavelength of light. When characterised with 785 nm light, the mean and standard deviation of Λ_i ($i = 2, 3, 4$) were found to be $\Lambda_2 = \pi/2(1.16 \pm 0.04)$, $\Lambda_3 = \pi/2(1.15 \pm 0.04)$, $\Lambda_4 = \pi/2(0.085 \pm 0.03)$. For the bond κ_1, all the light remains in the waveguide excited at the input, which indicates no transfer of light ($\Lambda_1 = 0$). In this situation, there are equal number of edge modes above and below each bulk bands [see Fig. 7.4], and

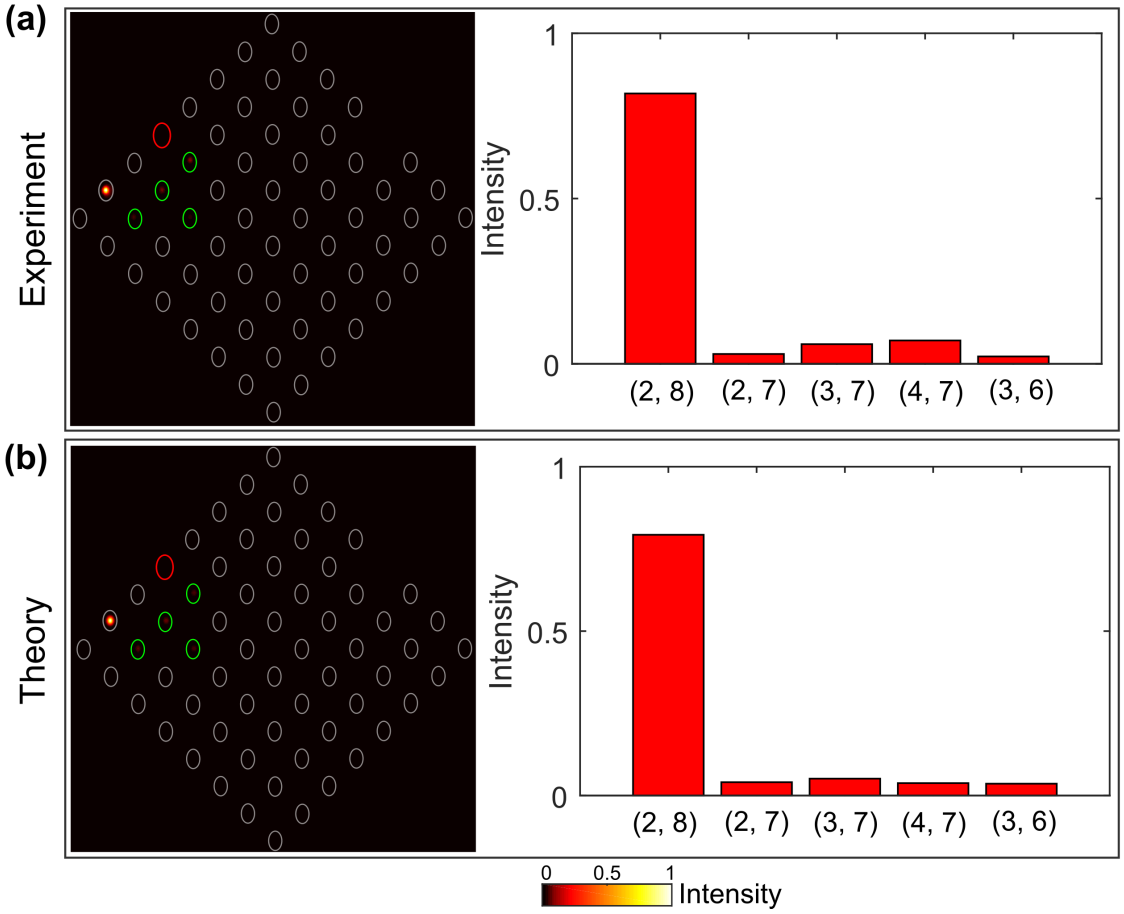

Fig. 7.7: (a) Same result as in Fig. 7.6 (a), but using a different colour-scale so as to highlight the low intensities (bulk response). The right panel shows the relative light intensity at the five lattice sites indicated by green circles (left panel), where light was detected at the output. (b) Theoretical simulation of the intensity distribution, from a numerical resolution of the Schrödinger equation associated with the Floquet (effective) Hamiltonian. The sites coordinates indicated in the right panels correspond to the axis orientation of Fig. 7.3 (a).

hence, the bulk bands are anomalous (Chern zero). We excited the edge modes by individually launching light at (4, 8), (2, 8) and (1,7) lattice sites respectively. The observed output intensity distributions are shown in Fig. 7.6 (a-c). Fig. 7.6 (b) shows that the edge modes are not scattered by corners. The response of the edge modes to a missing waveguide [Fig. 7.6 (d, e)] is the same as shown in Fig. 7.5 (d-e). Fig. 7.6 (f) shows the largely localised output intensity when the bulk bands are excited.

In our experiment, the excitation of a single lattice site on the edge cannot excite the edge modes with unit efficiency. This happens due to the fact that $\Lambda_{2,3,4}$ are slightly different from the ideal values. Note that the residual excitation of the bulk was exper-

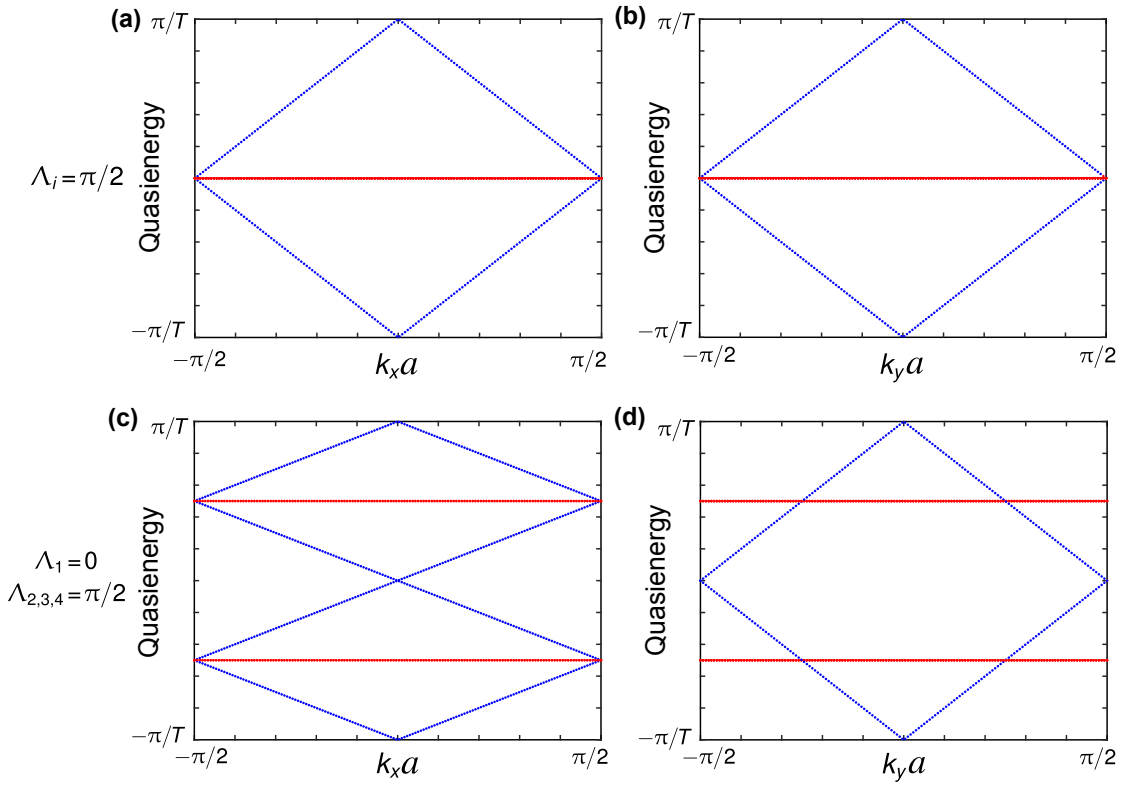

Fig. 7.8: Floquet spectrum calculated considering the strip geometries for (a, b) $\Lambda_i = \pi/2$ and (c, d) $\Lambda_1 = 0$, $\Lambda_{2,3,4} = \pi/2$. The quasienergies for the edge modes are shown in blue, and that for the bulk bands are in red.

imentally observed in Fig. 7.6 (a-e). To highlight this fact, we show the relative output intensities at various edge and bulk lattice sites in Fig. 7.7, which shows good agreement with a theoretical simulation. The latter was performed by inserting the mean values of J_i extracted from the experiment into the effective Hamiltonian, and resolving the corresponding Schrödinger equation numerically.

It should be noted that the group velocity of the edge modes on the top-left edge [Fig. 7.6 (a)] is half of that on the bottom-left edge [Fig. 7.6 (c)]. To explain this, Floquet spectrum was calculated considering the strip geometries; see Appendix B. As shown in Fig. 7.8 (c, d), the group velocity of the edge modes (i.e. the slope of the edge modes in Floquet spectrum) along the y axis is twice of that on the x axis, which was observed in the experiment. Also note that the group velocity of the edge modes is equal on both edges when all the four bonds have equal strength with $\Lambda_i = \pi/2$, see Fig. 7.8 (a, b), which was observed in Fig. 7.5 (a, c).

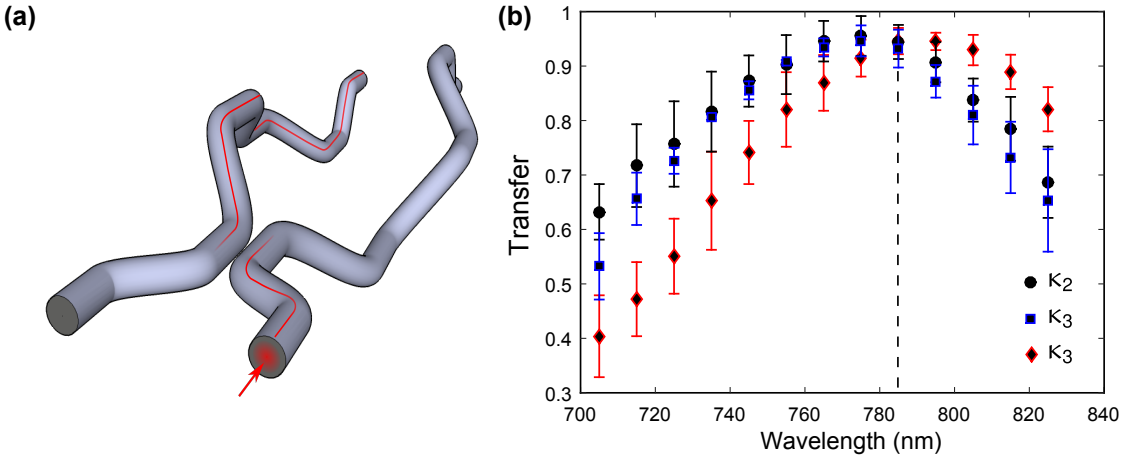

Fig. 7.9: (a) A cartoon of a directional coupler (evanescently coupled two-waveguides) which acts as the bond in the driven lattice. Each bond was fabricated with identical waveguide paths as used to inscribe the photonic lattice to characterise the four bonds. (b) Variation of coupling constant, κ_i $(i=2,3,4)$, as a function of wavelength. The error bars indicate the measured standard deviation. κ_1 was measured to be zero.

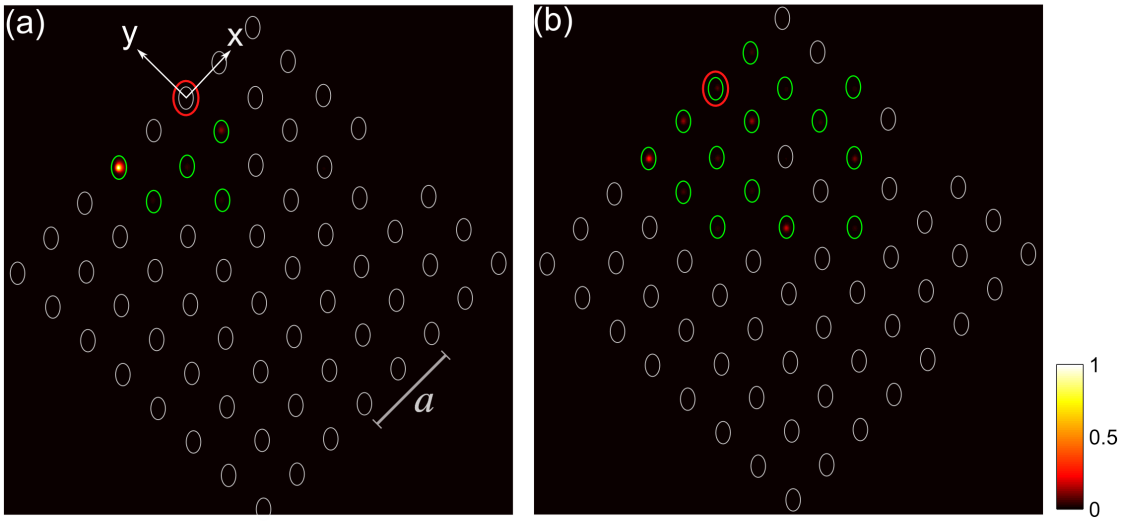

Fig. 7.10: Same as Fig. 7.6 with wavelength of incident light (a) 785 nm [i.e. $\Lambda_{2,3,4} \approx \pi/2$, $\Lambda_1 = 0$] and (b) 735 nm [i.e. $\Lambda_{2,3,4} \approx 0.65\pi/2$, $\Lambda_1 = 0$] respectively. The green circles indicate the lattice sites where light intensity was detected at the output. Each image is normalized so that the total power is 1.

7.7 Wavelength tuning

The refractive index profile of a photonic lattice is a function of wavelength, and by tuning the wavelength of incident light the evanescent coupling can be tuned. Wave-

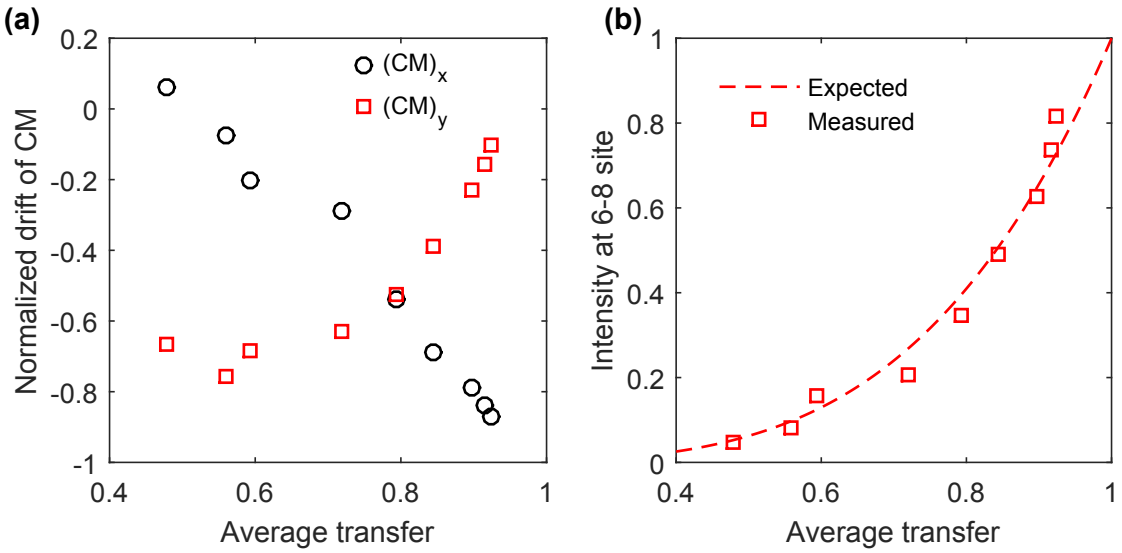

Fig. 7.11: (a) Variation of centre of mass (CM) along the two lattice axes as a function of average transfer of light. (b) Variation of output intensity (measured and expected) at the (6-8) lattice site as a function of average transfer of light.

length tuning also changes the propagation constant (i.e. the analogous site energy) of each waveguide, but this effect is not important for our experiments as the site energy can be chosen to be zero. Here we are interested in the wavelength range (i.e. 700 nm to 830 nm) for which each waveguide supports only the fundamental mode. In this section, we will discuss the effects of wavelength tuning for the lattice shown in Fig. 7.6; see also [150]. As mentioned in the previous section, to characterise each bond in the lattice we fabricated five sets of each bond (evanescent coupler) in isolation. The mean and standard deviation of the transfer of light, which is a measure of Λ_i, for three types of bonds ($i = 2, 3, 4$) are shown in Fig. 7.9. For the first bond the transfer of light was insignificant in the wavelength range of interest. It should be mentioned that the transfer of light is defined as: transfer $= P_2/P_1 = \sin^2(\Lambda)$, where P_1 and P_2 are the output power in the two arms [see Fig. 7.9] of the coupler.

We inject light at the (6-8) lattice site and tuned the wavelength using the monochromator shown in Fig. 7.3 (c). It was observed that as the transfer of light reduces from $\sim 100\%$ for the three bonds ($i = 2, 3, 4$), light starts to penetrate into the bulk. The output intensity distributions for 785 nm and 735 nm wavelength are presented in Fig. 7.10 (a, b) respectively. To quantify this penetration of light into the bulk of the lattice, we calculate the x and y components of the drift of the centre of mass [defined as $\sum_{l,m} I_{l,m}\boldsymbol{r}_{l,m}$] relative to the initially excited lattice site; see Fig. 7.11 (a). Note that for the specific

incident-light wavelength (785 nm) for which the average transfer is close to unity, it was found that $(\text{CM})_x \approx -a$ and $(\text{CM})_y \approx 0$, which is in agreement with the edge-mode (chiral) displacement observed in Fig. 7.10 (a). Fig. 7.11 (b) shows that the light intensity at (6-8) site varies as $(\text{transfer})^{-4}$ as would be expected. Here we have only demonstrated the capability of wavelength tuning which can be used, in principle, to investigate different topological phases (shown in Ref. [150]).

7.8 Chapter summary

In this chapter, we presented slowly driven photonic square lattices and demonstrated the existence of chiral topological edge modes which are robust against defects. The theoretical analysis shows that these edge modes have no static analogue and hence they are anomalous. In other words, these edge modes are associated with a distinct topological invariant known as the winding number. In future work, we expect to observe interesting phenomena in this system in the presence of nonlinearity.

This page is intentionally left blank.

Chapter 8

Conclusions and future work

8.1 Conclusions

In this thesis, we have mainly focused on various localisation effects in the periodic arrays of coupled optical waveguides. The experimental techniques were discussed in detail. We have also presented brief theoretical analysis for the completeness of the discussion. Most of the phenomena discussed in this work are well-known and well-studied in theoretical condensed matter physics, and the experimental work presented here proves the capabilities of the photonic system as a powerful and clean simulator which is an interesting alternative to cold atomic systems. The experimental results presented here offer new opportunities to study single and two-particle dynamics, and as such are of interest to a wide audience of researchers in quantum optics, photonics, cold atomic gases and condensed matter physics.

Here we summarise the main achievements of this work. The theoretical analysis of the straight and curved photonic lattices was briefly discussed in Chapter 2. We derived the Schrödinger-like equation that governs the propagation of light waves across a photonic lattice and introduced the concept of evanescent coupling. Calculations of the band structure using the tight binding model were presented for one-dimensional and two-dimensional lattices. In Chapter 3, we briefly summarised the ultrafast laser inscription technique and measurement of evanescent coupling and waveguide refractive index. In Chapter 4, we presented a novel technique of light-trapping using lattice geometries that support flat-band(s) in the energy spectrum. In Chapter 5, we discussed how one can simulate the dynamics of a single particle in a periodic potential with static and periodic driving. Here we demonstrated optical analogue of Wannier-Stark localisation and photon assisted tunnelling. We also demonstrated that it is possible to emulate a two-particle one-dimensional Hubbard model with unprecedented level of control using photonic lattices in Chapter 6. There we demonstrated suppression of standard 1-st order

tunnelling, observation of pair tunnelling and coherent destruction of tunnelling for the paired particles. In Chapter 7, we demonstrate a novel type of edge modes, which has no static analogue, using a slowly-driven photonic square lattice. These robust chiral edge modes, known as anomalous topological modes, exist even if all the bulk bands are topologically trivial.

8.2 Future work

It is of great interest to investigate single particle physics in the presence of a uniform magnetic flux. Experimental achievements of this thesis clearly indicate the possibility to realise a synthetic uniform magnetic flux by correctly engineering the propagation constant along the propagation direction. In this context, we have discussed the photonic Aharonov-Bohm photonic caging that can be observed in a rhombic lattice geometry; see Section 4.2.6. Specific phenomena in flat-band lattices, such as Landau-Zener Bloch Oscillations [151], disorder (Anderson) and nonlinearity induced localisation [152], have recently attracted great attention in theoretical physics, and can be successfully realised in the photonic setups. The experimental setup discussed in Chapter 6 can be used to study various two-body problems such as fermionisation of two bosons in the strong interaction regime. In this work, we discussed coherent destruction of tunnelling for the paired state in a one-dimensional (tight binding) lattice driven by an analogous external force with high frequency. Experimental investigation of a similar phenomenon in the low frequency regime will be interesting. The demonstration of anomalous edge modes (Chapter 7) opens up the possibilities to experimentally investigate similar phenomena in the presence of nonlinearity and disorder [153].

This page is intentionally left blank.

Appendix A

Photographs

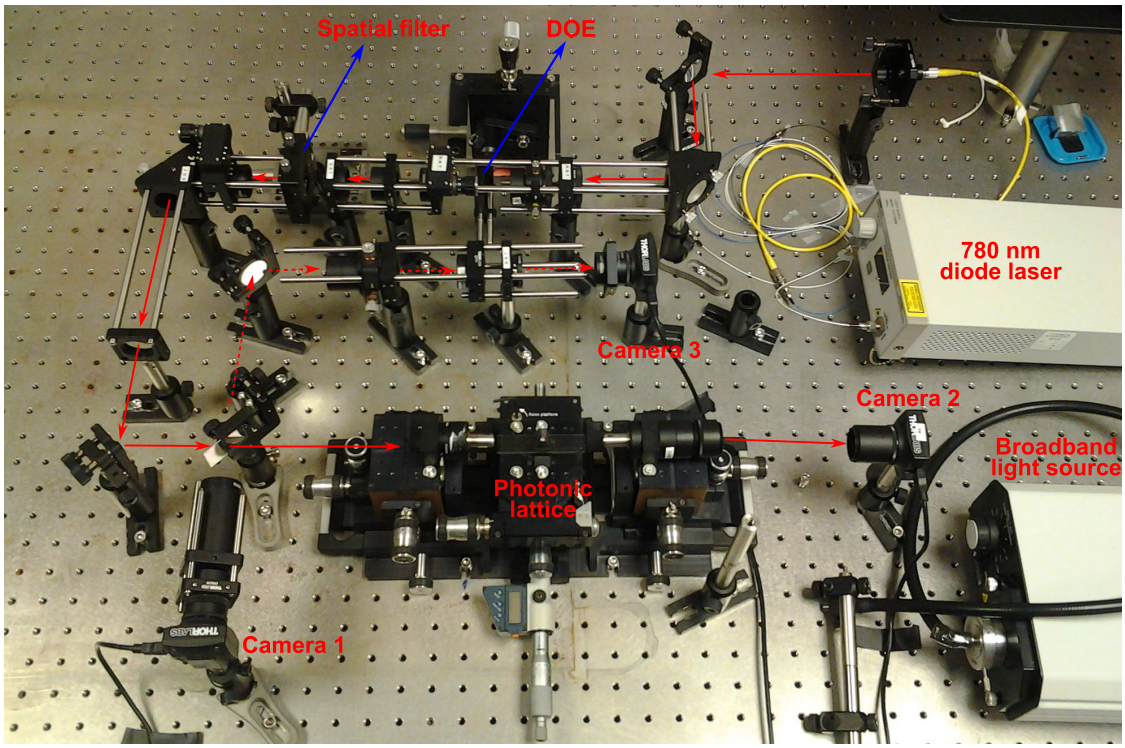

Fig. A.1: Experimental setup for exciting the desired lattice sites at the input of the photonic rhombic/Lieb lattice (Photonic Instrumention Group, Heriot-Watt University). See also Fig. 4.3 for the schematic diagram.

Appendix B

Floquet quasienergy spectrum using the strip geometry

Here, we consider a square lattice with two lattice sites (A and B) per basis (see Fig. B.1), which is very similar to the driven lattice discussed in Chapter 7. However, for the time being, we ignore the modulation of the of the Hamiltonian in time. The hopping amplitudes are denoted by $\kappa_1, \kappa_2, \kappa_3$ and κ_4. Note that the lattice is periodic along the y direction, and finite along the x direction. For simplicity we have considered only four sites the x direction. To obtain the band structure for this strip geometry, we first

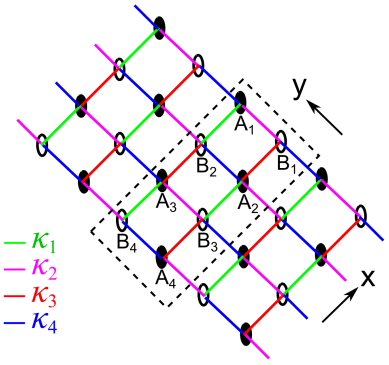

Fig. B.1: Strip geometry which is periodic along y direction.

write the Hamiltonian in the real space, considering the unit cell indicated by the dashed rectangle in Fig. B.1.

$$\begin{aligned}\hat{H} = -\sum_{m} \big[&\kappa_2 \hat{B}^{\dagger}_{1,m}\hat{A}_{1,m} + \kappa_4 \hat{A}^{\dagger}_{1,m+1}\hat{B}_{1,m} + \kappa_4 \hat{A}^{\dagger}_{2,m}\hat{B}_{2,m} + \kappa_2 \hat{B}^{\dagger}_{2,m+1}\hat{A}_{2,m} \\ &+ \kappa_2 \hat{B}^{\dagger}_{3,m}\hat{A}_{3,m} + \kappa_4 \hat{A}^{\dagger}_{3,m+1}\hat{B}_{3,m} + \kappa_4 \hat{A}^{\dagger}_{4,m}\hat{B}_{4,m} + \kappa_2 \hat{B}^{\dagger}_{4,m+1}\hat{A}_{4,m} \\ &+ \kappa_1 \hat{B}^{\dagger}_{2,m}\hat{A}_{1,m} + \kappa_3 \hat{A}^{\dagger}_{2,m}\hat{B}_{1,m} + \kappa_3 \hat{A}^{\dagger}_{3,m}\hat{B}_{2,m} \\ &+ \kappa_1 \hat{B}^{\dagger}_{3,m}\hat{A}_{2,m} + \kappa_1 \hat{B}^{\dagger}_{4,m}\hat{A}_{3,m} + \kappa_3 \hat{A}^{\dagger}_{4,m}\hat{B}_{3,m}\big] + \text{h.c.}\end{aligned} \tag{B.1}$$

Notations and symbols have their usual meaning. After Fourier transformation, Eq. (B.1) can be written as:

$$\hat{H} = \sum_{k} \begin{pmatrix} \hat{\mathbf{A}}^{\dagger}_{k} & \hat{\mathbf{B}}^{\dagger}_{k} \end{pmatrix} \hat{H}_k \begin{pmatrix} \hat{\mathbf{A}}_{k} \\ \hat{\mathbf{B}}_{k} \end{pmatrix}, \tag{B.2}$$

where $\hat{\mathbf{M}}_k \equiv (\hat{M}_1 \;\; \hat{M}_2 \;\; \hat{M}_3 \;\; \hat{M}_4)$, and

$$\hat{H}_k = \begin{pmatrix} 0 & 0 & 0 & 0 & -\Delta_1 & -\kappa_1 & 0 & 0 \\ 0 & 0 & 0 & 0 & -\kappa_3 & -\Delta_2 & -\kappa_1 & 0 \\ 0 & 0 & 0 & 0 & 0 & -\kappa_3 & -\Delta_1 & -\kappa_1 \\ 0 & 0 & 0 & 0 & 0 & 0 & -\kappa_3 & -\Delta_2 \\ -\Delta_3 & -\kappa_3 & 0 & 0 & 0 & 0 & 0 & 0 \\ -\kappa_1 & -\Delta_4 & -\kappa_3 & 0 & 0 & 0 & 0 & 0 \\ 0 & -\kappa_1 & -\Delta_3 & -\kappa_3 & 0 & 0 & 0 & 0 \\ 0 & 0 & -\kappa_1 & -\Delta_4 & 0 & 0 & 0 & 0 \end{pmatrix} \tag{B.3}$$

In Eq. (B.3), $\Delta_1 = \kappa_4 \exp(ika) + \kappa_2$, $\Delta_2 = \kappa_4 + \kappa_2 \exp(-ika)$, $\Delta_3 = \kappa_2 + \kappa_4 \exp(-ika)$, and $\Delta_4 = \kappa_2 \exp(ika) + \kappa_4$.

Now consider the driving protocol described in Section 7.3 (Case 1). In this case, the Hamiltonian, $\hat{H}_{k,n}$ ($n = 1, 2, 3$ and 4) is piecewise constant in (analogous) time within the interval $(n-1)z_0/4 \leq z_0 \leq nz_0/4$; z_0 is the total period. We can now construct the evolution operators defined as:

$$\begin{aligned} \hat{U}(k, z_0) &= \hat{U}_4 \hat{U}_3 \hat{U}_2 \hat{U}_1 \\ &= e^{-i\hat{H}_{k,4} z_0/4} e^{-i\hat{H}_{k,3} z_0/4} e^{-i\hat{H}_{k,2} z_0/4} e^{-i\hat{H}_{k,1} z_0/4}. \end{aligned} \tag{B.4}$$

It should be mentioned that the evolution operators are characterised by:

$$\begin{aligned} \hat{U}_1 &: \kappa_1 = \kappa, \quad \kappa_{2,3,4} = 0, \\ \hat{U}_2 &: \kappa_2 = \kappa, \quad \kappa_{1,3,4} = 0, \\ \hat{U}_3 &: \kappa_3 = \kappa, \quad \kappa_{1,2,4} = 0, \\ \hat{U}_4 &: \kappa_4 = \kappa, \quad \kappa_{1,2,3} = 0. \end{aligned} \tag{B.5}$$

Now the quasienergy spectrum is obtained from the effective Hamiltonian which can be evaluated as

$$\hat{H}_{\text{eff}}(k) = \frac{i}{z_0} \log \hat{U}(z_0). \tag{B.6}$$

The Floquet quasienergy presented in Fig. 7.8 (b) was numerically calculated using the Eq. (B.4)–(B.6) with $\kappa z_0/4 = \pi/2$.

This page is intentionally left blank.

References

[1] I. Bloch, "Ultracold quantum gases in optical lattices," *Nature Physics*, vol. 1, no. 1, pp. 23–30, 2005.

[2] D. Jaksch and P. Zoller, "The cold atom hubbard toolbox," *Annals of Physics*, vol. 315, no. 1, pp. 52–79, 2005.

[3] I. Bloch, J. Dalibard, and S. Nascimbène, "Quantum simulations with ultracold quantum gases," *Nature Physics*, vol. 8, no. 4, pp. 267–276, 2012.

[4] S. Longhi, "Quantum-optical analogies using photonic structures," *Laser & Photonics Reviews*, vol. 3, no. 3, pp. 243–261, 2009.

[5] I. L. Garanovich, S. Longhi, A. A. Sukhorukov, and Y. S. Kivshar, "Light propagation and localization in modulated photonic lattices and waveguides," *Physics Reports*, vol. 518, no. 1, pp. 1–79, 2012.

[6] J. C. Maxwell, "A dynamical theory of the electromagnetic field," *Proceedings of the Royal Society of London*, vol. 13, pp. 531–536, 1863.

[7] D. J. Griffiths, *Introduction to Electrodynamics*. Prentice-Hall, 1999.

[8] A. Ghatak and K. Thyagarajan, *An Introduction to Fiber Optics*. Cambridge university press, 1998.

[9] A. Yariv, *Quantum Electronics–3rd ed.* John Wiley & Sons, New York, 1989.

[10] S. M. Eaton, W.-J. Chen, H. Zhang, R. Iyer, J. Li, M. L. Ng, S. Ho, J. S. Aitchison, and P. R. Herman, "Spectral loss characterization of femtosecond laser written waveguides in glass with application to demultiplexing of 1300 and 1550 nm wavelengths," *Journal of Lightwave Technology*, vol. 27, no. 9, pp. 1079–1085, 2009.

[11] J. C. Bose, "On the influence of the thickness of air-space on total reflection of electric radiation," *Proceedings of the Royal Society of London*, vol. 62, no. 379-387, pp. 300–310, 1897.

[12] A. Sommerfeld, *Optics Lectures on Theortical Physics, Vol. IV*. New York, NY: Academic Press INC., p. 32, 1954.

[13] A. L. Jones, "Coupling of optical fibers and scattering in fibers," *Journal of the Optical Society of America*, vol. 55, no. 3, pp. 261–271, 1965.

[14] A. W. Snyder and J. D. Love, *Optical Waveguide Theory*. Chapman & Hall, London New York, p. 582, 1983.

[15] L. D. Landau and E. M. Lifshitz, *Course of Theoretical Physics, Volume 3: Quantum Mechanics–3rd ed.* Pergamon Press Ltd., p. 215, 1962.

[16] H. Fukuyama, R. A. Bari, and H. C. Fogedby, "Tightly bound electrons in a uniform electric field," *Physical Review B*, vol. 8, no. 12, p. 5579, 1973.

[17] F. Dreisow, M. Heinrich, A. Szameit, S. Doering, S. Nolte, A. Tünnermann, S. Fahr, and F. Lederer, "Spectral resolved dynamic localization in curved fs laser written waveguide arrays," *Optics Express*, vol. 16, no. 5, pp. 3474–3483, 2008.

[18] G. Lenz, I. Talanina, and C. M. De Sterke, "Bloch oscillations in an array of curved optical waveguides," *Physical Review Letters*, vol. 83, no. 5, p. 963, 1999.

[19] M. Heiblum and J. H. Harris, "Analysis of curved optical waveguides by conformal transformation," *IEEE Journal of Quantum Electronics*, vol. 11, pp. 75–83, 1975.

[20] W. C. Henneberger, "Perturbation method for atoms in intense light beams," *Physical Review Letters*, vol. 21, no. 12, p. 838, 1968.

[21] S. Longhi, D. Janner, M. Marano, and P. Laporta, "Quantum-mechanical analogy of beam propagation in waveguides with a bent axis: Dynamic-mode stabilization and radiation-loss suppression," *Physical Review E*, vol. 67, no. 3, p. 036601, 2003.

[22] S. Longhi, M. Marangoni, M. Lobino, R. Ramponi, P. Laporta, E. Cianci, and V. Foglietti, "Observation of dynamic localization in periodically curved waveguide arrays," *Physical Review Letters*, vol. 96, no. 24, p. 243901, 2006.

[23] J. Chan, T. Huser, S. Risbud, and D. Krol, "Structural changes in fused silica after exposure to focused femtosecond laser pulses," *Optics Letters*, vol. 26, no. 21, pp. 1726–1728, 2001.

[24] L. Sudrie, M. Franco, B. Prade, and A. Mysyrowicz, "Writing of permanent birefringent microlayers in bulk fused silica with femtosecond laser pulses," *Optics Communications*, vol. 171, no. 4, pp. 279–284, 1999.

[25] S. Juodkazis, K. Nishimura, S. Tanaka, H. Misawa, E. G. Gamaly, B. Luther-Davies, L. Hallo, P. Nicolai, and V. T. Tikhonchuk, "Laser-induced microexplosion confined in the bulk of a sapphire crystal: evidence of multimegabar pressures," *Physical Review Letters*, vol. 96, no. 16, p. 166101, 2006.

[26] D. Homoelle, S. Wielandy, A. L. Gaeta, N. Borrelli, and C. Smith, "Infrared photosensitivity in silica glasses exposed to femtosecond laser pulses," *Optics Letters*, vol. 24, no. 18, pp. 1311–1313, 1999.

[27] A. M. Streltsov and N. F. Borrelli, "Fabrication and analysis of a directional coupler written in glass by nanojoule femtosecond laser pulses," *Optics Letters*, vol. 26, no. 1, pp. 42–43, 2001.

[28] K. Minoshima, A. Kowalevicz, E. Ippen, and J. Fujimoto, "Fabrication of coupled mode photonic devices in glass by nonlinear femtosecond laser materials processing," *Optics Express*, vol. 10, no. 15, pp. 645–652, 2002.

[29] D. Choudhury, A. Arriola, J. Allington-Smith, C. Cunningham, and R. Thomson, "Towards freeform microlens arrays for near infrared astronomical instruments," in *SPIE Astronomical Telescopes+ Instrumentation*, pp. 915146–915146, International Society for Optics and Photonics, 2014.

[30] G. D. Marshall, M. Ams, and M. J. Withford, "Direct laser written waveguide-bragg gratings in bulk fused silica," *Optics Letters*, vol. 31, no. 18, pp. 2690–2691, 2006.

[31] H. Zhang, S. M. Eaton, J. Li, A. H. Nejadmalayeri, and P. R. Herman, "Type ii high-strength bragg grating waveguides photowritten with ultrashort laser pulses," *Optics Express*, vol. 15, no. 7, pp. 4182–4191, 2007.

[32] G. Brown, R. R. Thomson, A. K. Kar, N. D. Psaila, and H. T. Bookey, "Ultrafast laser inscription of bragg-grating waveguides using the multiscan technique," *Optics Letters*, vol. 37, no. 4, pp. 491–493, 2012.

[33] R. Thomson, T. A. Birks, S. Leon-Saval, A. Kar, and J. Bland-Hawthorn, "Ultrafast laser inscription of an integrated photonic lantern," *Optics Express*, vol. 19, no. 6, pp. 5698–5705, 2011.

[34] M. Ams, G. Marshall, D. Spence, and M. Withford, "Slit beam shaping method for femtosecond laser direct-write fabrication of symmetric waveguides in bulk glasses," *Optics Express*, vol. 13, no. 15, pp. 5676–5681, 2005.

[35] Y. Nasu, M. Kohtoku, and Y. Hibino, "Low-loss waveguides written with a femtosecond laser for flexible interconnection in a planar light-wave circuit," *Optics Letters*, vol. 30, no. 7, pp. 723–725, 2005.

[36] A. Mermillod-Blondin, I. M. Burakov, Y. P. Meshcheryakov, N. M. Bulgakova, E. Audouard, A. Rosenfeld, A. Husakou, I. V. Hertel, and R. Stoian, "Flipping the sign of refractive index changes in ultrafast and temporally shaped laser-irradiated borosilicate crown optical glass at high repetition rates," *Physical Review B*, vol. 77, no. 10, p. 104205, 2008.

[37] S. Eaton, H. Zhang, P. Herman, F. Yoshino, L. Shah, J. Bovatsek, and A. Arai, "Heat accumulation effects in femtosecond laser-written waveguides with variable repetition rate," *Optics Express*, vol. 13, no. 12, pp. 4708–4716, 2005.

[38] S. M. Eaton, H. Zhang, M. L. Ng, J. Li, W.-J. Chen, S. Ho, and P. R. Herman, "Transition from thermal diffusion to heat accumulation in high repetition rate femtosecond laser writing of buried optical waveguides," *Optics Express*, vol. 16, no. 13, pp. 9443–9458, 2008.

[39] N. D. Psaila, R. R. Thomson, H. T. Bookey, S. Shen, N. Chiodo, R. Osellame, G. Cerullo, A. Jha, and A. K. Kar, "Supercontinuum generation in an ultrafast laser inscribed chalcogenide glass waveguide," *Optics Express*, vol. 15, no. 24, pp. 15776–15781, 2007.

[40] J. Burghoff, S. Nolte, and A. Tünnermann, "Origins of waveguiding in femtosecond laser-structured linbo3," *Applied Physics A*, vol. 89, no. 1, pp. 127–132, 2007.

[41] A. Okhrimchuk, A. Shestakov, I. Khrushchev, and J. Mitchell, "Depressed cladding, buried waveguide laser formed in a yag: Nd 3+ crystal by femtosecond laser writing," *Optics Letters*, vol. 30, no. 17, pp. 2248–2250, 2005.

[42] D. Choudhury, J. R. Macdonald, and A. K. Kar, "Ultrafast laser inscription: perspectives on future integrated applications," *Laser & Photonics Reviews*, vol. 8, no. 6, pp. 827–846, 2014.

[43] R. Thomson, S. Campbell, I. Blewett, A. Kar, and D. Reid, "Optical waveguide fabrication in z-cut lithium niobate (linbo3) using femtosecond pulses in the low repetition rate regime," *Applied Physics Letters*, vol. 88, no. 11, pp. 111109–111109, 2006.

[44] R. Osellame, G. Cerullo, and R. Ramponi, *Femtosecond Laser Micromachining: Photonic and Microfluidic Devices in Transparent Materials*, vol. 123. Springer Science & Business Media, 2012.

[45] P. Salter, M. Baum, I. Alexeev, M. Schmidt, and M. Booth, "Exploring the depth range for three-dimensional laser machining with aberration correction," *Optics Express*, vol. 22, no. 15, pp. 17644–17656, 2014.

[46] R. Osellame, S. Taccheo, M. Marangoni, R. Ramponi, P. Laporta, D. Polli, S. De Silvestri, and G. Cerullo, "Femtosecond writing of active optical waveguides with astigmatically shaped beams," *Journal of the Optical Society of America B*, vol. 20, no. 7, pp. 1559–1567, 2003.

[47] R. Thomson, A. Bockelt, E. Ramsay, S. Beecher, A. Greenaway, A. Kar, and D. Reid, "Shaping ultrafast laser inscribed optical waveguides using a deformable mirror," *Optics Express*, vol. 16, no. 17, pp. 12786–12793, 2008.

[48] A. Szameit, F. Dreisow, T. Pertsch, S. Nolte, and A. TŘnnermann, "Control of directional evanescent coupling in fs laser written waveguides," *Optics Express*, vol. 15, no. 4, pp. 1579–1587, 2007.

[49] I. Mansour and F. Caccavale, "An improved procedure to calculate the refractive index profile from the measured near-field intensity," *Journal of Lightwave Technology*, vol. 14, no. 3, pp. 423–428, 1996.

[50] D. Blömer, A. Szameit, F. Dreisow, T. Schreiber, S. Nolte, and A. Tünnermann, "Nonlinear refractive index of fs-laser-written waveguides in fused silica," *Optics Express*, vol. 14, no. 6, pp. 2151–2157, 2006.

[51] R. Martinez-Vazquez, R. Osellame, G. Cerullo, R. Ramponi, and O. Svelto, "Fabrication of photonic devices in nanostructured glasses by femtosecond laser pulses," *Optics Express*, vol. 15, no. 20, pp. 12628–12635, 2007.

[52] K. Hill, Y. Fujii, D. C. Johnson, and B. Kawasaki, "Photosensitivity in optical fiber waveguides: Application to reflection filter fabrication," *Applied Physics Letters*, vol. 32, no. 10, pp. 647–649, 1978.

[53] G. Meltz, W. Morey, and W. Glenn, "Formation of bragg gratings in optical fibers by a transverse holographic method," *Optics Letters*, vol. 14, no. 15, pp. 823–825, 1989.

[54] I. Bennion, J. Williams, L. Zhang, K. Sugden, and N. Doran, "Uv-written in-fibre bragg gratings," *Optical and Quantum Electronics*, vol. 28, no. 2, pp. 93–135, 1996.

[55] C. Q. Trinh, S. C. Ellis, J. Bland-Hawthorn, J. S. Lawrence, A. J. Horton, S. G. Leon-Saval, K. Shortridge, J. Bryant, S. Case, M. Colless, *et al.*, "Gnosis: the first instrument to use fiber bragg gratings for oh suppression," *The Astronomical Journal*, vol. 145, no. 2, p. 51, 2013.

[56] K. O. Hill and G. Meltz, "Fiber bragg grating technology fundamentals and overview," *Journal of Lightwave Technology*, vol. 15, no. 8, pp. 1263–1276, 1997.

[57] P. W. Anderson, "Absence of diffusion in certain random lattices," *Physical Review*, vol. 109, no. 5, p. 1492, 1958.

[58] T. Schwartz, G. Bartal, S. Fishman, and M. Segev, "Transport and anderson localization in disordered two-dimensional photonic lattices," *Nature*, vol. 446, no. 7131, pp. 52–55, 2007.

[59] S. Mukherjee, A. Spracklen, D. Choudhury, N. Goldman, P. Öhberg, E. Andersson, and R. R. Thomson, "Modulation-assisted tunneling in laser-fabricated photonic wannier–stark ladders," *New Journal of Physics*, vol. 17, no. 11, p. 115002, 2015.

[60] A. Szameit, J. Burghoff, T. Pertsch, S. Nolte, A. Tünnermann, and F. Lederer, "Two-dimensional soliton in cubic fs laser written waveguide arrays in fused silica," *Optics Express*, vol. 14, no. 13, pp. 6055–6062, 2006.

[61] H. Tasaki, "Hubbard model and the origin of ferromagnetism," *The European Physical Journal B*, vol. 64, no. 3-4, pp. 365–372, 2008.

[62] J. D. Bodyfelt, D. Leykam, C. Danieli, X. Yu, and S. Flach, "Flatbands under correlated perturbations," *Physical Review Letters*, vol. 113, no. 23, p. 236403, 2014.

[63] D. Guzmán-Silva, C. Mejía-Cortés, M. Bandres, M. Rechtsman, S. Weimann, S. Nolte, M. Segev, A. Szameit, and R. Vicencio, "Experimental observation of bulk and edge transport in photonic lieb lattices," *New Journal of Physics*, vol. 16, no. 6, p. 063061, 2014.

[64] S. Mukherjee, A. Spracklen, D. Choudhury, N. Goldman, P. Öhberg, E. Andersson, and R. R. Thomson, "Observation of a localized flat-band state in a photonic lieb lattice," *Physical Review Letters*, vol. 114, no. 24, p. 245504, 2015.

[65] R. A. Vicencio, C. Cantillano, L. Morales-Inostroza, B. Real, C. Mejía-Cortés, S. Weimann, A. Szameit, and M. I. Molina, "Observation of localized states in lieb photonic lattices," *Physical Review Letters*, vol. 114, p. 245503, Jun 2015.

[66] S. Xia, Y. Hu, D. Song, Y. Zong, L. Tang, and Z. Chen, "Demonstration of flat-band image transmission in optically induced lieb photonic lattices," *Optics Letters*, vol. 41, no. 7, pp. 1435–1438, 2016.

[67] R. A. Vicencio and C. Mejía-Cortés, "Diffraction-free image transmission in kagome photonic lattices," *Journal of Optics*, vol. 16, no. 1, p. 015706, 2014.

[68] Y. Zong, S. Xia, L. Tang, D. Song, Y. Hu, Y. Pei, J. Su, Y. Li, and Z. Chen, "Observation of localized flat-band states in kagome photonic lattices," *Optics Express*, vol. 24, no. 8, pp. 8877–8885, 2016.

[69] S. Mukherjee and R. R. Thomson, "Observation of localized flat-band modes in a quasi-one-dimensional photonic rhombic lattice," *Optics Letters*, vol. 40, no. 23, pp. 5443–5446, 2015.

[70] S. Weimann, L. Morales-Inostroza, B. Real, C. Cantillano, A. Szameit, and R. A. Vicencio, "Transport in sawtooth photonic lattices," *Optics Letters*, 2016.

[71] S. Longhi, "Aharonov–bohm photonic cages in waveguide and coupled resonator lattices by synthetic magnetic fields," *Optics Letters*, vol. 39, no. 20, pp. 5892–5895, 2014.

[72] A. V. Yulin and V. V. Konotop, "Conservative and pt-symmetric compactons in waveguide networks," *Optics Letters*, vol. 38, no. 22, pp. 4880–4883, 2013.

[73] J. Vidal, B. Douçot, R. Mosseri, and P. Butaud, "Interaction induced delocalization for two particles in a periodic potential," *Physical Review Letters*, vol. 85, no. 18, p. 3906, 2000.

[74] C. Dean, L. Wang, P. Maher, C. Forsythe, F. Ghahari, Y. Gao, J. Katoch, M. Ishigami, P. Moon, M. Koshino, *et al.*, "Hofstadter/'s butterfly and the fractal quantum hall effect in moire superlattices," *Nature*, vol. 497, no. 7451, pp. 598–602, 2013.

[75] K. Fang, Z. Yu, and S. Fan, "Realizing effective magnetic field for photons by controlling the phase of dynamic modulation," *Nature Photonics*, vol. 6, no. 11, pp. 782–787, 2012.

[76] M. C. Rechtsman, J. M. Zeuner, A. Tünnermann, S. Nolte, M. Segev, and A. Szameit, "Strain-induced pseudomagnetic field and photonic landau levels in dielectric structures," *Nature Photonics*, vol. 7, no. 2, pp. 153–158, 2013.

[77] S. Longhi, "Effective magnetic fields for photons in waveguide and coupled resonator lattices," *Optics Letters*, vol. 38, no. 18, pp. 3570–3573, 2013.

[78] C. Abilio, P. Butaud, T. Fournier, B. Pannetier, J. Vidal, S. Tedesco, and B. Dalzotto, "Magnetic field induced localization in a two-dimensional superconducting wire network," *Physical Review Letters*, vol. 83, no. 24, p. 5102, 1999.

[79] M. Niţă, B. Ostahie, and A. Aldea, "Spectral and transport properties of the two-dimensional lieb lattice," *Physical Review B*, vol. 87, no. 12, p. 125428, 2013.

[80] N. Goldman, D. Urban, and D. Bercioux, "Topological phases for fermionic cold atoms on the lieb lattice," *Physical Review A*, vol. 83, no. 6, p. 063601, 2011.

[81] J. C. Slater, "Electrons in perturbed periodic lattices," *Physical Review*, vol. 76, no. 11, p. 1592, 1949.

[82] G. H. Wannier, "Wave functions and effective hamiltonian for bloch electrons in an electric field," *Physical Review*, vol. 117, no. 2, p. 432, 1960.

[83] J. Zak, "Solid state physics," *edited by H. Ehrenreich, F. Seitz, and D. Turnbull (Academic, New York)*, vol. 27, 1972.

[84] S. Longhi, "Coherent destruction of tunneling in waveguide directional couplers," *Physical Review A*, vol. 71, no. 6, p. 065801, 2005.

[85] G. Della Valle, M. Ornigotti, E. Cianci, V. Foglietti, P. Laporta, and S. Longhi, "Visualization of coherent destruction of tunneling in an optical double well system," *Physical Review Letters*, vol. 98, no. 26, p. 263601, 2007.

[86] F. Bloch, "Über die quantenmechanik der elektronen in kristallgittern," *Zeitschrift für physik*, vol. 52, no. 7-8, pp. 555–600, 1928.

[87] T. Pertsch, P. Dannberg, W. Elflein, A. Bräuer, and F. Lederer, "Optical bloch oscillations in temperature tuned waveguide arrays," *Physical Review Letters*, vol. 83, no. 23, p. 4752, 1999.

[88] N. Chiodo, G. Della Valle, R. Osellame, S. Longhi, G. Cerullo, R. Ramponi, P. Laporta, and U. Morgner, "Imaging of bloch oscillations in erbium-doped curved waveguide arrays," *Optics Letters*, vol. 31, no. 11, pp. 1651–1653, 2006.

[89] D. Dunlap and V. Kenkre, "Dynamic localization of a charged particle moving under the influence of an electric field," *Physical Review B*, vol. 34, no. 6, p. 3625, 1986.

[90] A. Szameit, I. L. Garanovich, M. Heinrich, A. A. Sukhorukov, F. Dreisow, T. Pertsch, S. Nolte, A. Tünnermann, S. Longhi, and Y. S. Kivshar, "Observation of two-dimensional dynamic localization of light," *Physical Review Letters*, vol. 104, no. 22, p. 223903, 2010.

[91] F. Dreisow, A. Szameit, M. Heinrich, T. Pertsch, S. Nolte, A. Tünnermann, and S. Longhi, "Bloch-zener oscillations in binary superlattices," *Physical Review Letters*, vol. 102, no. 7, p. 076802, 2009.

[92] F. Dreisow, A. Szameit, M. Heinrich, S. Nolte, A. Tünnermann, M. Ornigotti, and S. Longhi, "Direct observation of landau-zener tunneling in a curved optical waveguide coupler," *Physical Review A*, vol. 79, no. 5, p. 055802, 2009.

[93] P. Tien and J. Gordon, "Multiphoton process observed in the interaction of microwave fields with the tunneling between superconductor films," *Physical Review*, vol. 129, no. 2, p. 647, 1963.

[94] P. Guimaraes, B. J. Keay, J. P. Kaminski, S. Allen Jr, P. Hopkins, A. Gossard, L. Florez, and J. Harbison, "Photon-mediated sequential resonant tunneling in intense terahertz electric fields," *Physical Review Letters*, vol. 70, no. 24, p. 3792, 1993.

[95] L. Kouwenhoven, S. Jauhar, J. Orenstein, P. McEuen, Y. Nagamune, J. Motohisa, and H. Sakaki, "Observation of photon-assisted tunneling through a quantum dot," *Physical Review Letters*, vol. 73, no. 25, p. 3443, 1994.

[96] C. Sias, H. Lignier, Y. Singh, A. Zenesini, D. Ciampini, O. Morsch, and E. Arimondo, "Observation of photon-assisted tunneling in optical lattices," *Physical Review Letters*, vol. 100, no. 4, p. 040404, 2008.

[97] A. Eckardt, T. Jinasundera, C. Weiss, and M. Holthaus, "Analog of photon-assisted tunneling in a bose-einstein condensate," *Physical Review Letters*, vol. 95, no. 20, p. 200401, 2005.

[98] J. Hubbard, "Electron correlations in narrow energy bands," in *Proceedings of the Royal Society of London A: Mathematical, Physical and Engineering Sciences*, vol. 276, pp. 238–257, The Royal Society, 1963.

[99] M. Greiner, O. Mandel, T. Esslinger, T. W. Hänsch, and I. Bloch, "Quantum phase transition from a superfluid to a mott insulator in a gas of ultracold atoms," *Nature*, vol. 415, no. 6867, pp. 39–44, 2002.

[100] I. Spielman, W. Phillips, and J. Porto, "Mott-insulator transition in a two-dimensional atomic bose gas," *Physical Review Letters*, vol. 98, no. 8, p. 080404, 2007.

[101] B. Paredes, A. Widera, V. Murg, O. Mandel, S. Fölling, I. Cirac, G. V. Shlyapnikov, T. W. Hänsch, and I. Bloch, "Tonks–girardeau gas of ultracold atoms in an optical lattice," *Nature*, vol. 429, no. 6989, pp. 277–281, 2004.

[102] T. Stöferle, H. Moritz, C. Schori, M. Köhl, and T. Esslinger, "Transition from a strongly interacting 1d superfluid to a mott insulator," *Physical Review Letters*, vol. 92, no. 13, p. 130403, 2004.

[103] S. Fölling, S. Trotzky, P. Cheinet, M. Feld, R. Saers, A. Widera, T. Müller, and I. Bloch, "Direct observation of second-order atom tunnelling," *Nature*, vol. 448, no. 7157, pp. 1029–1032, 2007.

[104] L. Fallani, J. Lye, V. Guarrera, C. Fort, and M. Inguscio, "Ultracold atoms in a disordered crystal of light: Towards a bose glass," *Physical Review Letters*, vol. 98, no. 13, p. 130404, 2007.

[105] K. Winkler, G. Thalhammer, F. Lang, R. Grimm, J. H. Denschlag, A. Daley, A. Kantian, H. Büchler, and P. Zoller, "Repulsively bound atom pairs in an optical lattice," *Nature*, vol. 441, no. 7095, pp. 853–856, 2006.

[106] N. Strohmaier, D. Greif, R. Jördens, L. Tarruell, H. Moritz, T. Esslinger, R. Sensarma, D. Pekker, E. Altman, and E. Demler, "Observation of elastic doublon decay in the fermi-hubbard model," *Physical Review Letters*, vol. 104, no. 8, p. 080401, 2010.

[107] D. Petrosyan, B. Schmidt, J. R. Anglin, and M. Fleischhauer, "Quantum liquid of repulsively bound pairs of particles in a lattice," *Physical Review A*, vol. 76, no. 3, p. 033606, 2007.

[108] M. Valiente and D. Petrosyan, "Two-particle states in the hubbard model," *Journal of Physics B: Atomic, Molecular and Optical Physics*, vol. 41, no. 16, p. 161002, 2008.

[109] C. E. Creffield and G. Platero, "Coherent control of interacting particles using dynamical and aharonov-bohm phases," *Physical Review Letters*, vol. 105, no. 8, p. 086804, 2010.

[110] S. Longhi and G. Della Valle, "Klein tunneling of two correlated bosons," *The European Physical Journal B*, vol. 86, no. 5, pp. 1–10, 2013.

[111] M. Bello, C. Creffield, and G. Platero, "Long-range doublon transfer in a dimer chain induced by topology and ac fields," *Scientific Reports*, vol. 6, p. 22562, 2016.

[112] P. M. Preiss, R. Ma, M. E. Tai, A. Lukin, M. Rispoli, P. Zupancic, Y. Lahini, R. Islam, and M. Greiner, "Strongly correlated quantum walks in optical lattices," *Science*, vol. 347, no. 6227, pp. 1229–1233, 2015.

[113] E. Burovski, G. Orso, and T. Jolicoeur, "Multiparticle composites in density-imbalanced quantum fluids," *Physical Review Letters*, vol. 103, no. 21, p. 215301, 2009.

[114] M. Valiente, D. Petrosyan, and A. Saenz, "Three-body bound states in a lattice," *Physical Review A*, vol. 81, no. 1, p. 011601, 2010.

[115] F. Serwane, G. Zürn, T. Lompe, T. Ottenstein, A. Wenz, and S. Jochim, "Deterministic preparation of a tunable few-fermion system," *Science*, vol. 332, no. 6027, pp. 336–338, 2011.

[116] G. Zürn, F. Serwane, T. Lompe, A. Wenz, M. G. Ries, J. E. Bohn, and S. Jochim, "Fermionization of two distinguishable fermions," *Physical Review Letters*, vol. 108, no. 7, p. 075303, 2012.

[117] A. Wenz, G. Zürn, S. Murmann, I. Brouzos, T. Lompe, and S. Jochim, "From few to many: observing the formation of a fermi sea one atom at a time," *Science*, vol. 342, no. 6157, pp. 457–460, 2013.

[118] S. Murmann, A. Bergschneider, V. M. Klinkhamer, G. Zürn, T. Lompe, and S. Jochim, "Two fermions in a double well: Exploring a fundamental building block of the hubbard model," *Physical Review Letters*, vol. 114, no. 8, p. 080402, 2015.

[119] S. Murmann, F. Deuretzbacher, G. Zürn, J. Bjerlin, S. M. Reimann, L. Santos, T. Lompe, and S. Jochim, "Antiferromagnetic heisenberg spin chain of a few cold atoms in a one-dimensional trap," *Physical Review Letters*, vol. 115, no. 21, p. 215301, 2015.

[120] S. Longhi, "Optical realization of the two-site bose–hubbard model in waveguide lattices," *Journal of Physics B: Atomic, Molecular and Optical Physics*, vol. 44, no. 5, p. 051001, 2011.

[121] D. O. Krimer and R. Khomeriki, "Realization of discrete quantum billiards in a two-dimensional optical lattice," *Physical Review A*, vol. 84, no. 4, p. 041807, 2011.

[122] S. Longhi, "Photonic bloch oscillations of correlated particles," *Optics Letters*, vol. 36, no. 16, pp. 3248–3250, 2011.

[123] S. Longhi and G. Della Valle, "Coherent destruction of tunneling of two interacting bosons in a tight-binding lattice," *Physical Review A*, vol. 86, no. 4, p. 042104, 2012.

[124] G. Corrielli, A. Crespi, G. Della Valle, S. Longhi, and R. Osellame, "Fractional bloch oscillations in photonic lattices," *Nature Communications*, vol. 4, p. 1555, 2013.

[125] A. Rai, C. Lee, C. Noh, and D. G. Angelakis, "Photonic lattice simulation of dissipation-induced correlations in bosonic systems," *Scientific Reports*, vol. 5, p. 8438, 2015.

[126] S. Mukherjee, M. Valiente, N. Goldman, A. Spracklen, E. Andersson, P. Öhberg, and R. R. Thomson, "Experimental simulation of two interacting particles in a one-dimensional lattice," *arXiv preprint arXiv:1604.00689*, 2016.

[127] K. Noba, "Dynamic localization of two electrons in a one-dimensional lattice system driven by an oscillating electric field," *Physical Review B*, vol. 67, p. 153102, Apr 2003.

[128] S. Longhi and G. Della Valle, "Tunneling control of strongly correlated particles on a lattice: a photonic realization," *Optics Letters*, vol. 36, no. 24, pp. 4743–4745, 2011.

[129] A. Szameit, I. L. Garanovich, M. Heinrich, A. A. Sukhorukov, F. Dreisow, T. Pertsch, S. Nolte, A. Tünnermann, and Y. S. Kivshar, "Polychromatic dynamic localization in curved photonic lattices," *Nature Physics*, vol. 5, no. 4, pp. 271–275, 2009.

[130] M. C. Rechtsman, J. M. Zeuner, Y. Plotnik, Y. Lumer, D. Podolsky, F. Dreisow, S. Nolte, M. Segev, and A. Szameit, "Photonic floquet topological insulators," *Nature*, vol. 496, no. 7444, pp. 196–200, 2013.

[131] C. Creffield and G. Platero, "Localization of two interacting electrons in quantum dot arrays driven by an ac field," *Physical Review B*, vol. 69, p. 165312, 2004.

[132] M. Holthaus and D. Hone, "Quantum wells and superlattices in strong time-dependent fields," *Physical Review B*, vol. 47, no. 11, p. 6499, 1993.

[133] D. O. Krimer, R. Khomeriki, and S. Flach, "Two interacting particles in a random potential," *JETP Letters*, vol. 94, no. 5, pp. 406–412, 2011.

[134] C. Albrecht and S. Wimberger, "Induced delocalization by correlation and interaction in the one-dimensional anderson model," *Physical Review B*, vol. 85, no. 4, p. 045107, 2012.

[135] M. Di Liberto, A. Recati, I. Carusotto, and C. Menotti, "Two-body physics in the su-schrieffer-heeger model," *arXiv preprint arXiv:1608.07341*, 2016.

[136] K. v. Klitzing, G. Dorda, and M. Pepper, "New method for high-accuracy determination of the fine-structure constant based on quantized hall resistance," *Physical Review Letters*, vol. 45, no. 6, p. 494, 1980.

[137] B. A. Bernevig, T. L. Hughes, and S.-C. Zhang, "Quantum spin hall effect and topological phase transition in hgte quantum wells," *Science*, vol. 314, no. 5806, pp. 1757–1761, 2006.

[138] L. Fu, C. L. Kane, and E. J. Mele, "Topological insulators in three dimensions," *Physical Review Letters*, vol. 98, no. 10, p. 106803, 2007.

[139] D. Hsieh, D. Qian, L. Wray, Y. Xia, Y. S. Hor, R. Cava, and M. Z. Hasan, "A topological dirac insulator in a quantum spin hall phase," *Nature*, vol. 452, no. 7190, pp. 970–974, 2008.

[140] M. Aidelsburger, M. Lohse, C. Schweizer, M. Atala, J. T. Barreiro, S. Nascimbene, N. Cooper, I. Bloch, and N. Goldman, "Measuring the chern number of hofstadter bands with ultracold bosonic atoms," *Nature Physics*, vol. 11, no. 2, pp. 162–166, 2015.

[141] M. Hafezi, E. A. Demler, M. D. Lukin, and J. M. Taylor, "Robust optical delay lines with topological protection," *Nature Physics*, vol. 7, no. 11, pp. 907–912, 2011.

[142] M. Hafezi, S. Mittal, J. Fan, A. Migdall, and J. Taylor, "Imaging topological edge states in silicon photonics," *Nature Photonics*, vol. 7, no. 12, pp. 1001–1005, 2013.

[143] S. Mittal, J. Fan, S. Faez, A. Migdall, J. Taylor, and M. Hafezi, "Topologically robust transport of photons in a synthetic gauge field," *Physical Review Letters*, vol. 113, no. 8, p. 087403, 2014.

[144] M. S. Rudner, N. H. Lindner, E. Berg, and M. Levin, "Anomalous edge states and the bulk-edge correspondence for periodically driven two-dimensional systems," *Physical Review X*, vol. 3, no. 3, p. 031005, 2013.

[145] A. Gómez-León and G. Platero, "Floquet-bloch theory and topology in periodically driven lattices," *Physical Review Letters*, vol. 110, p. 200403, 2013.

[146] N. Goldman and J. Dalibard, "Periodically driven quantum systems: Effective hamiltonians and engineered gauge fields," *Physical Review X*, vol. 4, p. 031027, 2014.

[147] T. Kitagawa, E. Berg, M. Rudner, and E. Demler, "Topological characterization of periodically driven quantum systems," *Physical Review B*, vol. 82, no. 23, p. 235114, 2010.

[148] W. Huang and H. A. Haus, "Self-consistent vector coupled-mode theory for tapered optical waveguides," *Journal of Lightwave Technology*, vol. 8, no. 6, pp. 922–926, 1990.

[149] L. J. Maczewsky, J. M. Zeuner, S. Nolte, and A. Szameit, "Observation of photonic anomalous floquet topological insulators," *arXiv preprint arXiv:1605.03877*, 2016.

[150] S. Mukherjee, A. Spracklen, M. Valiente, E. Andersson, P. Öhberg, N. Goldman, and R. R. Thomson, "Experimental observation of anomalous topological edge modes in a slowly-driven photonic lattice," *arXiv preprint arXiv:1604.05612*, 2016.

[151] R. Khomeriki and S. Flach, "Landau-zener bloch oscillations with perturbed flat bands," *Physical Review Letters*, vol. 116, no. 24, p. 245301, 2016.

[152] D. Leykam, S. Flach, O. Bahat-Treidel, and A. S. Desyatnikov, "Flat band states: Disorder and nonlinearity," *Physical Review B*, vol. 88, no. 22, p. 224203, 2013.

[153] P. Titum, E. Berg, M. S. Rudner, G. Refael, and N. H. Lindner, "Anomalous floquet-anderson insulator as a nonadiabatic quantized charge pump," *Physical Review X*, vol. 6, no. 2, p. 021013, 2016.